Title
Microfluidic and Holographic Microscopy Integrated Optoelectronic Tweezers For Single-cell Applications

Author
Huang, Kuo-Wei

Publication Date
2012

Peer reviewed|Thesis/dissertation

UNIVERSITY OF CALIFORNIA

Los Angeles

Microfluidic and Holographic Microscopy Integrated Optoelectronic Tweezers For Single-cell Applications

A dissertation submitted in partial satisfaction of the

requirements for the degree Doctor of Philosophy

in Mechanical Engineering

by

Kuo-Wei Huang

2013

ABSTRACT OF THE DISSERTATION

Microfluidic and Holographic Microscopy Integrated Optoelectronic Tweezers

For Single-cell Applications

By

Kuo-Wei Huang

Doctor of Philosophy in Mechanical Engineering

University of California, Los Angeles, 2013

Professor Pei-Yu Chiou, Chair

Optoelectronic tweezers (OET), combining the advantages of optical and dielectrophoretic (DEP) manipulation, has been widely used in laboratories around the world. Despite being a useful platform for single-cell manipulation, OET still suffers from two limitations, the difficulty of being integrated with microfluidic components and the lack of large-area real-time detection function. The two issues restrain OET from complicated single-cell analysis and large-area automated manipulation. To integrate the PDMS-based microfluidic components with OET, two techniques are purposed in this research, SWNT-embedded electrodes and 3D PDMS membranes. The first technique uses SWNT thin films as transparent and conductive electrodes for OET inside multilayer PDMS channels. 3D microfluidic technique makes PDMS membranes to be a multilayer network between two rigid OET substrates. Based on these two new fabrication methods, novel microfluidic OET platforms have been developed to enable single or

multiple cell manipulation and to accomplish multi-steps tasks. Therefore, off-chip and on-chip single-cell RT-qPCR are achieved on these two platforms respectively.

To address the issue of large-area real-time detection, a new technology, holographic on-chip imaging microscopy, is employed. This integrated platform has optical detection area equal to the size of an optoelectronic sensor array. Recording holographic images or digital reconstruction images, the automated image analysis in the system can keep the real-time positions of thousands of objects in field of view. Based on the real-time position information, the system simultaneously transports the target objects to the desired destinations. Particles or cells can be patterned or sorted on the platform which enabling simultaneous automated imaging, image analysis, real-time position feedback and interactive manipulation of thousands of micro-objects over an area of 240 mm^2.

The dissertation of Kuo-Wei Huang is approved.

Chih-Ming Mo

Chang-Jin Kim

Dino Di Carlo

Pei-Yu Chiou, Committee Chair

University of California, Los Angeles

2013

To My Family and My Friends

Table of Contents

Acknowledgements

Above all, I thank my advisor, Dr. Pei-Yu Chiou, for his guidance and support throughout my Ph.D. study and graduate career. His creativity and insight not only give an energetic atmosphere in the lab but also open a door in my research. To me, he is always the most inspiring and supportive one when I face a trouble in my researches. I am really grateful for having him and his advises during my Ph.D. life. I would like to thank my doctoral committee members, Dr. Chih-Ming Ho, and Dr. Chang-Jin Kim for their generous support and allowing me to use their equipments. Without them, the research would not have progressed as it did. I would also like to thank Dr. Bruce S. Dunn and Dr. Dino Di Carlo for being my committee in my qualify exam and dissertation. The comments from all of them are very valuable.

I am privileged to corporate with various people both inside and outside UCLA. I thank Dr. Aydogan Ozcan and Dr. Ting-Wei Su for their generous help and suggestions in lensfree holographic microscopy; Dr. Jiang Zhong for his discussion on single-cell analysis; Dr. Hsian-Rong Tseng and his group members, Yi-Chun Chen and Dr. Libo Zhao, for the help with PDMS fabrication and facilities; Dr. Ji-Ann Lee and Dr. Michael Teitell for helping with PCR. Particularly, I would like to extend the appreciation to Mr. Szu-Yuan Pu for his useful discussion and his friendship. I sincerely thank the people listed above for their kind support.

I have been very fortunate to work with many brilliant people in Dr. Chiou's group. I thank Dr. Ting-Hsiang Wu, Dr. Carina Kamaga, and Dr. Daisuke Yamane for their simulating discussions; Yi-Chien for his help with cell preparation; Yu-Chun for his innovation in developing 3D microfluidic devices. I am also grateful to the remaining members in the group, Sunny, Fan, Ray, Sabbir, Yajia, Wen, and Wendy. My collaboration with you has greatly

enriched my dissertation and I also want to thank you for your warm friendship during my study at UCLA.

I am eternally grateful to my parents and my family for their love and unwavering supports. The encouragements, including those from my parents, my grandparents, my uncles/aunts, and my brother, were my strongest support to overcome this challenge. I would also like to thank Shu-Chuan for her understanding and patience when I was busy with my research work. I also have to thank all my dear friends who I had known you since high school, college, or graduate study. Only with your company, I can finish this work. I thank all of you.

Vita

1997-2001	Bachelor of Science in Civil Engineering
	National Taiwan University, Taiwan
2001-2003	Master of Environmental Planning and Management
	National Taiwan University, Taiwan
2003-2005	Second Lieutenant
	Army (Engineer Company, 176 Brigade), Taiwan
2006-2008	Master of Science in Mechanical Engineering
	University of California, Los Angeles, U.S.

Chapter 1 Introduction

1.1 Optoelectronic Tweezers

Optoelectronic tweezers (OET) are a new optical manipulation concept that uses dielectrophoresis (DEP) or ac electroosmosis induced by projected optical images to grab tiny particles or move fluids with sizes ranging from tens of nanometers to hundreds of micrometres. The Principles of OET are based on the electrokinetic motions of particles or fluids under an electric field induced or perturbed by projected light. The first prototype of OET based on the optical control of surface conductivity was proposed by Chiou *et al.* in 2005 [1]. The first prototype of OET platforms is shown in Figure 1- 1 . An OET platform is composed of a photoconductive layer, a sample solution, a spatial light modulator, and a light source projected into the device. In conventional OET devices, optical components such as objective lenses are also needed for observation and projection. OET devices require unique configuration which includes a photoconductive surface on indium tin oxid (ITO) and ITO top electrode (Figure 1- 1). Between these two substrates, liquid containing particles is sandwiched. The most common mechanism of OET is DEP forces. At ~100 Hz, when the light patterned by the digital projector is projected onto the device, virtual electrodes are created in the area that light projected, and further disturbing the electric field between the two plates. Finally, dielectrophoretic traps are formed to spatially manipulate objects of interest. OET provide on-demand parallel DEP traps. The DEP traps can be re-shaped by changing projected light, so dynamic trap and manipulation have been achieved. This is the unique manipulation strategy OET offers. Based on the unique manipulation strategy, OET has been used to manipulate various objects such as polymer particles, cells, biomolecules, and nanotube wires.

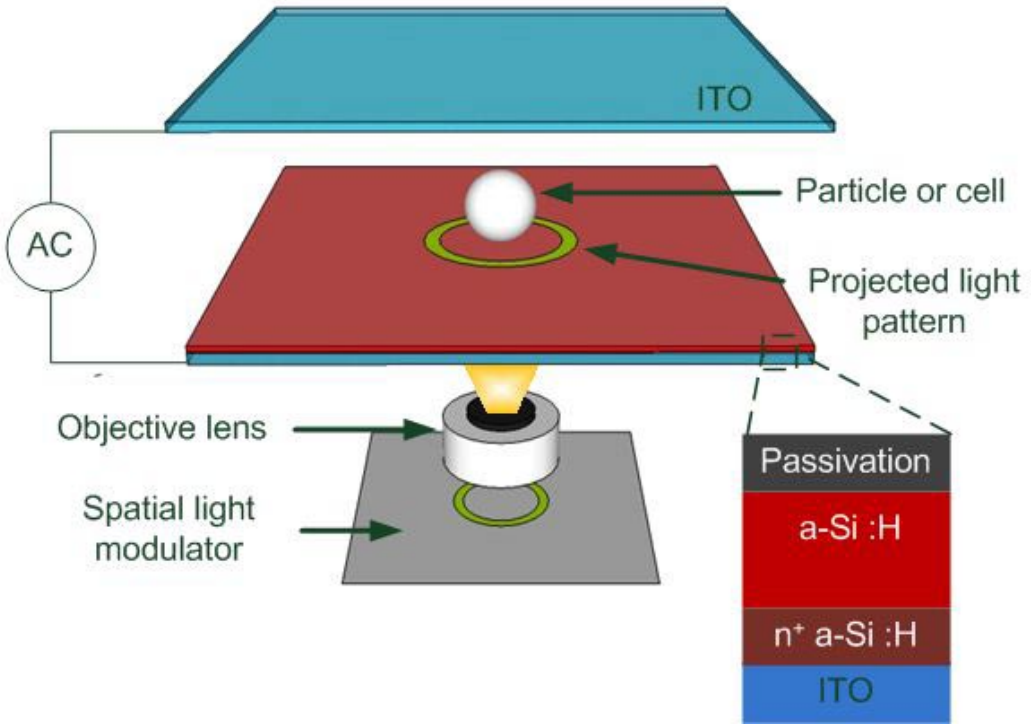

Figure 1- 1 The prototype of optoelectronic tweezers (OET). A conventional OET device composed of a photoconductive layer on ITO substrate and a top ITO electrode. Liquid containing particles is sandwiched between a transparent electrode and a photoconductive (amorphous silicon, a-Si:H) electrode. Experimental setup includes a digital projector and an objective lens. The light patterned by the digital projector is projected onto the device to generate virtual electrodes that in turn create dielectrophoretic traps in the illuminated areas.

For manipulate non-biological materials, one attractive application is to trap, separate, and arrange objects in nanometer scale, including silver or silicon nanowires, single-wall and multi-wall carbon nanotubes, metallic spherical nanocrystals, etc. Jamshidi *et al.* reported the manipulation of silver or silicon nanowires by OET platform [2]. Results show nanowires have very interesting OET trapping characteristics, the strong alignment with the electric field in the

medium. This characteristic is due to the large electrical polarizalbility along the nanowires' length. By adjusting the scanning speed of the projected light, silver and silicon nanowires were spatially separated. Silver nanowires were further assembled into an array. This shows the ability of "top-down" manipulation in nanometer scale. The trapping has been extended to individual and bundled carbon nanotubes (CNT) [3, 4]. CNTs benefit from their nearly one-dimensional structures in the manipulation. DEP forces generated by fix electrodes were reported to separate single-wall and multi-wall or metallic and semiconducting CNTs. Compared to prefabricated and fixed electrodes, OET manipulation combines the massive parallelism of DEP with the optical flexibility. From application point of view, dynamically manipulation of CNTs can be potentially integrated for energy and hydrogen storage devices, field emission and lighting devices. It makes OET manipulation of CNTs significantly interesting.

Biological samples such as cells, DNA, etc. are one of the most attractive objects for OET manipulation. Based on the DEP property, OET can be used to sort live or dead cells, and used to sort different types of cell. Chiou *et al.* demonstrated the selective concentration of live human B cells from a mixed population of live and dead B cells [1]. Ohta *et al*. spatially separated a mixed population of Jurkat and HeLa cells [5]. Besides separation of different type of cell, OET platform has been used to judge the cell properties. Viable live non-motile sperm was distinguished from non-viable sperm by OET [6]. This nun-invasive OET evaluation of sperm could be a potential method by which to identify viable non-motile sperm for assisted reproductive technologies. OET has been report to be a nun-contact tool for selection normal oocytes for in vitro fertilization [7]. Besides sperms and oocytes, motile bacteria have been also been trapped using OET [8]. The manipulation of DNA molecules using light-induced DEP in an OET device has also been demonstrated. Hoeb *et al.* deposited amorphous hydrogenated silicon

on a 70-nm thick untextured ZnO layer to build OET chips. In the experiments, double-stranded 48.5 kbp DNA of the λ-phage was marked with the intercalating fluorescent dye was trapped by DEP [9]. Positive DEP motions were observed and compared with thermal effect and Brownian motion. In nanoscale manipulation, Brownian motions on the nanoparticles are competing with the trapping forces. Trapping a nanoparticle is challenging and more difficult than microparticles because the DEP forces involved are proportional to the nanoparticle's volume. To overcome this issue, Lin *et al.* use microbeads bounded with DNA molecules to control the DNA [10]. They measured the elongation and rotation forces of DNA molecules using the indirect manipulations. Biological applications used OET have been reported. For example, assessment for embryos fertilization by OET provides a non-invasive method to measure embryo developmental stage [11].

1.2 Dielectrophoresis

Microfluidic and Lab-on-a-chip (LOC) devices are platforms that can handle complex chemical and biological processes and analysis for many applications. The applications include life sciences, basic biologies, pharmaceutical research, etc. The manipulation of particles in LOC systems is one of the crucial steps. The manipulation on chip is to realize following functions: trapping, sorting, separation and patterning, purification of cells, viruses, nanoparticles, microparticles and proteins. Various techniques have been reported to manipulate micro-paritcles in microfluidic systems such as optical tweezers, magnetic forces, acoustic forces and electrical forces. Among these mechanisms, the importance of electrical forces rises because the relatively easy control in microsystems and the label-free properties.

Electrical forces mainly results from the interaction between charged particles and the fields. Basically, two types of electrical forces can be commonly cataloged, electrical electrophoresis (EP) and dielectrophoresis (DEP). EP is based on $\mathbf{F} = q\mathbf{E}$ where q is the net charge of the particles and $\mathbf{E}$ is the electric field. EP is usually used in capillary separation of DNA, proteins, etc. While the EP is from the charge of particle and electric field, DEP is the movement coming from the interactions of particles' electric dipole and spatial gradient of the surrounding electric field. Because most materials do not have permanent dipole which comes from the orientation of atoms, the DEP forces mainly results from the induced dipoles which is due to the applied external electric field. Figure 1- 2 shows the concept of DEP forces. The induced dipole is due to polarizability of the particles, which can be described as the ability of a material to produce charge at the interface when particles in an external electric field. When a particle is suspended in an electrolyte and placed in an electric field, the charges inside the particle and inside the medium will accumulate in the interface. The redistribution of the charges at the particle–medium interface will depend on the polarizabilities of the particle and the medium. When the polarizability of the particle is higher than the polarizability of the medium, more charges will accumulate at the particle's side. On the contrary, if the polarizability of the medium is higher than the particles', more charges will accumulate at the medium's side. The difference in the charge density on either side of the particle leads to an induced dipole across the particle aligned with the applied electric field. If we put the system is placed in a non-uniform electric field distribution, the particle feels different forces at each end. The unbalance of forces at both ends generates a net force in either direction depending on the polarizability of the particle and the medium.

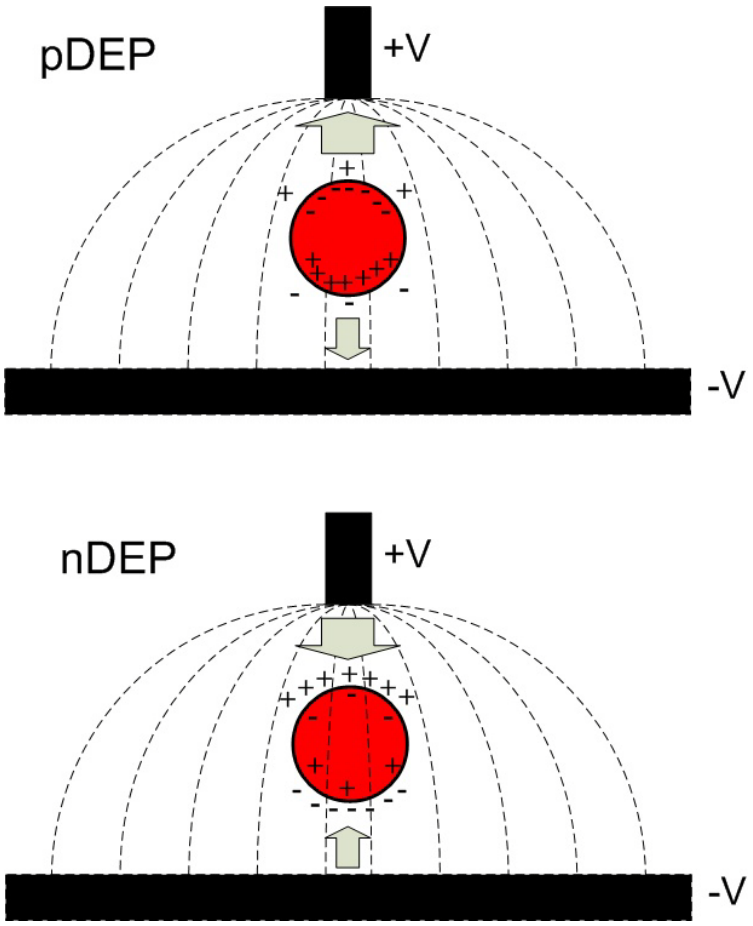

Figure 1- 2 DEP force on an induced dipole. The neutral particles in a non-uniform electric field will experience a net force toward the electric field maximum or minimum. (A) (B)

The general expression of DEP can be written

$$F_{dep} = p \cdot \nabla E \qquad \textbf{Eq. 1- 1}$$

where p is the particle's dipole, **E** is the external electric field. If the gradient of the electric field in Eq. 1- 1 is zero, there will be no DEP forces. Another approach to express DEP force is to use Maxwell stress tensor (MST) formulation, which is integrating the stress tensor T over the surface of the particle:

$$\vec{F}_{DEP}(t) = \oint (T \cdot \vec{n}) dA \qquad \textbf{Eq. 1- 2}$$

where $\vec{n}$ is the unit normal to A and t is time. This is the most general approach to the force [12]. For an applied electric field with a frequency less than 100 MHz, the expression for the time-average DEP force for spherical cells immersed in a medium with complex permittivity ε_s^* and subjected to electric field can be described as follows:

$$\langle F(DEP)\rangle = \frac{1}{4}\mathrm{Re}(\varepsilon_s^*)\oint_A \left[\left(EE^* + E^*E\right) - |E|^2\right]\cdot \vec{n}\,dA \quad , \qquad \textbf{Eq. 1- 3}$$

where E is the electric field distributed on surface A enclosing the cell, and E* is the complex conjugate of E[12]. The MST is the most precise approach to the derivation of field induced forces. The DEP force of a spherical particle can be derived by MST. During the derivation of DEP force, a critical assumption is that the field in the particle surface is expanded in terms of the original field at the particle center. When the particle radius is very small compared with the spatial features of the electrode system (i.e. the size of the particle is much smaller than the distance over which the external electric field varies), the first-order approximation is reasonable. The following expression for DP force for a spherical cell subject to a sinusoidal electric field can be derived by first-order approximation:

$$\langle F(DEP)\rangle = 2\pi r^3 \varepsilon_m \,\mathrm{Re}(f_{CM})\nabla E^2 \qquad \textbf{Eq. 1- 4}$$

where r is the radius of a particle, ε_m is the permittivity of the medium, E is the local electric field, and $\mathrm{Re}(f_{CM})$ is the real part of the Clausius-Mossotti (CM) factor, which is defined by

$$f_{CM}(\omega) = \frac{\varepsilon_p^* - \varepsilon_m^*}{\varepsilon_p^* + 2\varepsilon_m^*}, \quad \varepsilon_p^* = \varepsilon_p - j\frac{\sigma_p}{\omega}, \quad \varepsilon_m^* = \varepsilon_m - j\frac{\sigma_m}{\omega} \qquad \textbf{Eq. 1- 5}$$

where ε_p^* and ε_n^* are the complex permittivity of the particle and medium respectively, j is $\sqrt{-1}$, σ is the conductivity of the particle or medium, and ω is the angular frequency of the applied electric field. The local electric field, E, contains the information about the non-uniformity of the field created by the virtual electrodes on the photoconductive layer. The real part of CM factor, which varies with the applied ac frequency and the properties of the particle and the medium, can be either positive or negative. When the real part of CM factor is positive, cell will experience a positive DEP (pDEP) and be attracted to the strong electric field region. On the contrary, the negative DEP, repelling cell from electric field maxima, is induced by negative CM factor. Eq. 1-4 has a limitation when applied to cells, as their size is comparable to the electrodes. For more accurate calculation of DEP forces, higher order dipole moments need be introduced in to the approach or numerical methods should be used to determine the electric field distribution for the MST method[13].

1.3 Different Dominant Effects of OET

Although the light-induced DEP is most common used mechanism in OET, several other electrokinetic and hydrodynamic effects are also present in OETs[14]. Light-induced fluidic flow resulting from AC electro-osmosis and electrothermal (ET) effects may also occur on the conventional OET platforms. The optically induced ac electroosmosis is a fluidic motion generated by the motion of ions within the electric double layer due to the tangential electric field. OET have used this mechanism for concentration of microparticles, nanoparticles and molecules. Light-induced ac electroosmosis (LACE) only occurs when the voltage bias frequency low (<10 kHz) or the optical intensity high (>1000 W cm^{-2}) [14]. In most of cases, OET is operated at high frequency (>100 kHz) and in low optical intensity (1 W cm^{-2}), so DEP

forces dominate. LACE flow can be modeled by calculating the slip velocity due to the interaction of the lateral component of the electric field with the electrical double layer on a-Si:H surface,

$$v_{slip} = -(\varepsilon_m \zeta E_t)/(\eta) \qquad \textbf{Eq. 1- 6}$$

where ζ is the zeta potential of the electrical double layer and E_t is the lateral component of the electric field. ET flow is generated by the absorption of the light in the a-Si:H creating a local heat gradient. The heat gradient creates a gradient in permittivity and conductivity of the liquid layer, generating dielectrophoretic forces on the liquid layer. This force drives the liquid in a vortex flow pattern around the illuminated area. The ET can be described by:

$$\langle f_{ET} \rangle = \frac{1}{2}\mathrm{Re}\left[\frac{\sigma_m \varepsilon_m}{\sigma_m + i\omega\varepsilon_m}(\kappa_\varepsilon - \kappa_\sigma)(\nabla T \cdot E)E^* - \frac{1}{2}\varepsilon_m \kappa_\varepsilon |E|^2 \nabla T \right] \qquad \textbf{Eq. 1- 7}$$

where σ_m is the fluid conductivity; $\kappa_\varepsilon = (1/\varepsilon)(\partial\varepsilon/\partial T)$ and $\kappa_\sigma = (1/\sigma)(\partial\sigma/\partial T)$ are the variations of the electrical properties according to the temperature; T is the temperature; and E^* is the complex conjugate of the electric field. In an optoelectrofluidic device, thermal gradients can be generated by Joule heating or by highly focused light. Figure 1- 3 is the sckematic of LACE mechanism on OET. LACE mechanism has been used to trap and concentrate nanoscale particles [15, 16]. 90-nm diameter spherical gold nanoparticles were collected by LACE and ET over a long range of distance. DEP force in short range can help to immobilize the nanoparticles. Results show that the particles can stay in the surface even after the top ITO is removed and the remainder of the liquid is blow-dried. Another application of LACE is separating particles. Hwang et. al. employ the LACE and DEP together to separate different sizes of particles [17]. The results show that large-diameter polystyrene beads were repelled from the area while large-diameter polystyrene

beads were attracted. The reason is due to relatively strong negative DEP forces on large beads and stronger LACE on small beads.

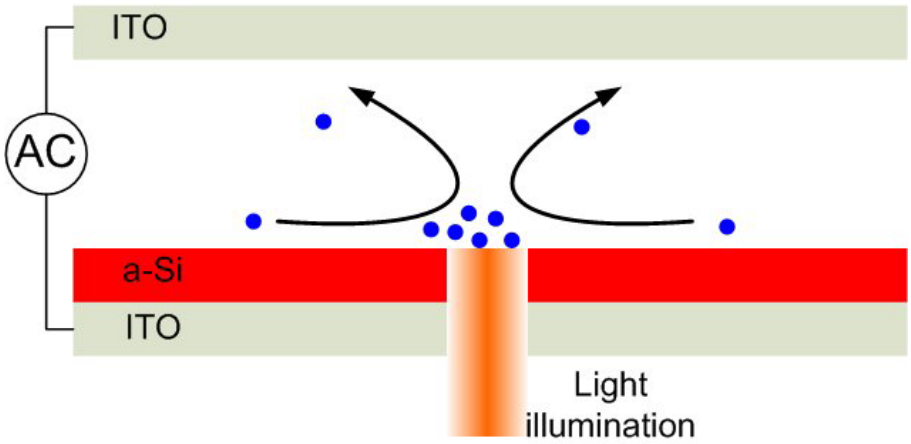

Figure 1- 3 LACE mechanism on OET platform.

Several structure variations have been reported. One extension known as floating-electrode OET (FEOET) was purposed by Park *et al.* recently [18, 19]. FEOET device used a lateral electric field formed by two separated electrodes on a photoconductive layer to move water droplet in oil. The lateral electric field makes the device an open channel configuration which allows integration with other microfluidic components such as tubing, microwell arrays and closed channels. DEP and lateral field optoelectrowetting can be implemented on the platform and the light intensity to trigger FEOET is as low as 400 $\mu W/cm^2$. Droplet functions include merging, mixing and splitting have been accomplished. Besides FEOET for droplet manipulation, lateral-field optoelectronic tweezers (LOET) was reported to control cells in single-sided OET device [20]. However, the further integration with other microfluidic components has not been reported yet.

Changing the photoconductive material gives a simple way to fabricate OET chips. TiOPc, an organic photoconductive material, has been used to form the photoconductive layer for OET [21]. The fabrication process of the TiOPc-based chip substrate can be finished by spin-coating on an ITO glass.

Rather than modifying the device structure, OET has been changed the method light beams project on. Light patterns are typically generated by a digital micro-mirror device (DMD) in conventional OET. Choi *et al.* proposed a liquid crystal display (LCD)-based OET platform [22]. In LCD-based OET platform, the objective lens between the DMD mirror and OET device is taken off. This lens-free structure enlarged the manipulation area to centimeter scale and reducing the effort of optical alignment, but lens-free configuration also blurred the projected image and reduced the gradient of the light pattern. A modified LCD-based OET were proposed to solve the problem [23]. A condenser lens was placed between the OET and LCD to focus a light pattern onto the photoconductive layer. Although the large-area manipulation has been shown, the large-area detection function is still missing.

1.4 Challenges of OET

One of the biggest challenges to conventional OET is the requirement of low-conductivity media (<0.1 S m^{-1}), so cells manipulation in conventional OETs usually need to replace physiological buffers with an isotonic solution. Once put in the isotonic solution, cells begin to lose normal functions such as proliferation and growth after a few hours. Therefore, for long-term cell manipulation and culture, Hsu *et al*. has reported a phototransistor-based OET. Phototransistor-based OET uses silicon substrates to form phototransistors generating 500 times higher photoconductivity than the amorphous silicon photoconductor [24].

The integration of microfluidic channels into an OET is also very challenging. OET manipulation based on DEP is also limited due to its own configuration. Conventional OET consists of ITO top electrodes, liquid media, and a photoconductive layer. The simple structure of OET basically doesn't need any fluidic components such as channels, chambers, valves or pumps. However, the simple structure restrains OET from performing complicated processes such as injection or collection of samples, change of buffer media, and continuous sample processing, because the two rigid substrates are very difficult to be realized in the most popular microfluidic material, PDMS, which is nun-conductive and mechanically flexible. One of the biggest challenges of standard OET is in its difficulty in integration with other microfluidic components for real biological applications such as single-cell analysis. Without the integration of other microfluidic functions, OET was limited to being a micro-manipulation tool, which loses many real benefits and practical applications. The laterial-filed OET (LOET) using single substarte may be a solution. However, LOET has the limitation of moving particles in the direction perpendicular to the electrodes when the particles are relatively smaller than its electrodes. To address this limitation, the integration with PDMS-based microfluidic structures is discussed in Chapter 2. The main challenge of the integration is to build a transparent and conductive electrode in non-conductive polymer. Chapter 2 shows two methods to build electrode for OET, the fabrication details and structure of the devices. New fabrication methods are developed for integration of OET and traditional PDMS soft lithography techniques, particles and cells can be manipulated in PDMS channels by light-induced DEP.

In Chapter 3, a brand new platform is developed by transforming OET into one of the function in new platform. Instead of build block PDMS structure on OET chips, PDMS thin membranes are sandwiched between ITO glasses and OET chips. Some integration between

OET and microfluidic channels have also been reported [25, 26], but two major problems are still unsolved. First, leakage is the issue when photoresists are the spacer to form the micro-channels. The photoresists cannot be strongly bonded to ITO or OET chips, and the gaps between spacers and chips restrict the high speed or high pressure pumping. It will make pressurized flow and pressurized valves impossible. Despite the fact that some researches using PDMS as the side wall of channels, the lack of micro-valve restricts the device to simple applications. Therefore, the second issue is the integration of the micro-valves with OET. In the cases of PDMS as the side wall of channels, OET platforms were not really merged with soft lithography if the device cannot control the liquid well, which limits OET from more complex microfluidic functions such as reagent mix, cell lysis, single-cell mRNA analysis or on-chip RT-PCR[27]. Thus, Chapter 3 describes a new fabrication method to stack PDMS membranes with micro-valves between two rigid substrates. The fabrication method creates brand new OET devices by using 3-dimensional (3D) PDMS techniques (i.e. PDMS membrane with via holes). We improved the 3D PDMS technique by increasing the "via patterns" from holes to channels and improved the flatness of the PDMA membranes. The two major improvements make it possible that the PDMS membrane can be sandwiched in two rigid substrates and the OET function can be realized in those via channels.

Chapter 4 discusses arming OET with a complementary function, large-area detection. It has also been demonstrated that the optical manipulation area of OET can be extended to $26.4 \times 19.6\ mm^2$ using light patterns shaped by a transmission type LCD display without using a projection lens. Although large-scale OET manipulation has been achieved, most of these manipulations are passive type, meaning that the optical image patterns are pre-programmed and projected on OET without knowing where the particles or cells are. To achieve an active and

real-time interactive optical manipulation, an image feedback system is necessary to identify particle locations before projecting corresponding optical patterns. To identify particles with a size of few to 10 μm needs an objective lens whose field of view (FOV) is very limited. The FOV of a 10 × objective lens is less than 600 μm. The tradeoff between FOV and optical resolution also prevents the use of objective lenses with lower magnifications. As a result, real-time, interactive optical manipulation over large area is prohibited due to the limitation of the image detection method used in OET.

The configuration of conventional OET makes it difficult to work with other microfluidic components such as valves, pumps, mixers. Although it is very attractive that conventional OET allows individual particle manipulation under a relatively large chamber (several cm * several cm), most of the single-cell studies need not only individual cell control but also isolating them into discrete environments for performing complex protocols. It requires the control of liquid in the chamber. Chapter 5 is proposing to new microfluidic design for OET integration. The new structures are based on the SWNT electrode described in Chapter 2 and 3-dimension (3D) PDMS fabrication technique in Chapter 3. In this chapter, we present the two platforms incorporating OET into PDMS-based microfluidic channels enabling single or multiple cell control to accomplish multi-steps tasks for single-call analysis. On this platform, OET and PDMS microfluidic components provide complementary functions. Being free from the fixed layout of micro-electrode, OET provides spatial trapping and sorting cells of interest in microfluidic channels. PMDS microfluidic components are effective in controlling fluid. The integrated platform allows users to selectively retrieve individual cells from a population based on their optical signatures such as size, shape, and fluorescence colors, and then further isolate them into discrete environments for on-chip or external single-cell analysis. Different devices can provide

off-chip RT-qPCR or on-chip RT-PCR for single-cell applications. Comb-shape microfluidic channels with SWNT electrode can be used for active single-cell selection and sorting while the 3D-microfluidic OET can realize “from-cell-to-result” device performing on-chip selection, on-chip isolation, and on-chip analysis. The simplicity of use solves the complexity of operating conventional microfluidic devices but still provides a rapid sorting and isolation tool for cell samples with small volume. In addition, the simplicity of the device design has the potential to be integrated with automated processing to perform high throughput.

Chapter 2 Electrodes for Optoelectronic Tweezers in Microfluidics

2.1 Introduction

Microfluidic or Lab-on-a-chip (LOC) systems provide a powerful platform for biological assays due to the advantages of small volumes of solvent, sample, and reagents are moved through microchannels and various functional units. Miniaturized systems offer many advantages, including small requirements for solvents, reagents, and cells, short reaction times, portability, low cost, low consumption of power, versatility in design, and potential for parallel operation and for integration with other miniaturized devices. The advantages may be critical for valuable samples and some of bioassays. Recently, many of the exploratory functions in microfluidic system have been carried out by in a elastomeric polymer, poly(dimethylsilane) or PDMS. PDMS has distinctive properties including optical transparency, chemical stability, biocompatibility and mechanical flexibility [28, 29]. These properties are excellent for many chemical and biological applications such as DNA sequencing, polymerase chain reaction (PCR), electrophoresis, DNA separation, enzymatic assays, immunoassays, cell counting, cell sorting, and cell culture. PDMS is a flexible (Young's modulus on the order of 1MPa) material. Optical transparency (above230 nm) guarantees its compatibility with various microscopic detection techniques. Besides, the surface of PDMS can be easily modified by adsorption of certain chemical or by plasma processing. PDMS surface can be bonded to another PDMS surface or glass substrate using a brief oxygen plasma treatment. It is compatible with biological studies because it is impermeable to water, nontoxic to cells, and permeable to gases. Over the past years, it has been widely used in bio- or medical-related fields.

In addition, multilayer soft lithography (MSL) fabrication and cast molding technique have made PDMS relatively easy to fabricate. For the development of biological applications, many designs may need to be tested in the early developing stages, so the simple inexpensive fabrication process of PDMS makes it a perfect candidate for rapid prototyping. The procedures for the fabrication of multilayer PDMS structures for microfluidics have been described in 2000 by Unger *et al.* [30] This technique provides a very general method to control the fluid in microfluidic channels. The fabrication technique starts from a standard photolithography on a photoresist-coated silicon wafer. Usually, the photocurable epoxy SU-8 on a silicon wafer and different types of SU-8 give various thicknesses of structure from 1-μm to ~300-μm high. The patterned and solidified SU-8 serves as a master for fabricating PDMS structures. By overlapping two layers of the PDMS channels, the cross-channel architecture made of PDMS to be a mechanical valve (see Figure 2- 1). The membrane between two layers of channel forms pneumatically actuated valves, and the valves can be push-up or push-down style. Advantages of pneumatically actuated valves include ease of fabrication. The PDMS-based valves in microfluidics has been the basic component of various complex units of the system such as pumps [31], mixers [32, 33] etc. Its ability to support certain very useful components has pushed it to be the key material for lab-on-a-chip systems.

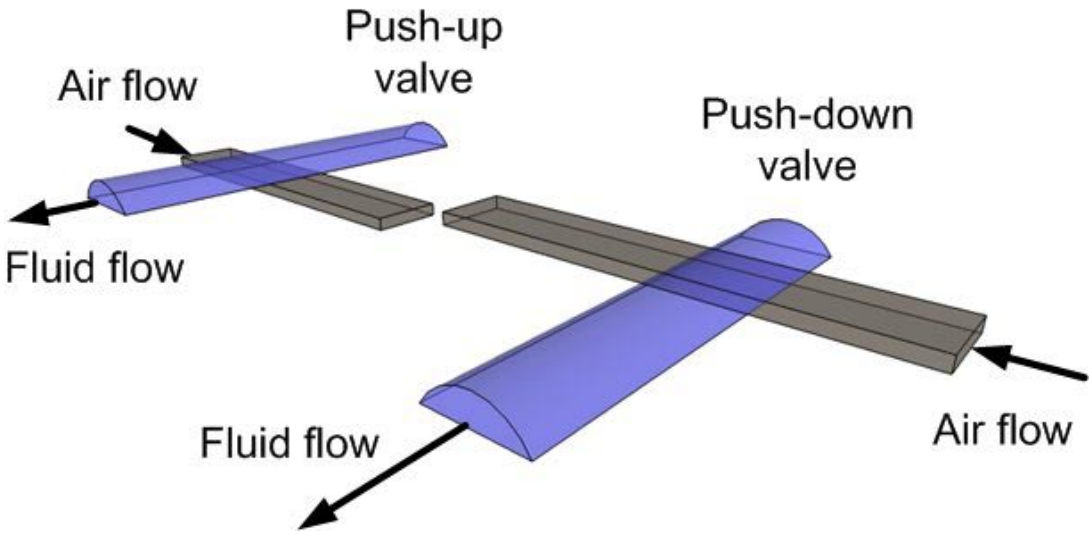

Figure 2- 1 PDMS-based switches and valves for control of fluid movement. The membrane between two layers of channel forms pneumatically actuated valves. For push-up valve, when pressure is applied the above channel, flow in the bottom rounded channel stops. For push-down valve, when pressure is applied the bottem channel, flow in the bottom rounded channel stops.

Valves fabricated using multilayer soft lithography allowed a number of different functions to be realized on-chip. Those functions include reagent metering/mixing and cell isolation/lysis. Current PDMS-based microfluidic valving system has been utilized for the analysis of single-cell RNA [34] and culture of individual human embryonic stem cells (hESCs) [35]. The valve opening time is in the order of ten to hundred microseconds, making them suitable for rapid buffer exchange applications[36]. A drawback of this system is the complexity of operation. For realizing the cell manipulation, lysis, culture, or PCR, the chips must have tens of fluidic and control channels, valves, pumps, and tubings connected to off-chip supplying system and computer. For loading/capturing a single cell into the chamber in this system, the cell concentrations of suspensions need to be adjusted to fit the optimal flow rate and the optimal spacing between cells.

Being a nun-conductive polymer constrains PDMS from many applications needed electrical controls or detections. Cell manipulation techniques such as DEP in the Chapter 1 are difficult to be implemented in the PDMS-based microfluidic devices or integrate with the pneumatically actuated valves. The lack of appropriate technique to build electrodes on PDMS constrained the board usage of being a substrate for electrical devices. Few methods have been tried to build electrode on or in PDMS. First, highly conductive fillers are usually introduced into the polymer matrix to overcome the low electrical conductivity of PDMS [37-39]. Carbon black powders, carbon nanotubes, silver particles are the materials to reinforce the electrical and thermal conductivity and the mechanical strength. PMDS can be turned into a conductive material by the addition of carbon black in a concentration higher than 10 wt% or silver particles (1-2μm) in a concentration higher than 84 wt%. Usually, the percentage of conductive fillers has to be higher than a threshold. It should be noted that the high percentage of conductive fillers makes the PDMS composite stiff, easy to break, and difficult to process.

An interesting technique to make PDMS conductive is low-energy high-dose metal ion implantation. It has been reported to be a candidate for dielectric electroactive polymer (DEAP) membranes and dielectric elastomer actuators (DEA) [40-42]. This implantation technique employs the combination of large ion doses (1~3*1016 ions/cm^2) and low energy (< 5 keV) to make the PDMS sufficiently conductive. For achieving this implantation conditions, a special implantation techniques called plasma immersion ion implantation or filtered cathodic vacuum arc (FCVA) was used. The metal ions were buried into PDMS surface (< 20 nm) and a conductive elastomer formed. Figure 5 shows the TEM cross-section images of flexible electrodes made by gold ion implantation at 5keV into PDMS thin film (20μm); the gold cluster size increases with the dose [43]. The surface of the implanted PDMS film is difficult to

distinguish because the nanoparticles are at most a few nm below the surface. However, the implantation changes the electrical and mechanical properties of PDMS. For Au doses of $1.5 \bullet 10^{16}$ ions/cm^2 implanted by FCVA at 5 keV, a resistivity of 120 Ω/square is obtained [41]. The increase of Young's modulus due to ion implantation is about a factor of 1.5 – 3 [42, 43]. The electrodes produced by this implantation method are not stiffer than the elastomer, which happens on the simply sputtering or evaporating metals electrodes [40]. The ion implanted PDMS (20-30μm thick) can achieve vertical displacement of 5-10% of their lateral size (2-3 mm). For patterning the implantation area, both shadow mask and the photolithography could be used. Unfortunately, FCVA is not a common used technique for deposition and the facility of FVCA is rare.

In order to integrate OET with PDMS-based microfluidic sturucture, a new type of electrode has to be developed due to the two reasons: (1) the unique configuration of OET, and (2) the nun-conductive property of PDMS. As the discussion in Chapter 1, OET consists of two electrodes, top and bottom electrodes, switching the particles and solutions. It means the top electrode must be built on nun-conductive PDMS surface and there are several requirements for this electrode. Several requirements need to be satisfied to realize the integration with OET. First, the electrode needs to be optically transparent to allow optical imaging and diagnostics. This is important since the amorphous silicon used in OET strongly absorb visible lights with wavelength shorter than 632 nm (red). Fluorescence excitation and observation through the amorphous silicon side is difficult and has to come from the transparent electrode side. Second, the electrode needs to be electrically conductive after deposited on the elastic PDMS surface. ITO electrodes usually crack after deposition on PDMS and cannot conduct current. Third, the

PDMS device needs to provide an interface after electrode coating that can form strong bonding with the OET surface to provide good sealing and prevent liquid leakage during manipulation.

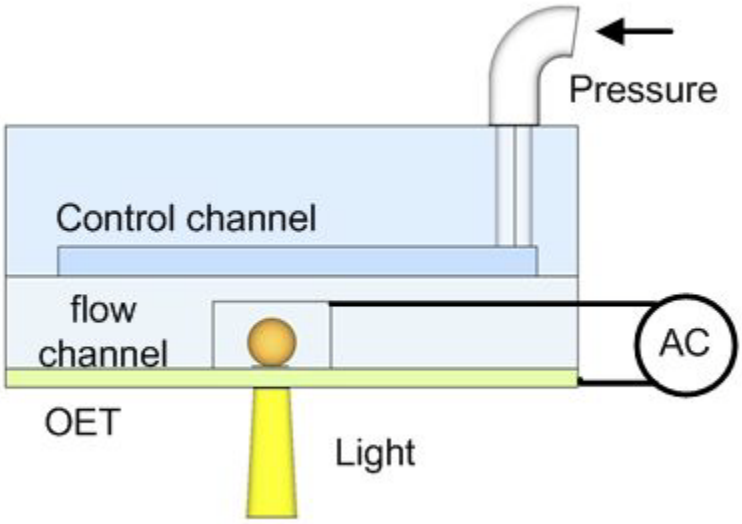

Figure 2- 2 Schematic of a microfluid integrated OET device. Unlike a conventional OET device described in Chapter 1, the multilayer PDMS microfluidic integrated OET has two layers of channels. The bottom fluid channel contains aqueous solutions carrying biological cells or particles and the top channel is used to control the membrane valve formed at the region where the top and bottom channel intersect.

The schematic of a microfluidic integrated OET consisting of an upper PDMS microfluidic channel and a bottom photoconductive OET surface is illustrated in Figure 2- 2. Unlike a conventional OET device in which a fluid chamber is formed between an ITO electrode and a photoconductive substrate, the proposed multilayer PDMS microfluidic integrated OET can have two or more layers of channels. The bottom channel contains aqueous solutions carrying biological cells or particles and the top channel is used to control the membrane valve formed at the region where the top and bottom channel intersect. This elastic membrane works as a

mechanical valve that can be controlled by pneumatic pressure to close the bottom channel and stop the fluid flow. A peristaltic pump can be achieved by actuating three valves along a channel in series.

2.2 Au-mesh Technique

Depositing a thin layer of metal, usually Ti (5-30 nm) and Au (50-300 nm), by electron-beam evaporation on PDMS is most common method to construct conductive layers on PDMS substrates [44-46]. Report shows that gold thin films formed by physical vapor deposition directly onto PDMS spontaneously forms microstructured or nanostructured waves [47, 48]. These gold thin films made on an elastomeric substrate have built-in compressive stress to form the wave structures. Research shows Depositon of 100-nm-thick layers of gold on top of a 5-nm-thick adhesion interlayer of chromium can remain electrically continous under a strain of a few tenths of a percent. The Cr/Au thin film was deposited onto PDMS by electron beam evaporation at room temperature through a shadow mask made of polyimide foil. The compressive stress in the gold films induces spontaneous wrinkling and shrinks the net length of the thin-film conductors by several tenths of a percent. This Au stripe on PDMS is the first technique we are going to describe. Figure 2- 3 is the Au-mesh electrode deposited on PDMS and integrated with OET chip. It consists of two parts: an upper Au-mesh coated chamber and a lower photoconductive OET surface. The bottom OET surface comprises of multiple layers including a 50-nm doped hydrogenated amorphous silicon (a-Si:H), a 1-μm photoconductive a-Si:H, and a 100-nm silicon dioxide. Above the OET surface, the fluidic chamber is made by PDMS. Figure 2- 3 shows the single layer PDMS, but the Au-mesh electrode can be deposited on multilayer PDMS.

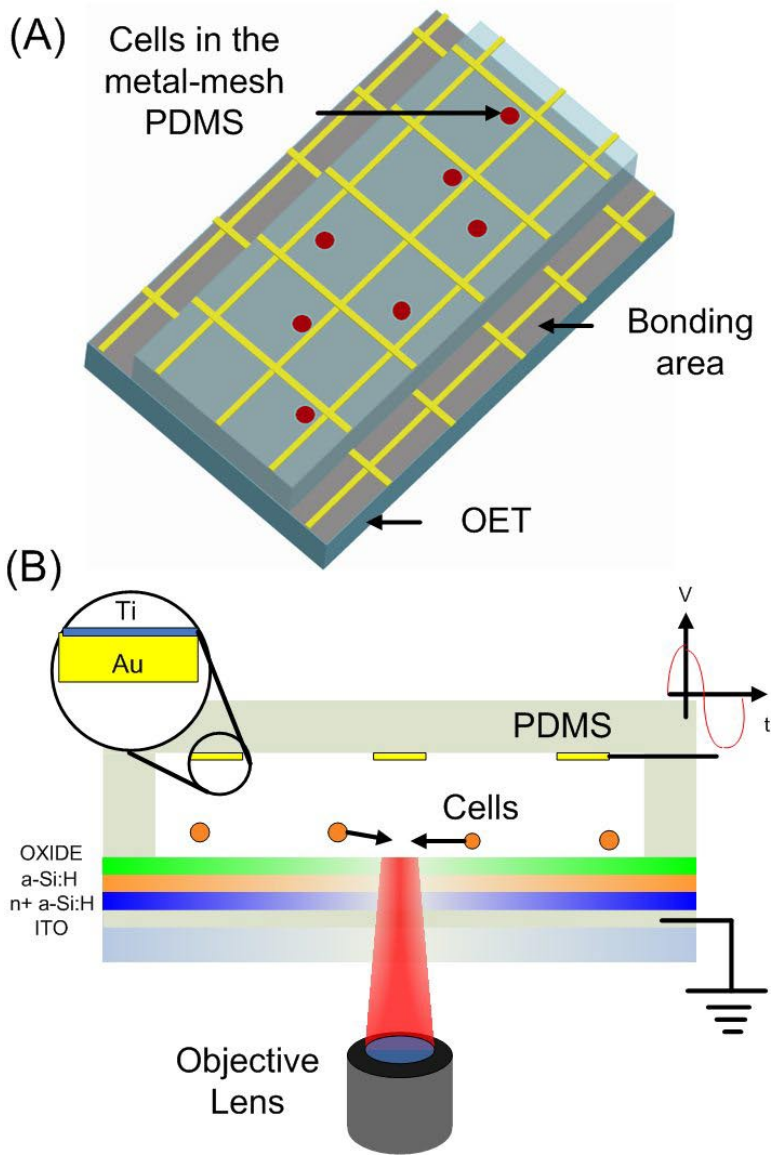

Figure 2- 3 ***Schematic diagram of a microfluidic integrated OET. The Au-mesh electrode is deposited by directional thermal evaporation through a shadow mask before bonding with OET.***

Because the thin metal layer are not transparent, to pattern the metal layer are required for OET application. There are two methods to create a pattern on the metal layer. In the first, conventional photolithography and etchants are utilized. In the second method, shadow masks are used. Compared to the second method, relative small size of pattern (~2μm) can be achieved by the first method and the resistance didn't change significantly. Based on this metal deposition

technique, Au-mesh electrode has been developed. An Au-mesh electrode is formed by two-perpendicular periodic Au/Ti stripes coated on the top surface of a PDMS channel by directional e-beam evaporation through shadow masks (Figure 2- 4(b)). Au-mesh electrodes provide high electrical conductivity in the same order of magnitude as regular metal electrodes. The empty regions between wires control their optical transparency. Since Au covers only a small area on an Au- mesh electrode, strong bonding between PDMS and the OET can be formed through plasma treatment to provide tight sealing during fluid delivery. Figure 2- 4 shows the fabrication process of Au-mesh electrodes. A shadow mask with an array of strips is used to create periodic metal strips through e-beam deposition on the top surface of a PDMS channel. The fabrication process of the shadow mask starts from a commercial 100-μm thick silicon wafer. A thin layer of PECVD oxide was deposited on the wafer as an etch mask for deep reactive-ion etching (DRIE). A strip pattern with a line width of 5-μm and a spacing of 50-μm was patterned on the etch mask by standard photolithography. The PDMS microfluidic channels and chambers are fabricated through standard soft lithography processes. After peeling off the PDMS structures from the mold, the periodic electrodes formed by 1 nm Ti and 100 nm Au stripes are deposited by e-beam evaporation on the PDMS surface through the shadow mask twice. In the second deposition, the shadow mask was rotated by 90 degrees.

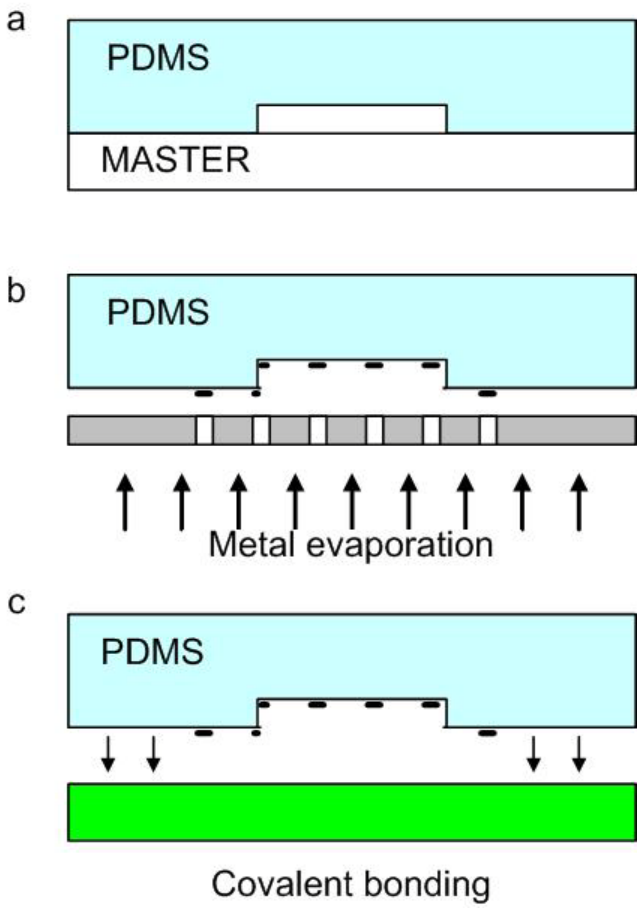

Figure 2- 4 (a) A master mold fabricated by SU-8 is used to define the PDMS microfluidic channels. (b) Evaporating through a shadow mask placed near the PDMS enables the fabrication of patterned Au/Ti wires on the upper surface of channels. (c) Covalent bonding is formed between the Au/Ti-mesh PDMS and the OET chip after oxygen plasma treatment on the bonding surfaces.

Figure 2- 5 shows both the bright and fluorescence images of 10-μm fluorescent particles positioned 100 μm underneath an Au-mesh electrode. The particles can be clearly observed under a 10× and a 50× objective lens even for particles positioned right underneath Au wires. Since Au mesh and particles are not at the same focal plane, the Au-mesh image blurs out when the imaging plane is on the OET surface. It can be expected that the larger the separation gap between OET and the electrode, the larger the blurring. Also, the higher the magnification of the

objective lens is, the less the shadowing effect. Furthermore, decreasing the width of Au wires can further reduce the shadow effect of Au mesh.

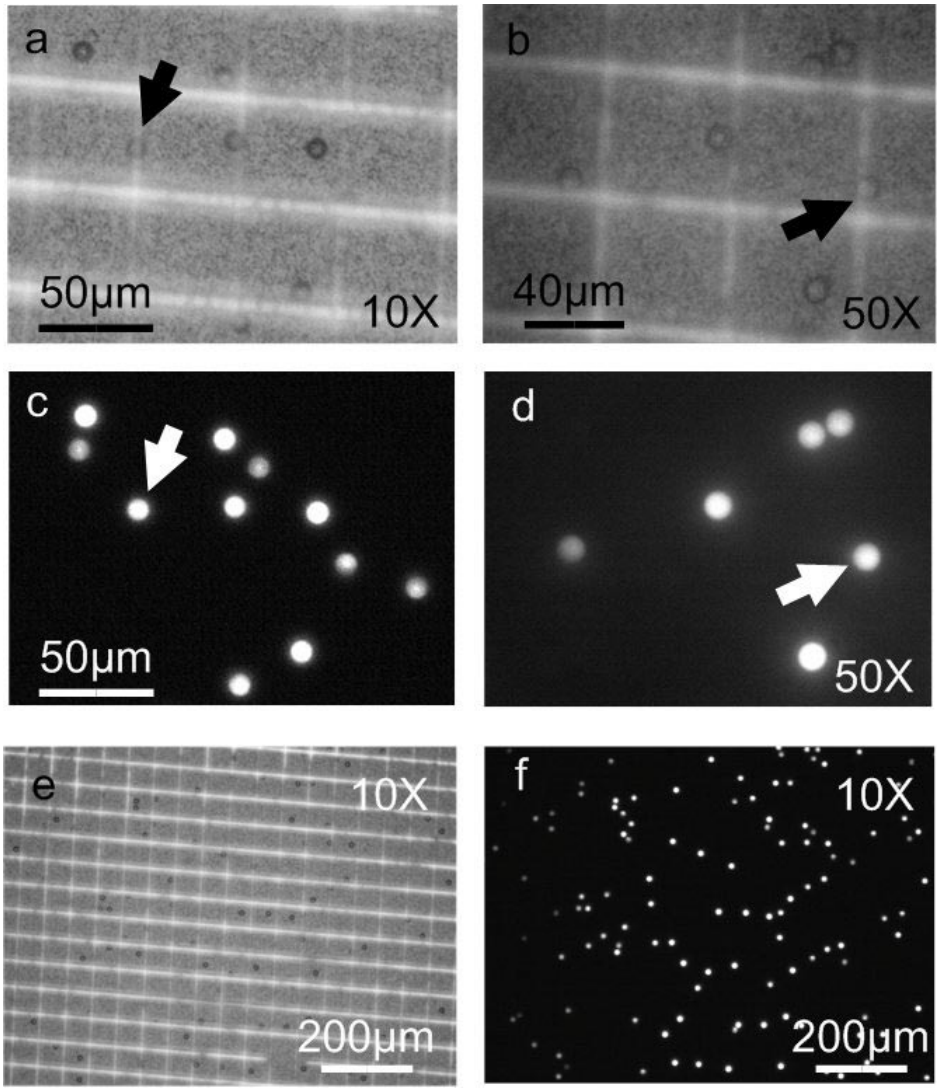

Figure 2- 5 (a) (b) bright-field images and (c) (d) fluorescent images of 10-μm particles at 100-μm underneath the Au mesh. The arrows point the particles below an Au wire. (e)(f) the entire field of view of 10X objective images.

To verify the performance of OET manipulation using an Au-mesh electrode, a HeNe laser was used as the light source to induce a virtual electrode on the photoconductive surface. Nalm 6 cells were first suspended in an isotonic buffer, and then flowed into the microchannels using a syringe pump. After a light beam turned on a virtual electrode, Nalm 6 cells experiencing positive DEP forces are observed to move toward the light spot as shown in Figure 2- 6 (a) and (b).

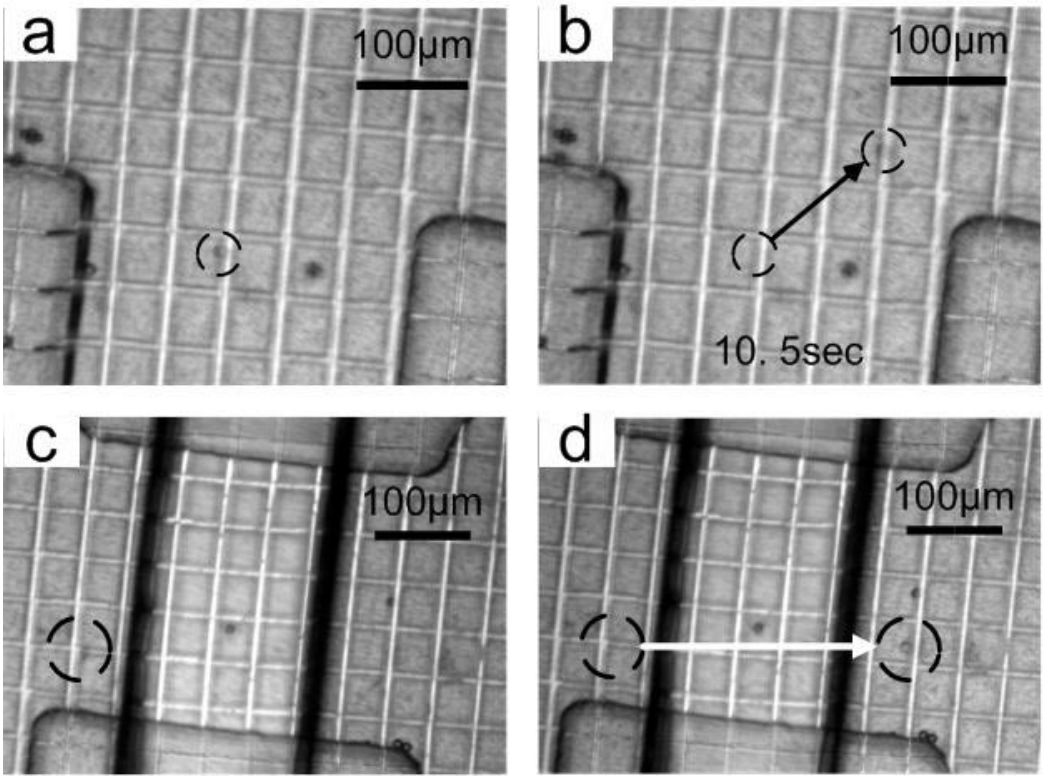

Figure 2- 6 (a)(b) A Nalm 6 cell trapped by a light spot (the dish circle) is transported by OET in the microfluidic channels (c)(d) Transport of a single Nalm 6 cell trapped by OET in the multilayer PDMS channels. There are two layers of channels. The region between two black lines is a conrtol channel above the flowing channel where cells are.

One potential drawback of Au-mesh electrode is the highly non-uniform electric field near Au wires. If cells or particles are near these wires, strong DEP forces will be induced on them. This effect turns out to be not severe when particles or cells are manipulated near the OET surface since this highly non-uniform field decreases rapidly away from the wires. This property allows Au-mesh OET to manipulate cells or particles near the photoconductive surface smoothly as a continuous electrode. This can be confirmed by the finite element method (FEM) simulation showing the electric-field distribution induced by a light beam on an Au-mesh OET device as shown in Figure 2- 7(a). The geometry parameters used in simulation is based on real device dimensions. The width of Au-wire electrodes is 5μm and the spacing is 50μm. A 50-μm high chamber is filled with medium having a conductivity of 0.01 S/m. The photoconductivity of a-Si:H is assumed to follow the Gaussian distribution profile with a peak conductivity of 0.1 S/m and a FWHM spot diameter of 16.6 μm. The non-uniform electric field induced by Au mesh is limited to regions close to the top surface (shown in the 47.2 μm curve in Figure 2- 7(b)) and quickly decays in the vertical direction. At regions near the OET surface, Au-mesh induced field gradient is negligible compared to that induced by the light beam (1.8 μm and 7.5 μm curves in Figure 2- 7(b)).

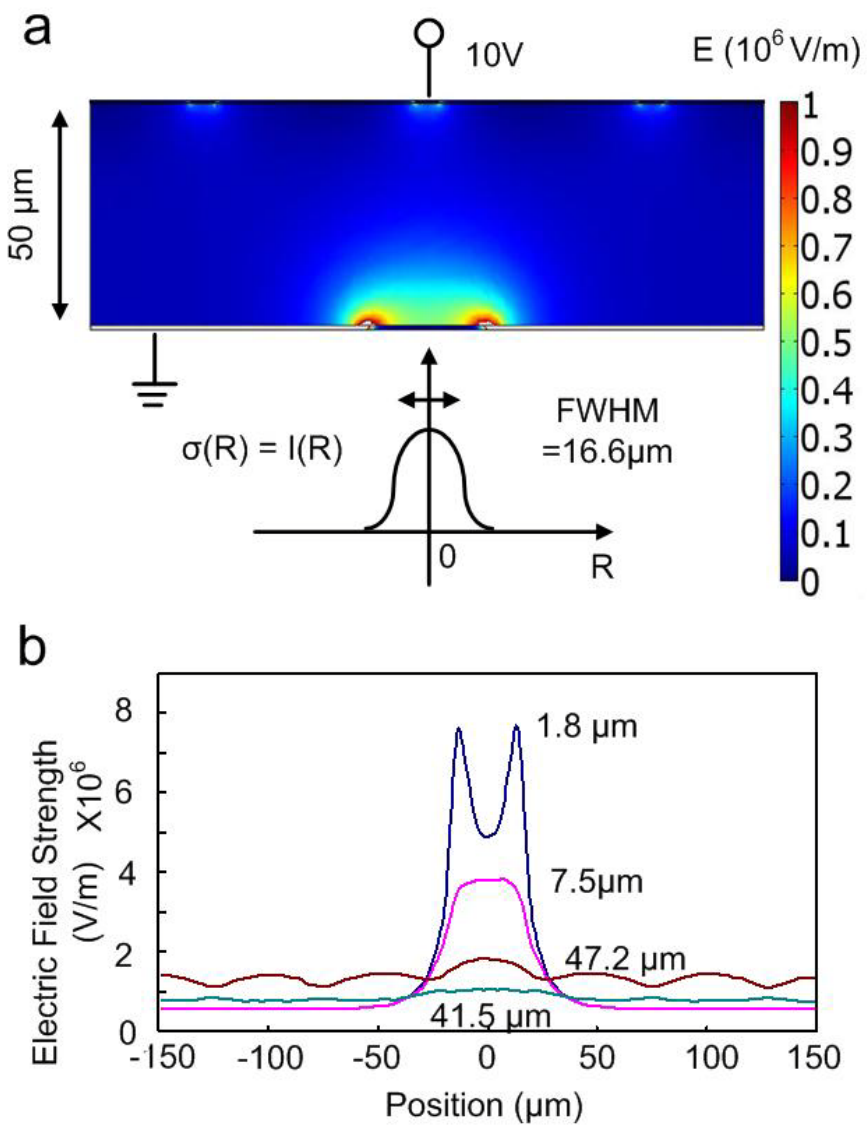

Figure 2- 7 (a) Electric field pattern in the liquid layer when the photoconductive layer is turned on by illumination of a 16.6 µm FWHM light spot. (b) The electric field distribution at different heights above the photoconductive layer.

Although Au-mesh electrodes provide high electrical conductivity and high optical transparency, there are several drawbacks. First, there is a trade-off between the height of

channels and the density of Au-mesh since the electrode is discrete. The non-uniform electric field induced near Au wires will affect OET manipulation when the height of channels becomes small. Increasing the channel height or reducing the spacing between Au wires can help reducing this effect. Another limitation comes from the fact that metallic films, despite more deformable than ITO, tend to peel off from PDMS surface after large deformation which also creates cracks. As a result, Au-mesh electrodes can only undergo large mechanical deformation once before failure. In Figure 2- 6(c) and (d), a Nalm 6 cell was transported across a deformable PDMS membrane valve coated with Au-mesh electrode. This Au-mesh electrode failed after the PDMS membrane valve was pushed down to close the flow channel.

2.3 Single-Wall Carbon Nanotube Electrodes

We present SWNT thin-films electrodes here. SWNTs exhibit high conductivity (106S/cm) and films made by randomly distributed SWNTs have also shown to be a potential candidate in flexible electronics. SWNT thin films with thickness in the range of 10-100 nm perform low sheet resistance and high optical transparency as well as robust mechanical flexibility[49, 50]. Devices such as solar cells [51], thin-film transistors [52], light emitting diodes [53], and electrowetting devices [54] have been demonstrated using SWNT thin film with comparable to those for which ITO electrodes used. Recently, researches about CNT thin film embedded in polymer suggest that the electrical stability and mechanical robust of CNT films can be improved [55, 56]. Devices made by CNT films within polymer membranes show the enormous potential for applications on microfluidic platforms [57, 58]. We utilize the properties of SWNT thin films to build the electrodes in PDMS microfluidic channels for OET manipulation. The OET using SWNT electrode is schematically illustrated in Figure 2- 8. The top Au-mesh electrodes are

replaced by SWNT thin films which are homogeneous, optically transparent, and electrically conducting. The continuous SWNT electrodes don't have the discrete problem of Au mesh. The transparency also provides the observation from top side. In addition, the flexibility of SWNT thin film compatible with PDMS substrate solves the cracking problems of Au mesh. Embedding SWNT thin film into the PDMS matrix prevents the wash-away by solutions. After an AC bias is applied to the top SWNT electrode and the bottom photoconductive electrode, the light-induced DEP forces are generated by light patterns as well.

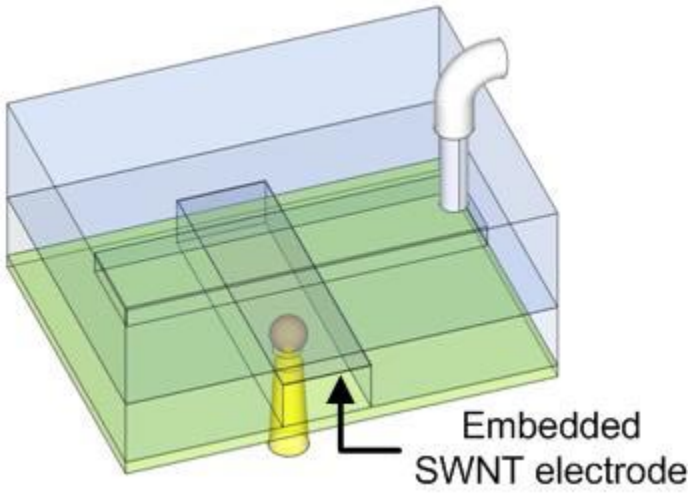

Figure 2- 8 The schematic of a microfluidic integrated OET device using a SWNT embedded flexible PDMS electrode as the top channel surface and the deformable check valve.

The procedure to fabricate SWNT thin film in PDMS is outlined schematically in Figure 2- 9. To get uniform CNT films, we adopt the method based on a vacuum filtration [59]. This approach utilizes vacuum-filtering a surfactant-based suspension of SWNTs onto a filtration membrane to form networks on the membrane. In order to make highly dense SWNT suspension, commercially available purified arc discharge nanotubes with purity above 90% was purchased (Carbon Solutions, Inc.). SWNT were dissolved in 1wt% sodium dodecyl sulfate (SDS) solution

to prepare solution-based SWNT. This highly concentrated SWNT suspension was ultrasonically agitated using probe sonicator for ~10 minutes. To remove the carbon particles and impurities, the suspension was centrifuged at 14000 rpm for 30 min. A porous anodic aluminum oxide (AAO) filter (Anodisc 47, Whatman Inc.) was used in vacuum filtration. The suspension falls through the pores while the CNTs are trapped on the surface of AAO filter, so the SWNT film homogeneity is guaranteed by the filtration. The density of SWNT network can be controlled by the concentration and the volume of the suspension.

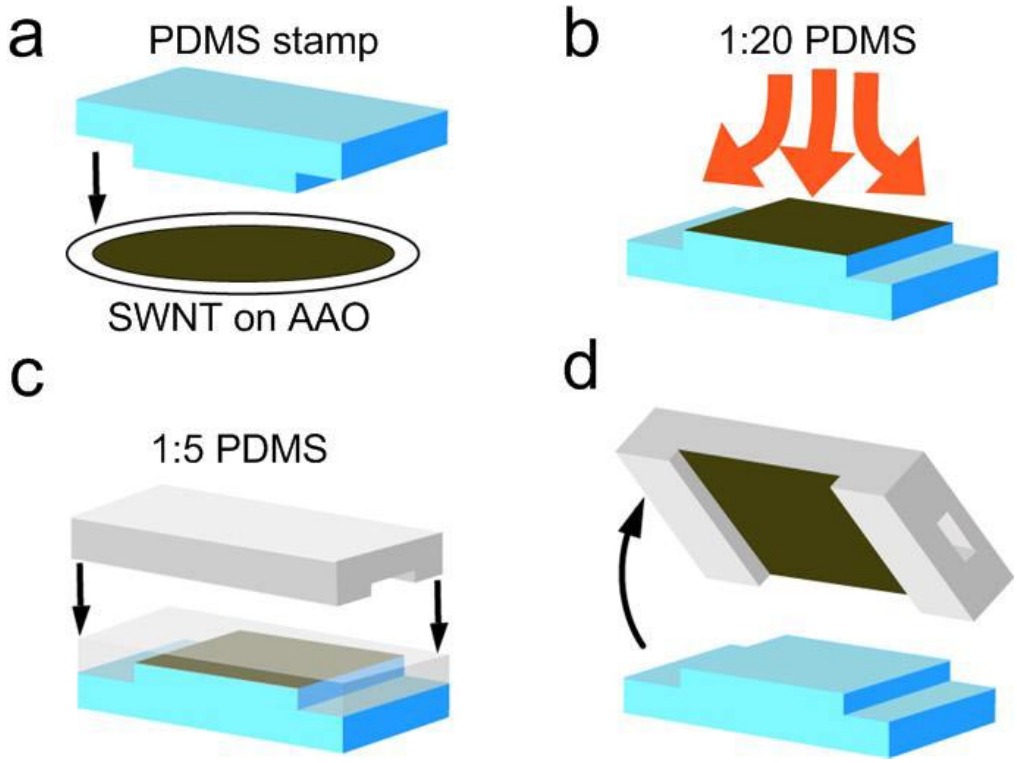

Figure 2- 9 The fabrication process of embedding a thin layer SWNT network in a multiplayer PDMS microfluidic structure.

A PDMS stamp is then used to transfer the SWNT thin film from the filtration membrane [60]. To fabricate the PDMS stamp, a master mold was made by using standard photolithography using a negative photoresist (SU-8 2025, MicroChem corporation) on a silicon wafer. Poly-dimethylsiloxance (Sylgard 184, Dow Corning) with a ratio of 10 base: 1 curing agent was poured onto the master mold and cured at 65 ^{o}C for 4 hr. A PDMS stamp with a pattern of microfluidic channels could be peeled off from the Si wafer. Before the stamp contact the filtration membrane, it was treated by trichloro(1H, 1H, 2H, 2H-perfluorooctyl)silane (Sigam-Aldrich, Inc.), a chemical release agent that lowers the adhesive forces between the PDMS stamp and the SWNT thin film [61]. The treated PDMS stamp was then pressed in contact with the SWNT network on the AAO filter paper (Figure 2- 9(a)). After the PDMS stamp is removed, the SWNT network is transferred onto the extruding surface of the PDMS stamp. This PDMS stamp with a SWNT thin film was then used as the mold for casting microfluidic channels.

To cast the microfluidic channels, an uncured PDMS precursor at the ratio of 10 base: 1 curing agent was poured onto the PDMS stamp, and baked in an oven. The uncured gel-like PDMS precursor infiltrates the vacant regions in the SWNT network during the curing process. The cured microfluidic channels were then be peeled off from the mold with a SWNT thin film embedded near the top surface of channels. This fabrication technique can be used to embed SWNT thin film on multilayer PDMS microfluidic devices. To achieve that, the uncured PDMS precursor at a ratio of 20 base: 1 curing agent was spin-coated on the PDMS stamp to create a thin membrane (Figure 2- 9(b)). A top thick PDMS layer made with a ratio of 5 base: 1 curing agent is pressed to contact the thin PDMS layer. These two layers are bonded after cured (Figure 2- 9(c)). The cured PDMS with a top control channel and a thin film SWNT embedded bottom PDMS channel can be peeled off from the first PDMS stamp as shown in Figure 2- 9(d). This

multilayer PDMS channels with an embedded SWNT thin film electrode on the top surface of bottom channels including the membrane valve locations was then bonded with an OET device through oxygen plasma treatment.

In our fabrication process, the PDMS stamp is not only used as the mold for casting other microfluidic channels but also transferring a SWNT thin film to the top surface of a channel. This fabrication process is compatible with the standard soft lithography process. Figure 2- 10(a) shows the microscopic image of the SWNT electrode embedded in a multiplayer PDMS microfluidic device. Since the SWNT electrode exists only on the top surface of the flow channels, this promises a clean surface for forming strong covalent bonding between PDMS and silicon dioxide surface of an OET device. Figure 2- 10(b) shows the SEM image of a thin film SWNT embedded into the cured PDMS matrix. Embedded SWNT networks can provide better electrical stability and mechanical robustness.

To examine the optical transparency of SWNT electrodes, 10-μm fluorescent particles were pumped into a SWNT OET device. Figure 2- 10 (c) and Figure 2- 10(d) are the bright field and the fluorescence images of 10-μm fluorescent particles underneath a SWNT electrode. Three particles highlighted with arrows are located in the membrane valve location where two layers of PDMS channels cross. The relation between the measured sheet resistance and the optical transmittance at 632 nm is plotted in Figure 2- 11 (A). The optical transparency and electrical conductivity of SWNT electrodes are highly dependent on the carbon nanotube purity, tube length, and dispersion quality of the films. The transparency and the sheet resistance can be controlled by the thickness of SWNT films, which can be adjusted by the amount of SWNT in the dispersion solution. Experimental results have shown a linear relationship between sheet resistance and optical transparency. The electrodes with sheet resistance from ~350 to ~550 ohm

per square have 55 to 80% optical transparency measured at 632 nm. The electrical resistance of the SWNT electrode increased when the strain increases. The measurement was applied by following steps. A thin film PDMS with SWNT-embedded region in 5mm * 5mm was made by the procedure described above. The SWNT PDMS film was secured on a two-stage platform separated by a 5mm gap. Electrical leads were secured by epoxy on both ends of the PDMS region (at the outer edge, not within the 5mm gap). Initial reading of the resistance was measured for the 5mm gap (with no strain). To increase the percentage of the strain, one end of the stage was capable of moving horizontally through a rotational knob that had distance markers on it. The marker on the knob was used to assess the distance stretched and the correlating resistance was measured with the resistance machine. The resistance varies with the strain would be recorded. After reaching the maximum strain we set in each experience, we released the strain by releasing the knob. The resistance can decrease back to its original value before reaching a threshold strain value. The SWNT embedded PDMS thin film electrode is capable of reproducing their electrical conductivity for strain up to 40 %. (Figure 2- 11(B))

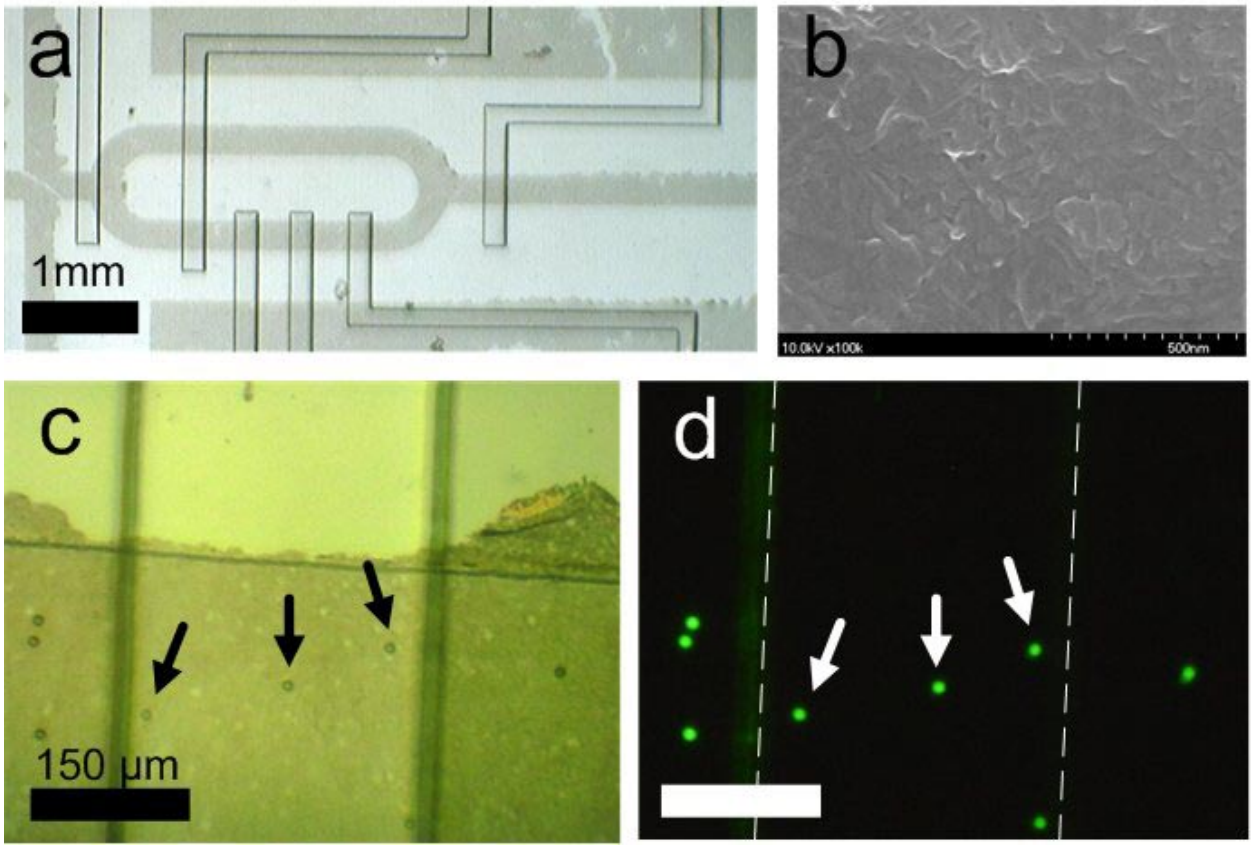

Figure 2- 10 (a) A microscopic image of SWNT embedded valves and channels in multilayer PDMS microfluidic structures. The channel is bonded on an OET chip. (b) A SEM image of SWNT network embedded in the surface of PDMS. (c)(d) Bright field and fluorescence image of 10 µm fluorescence particles underneath a SWNT electrode.

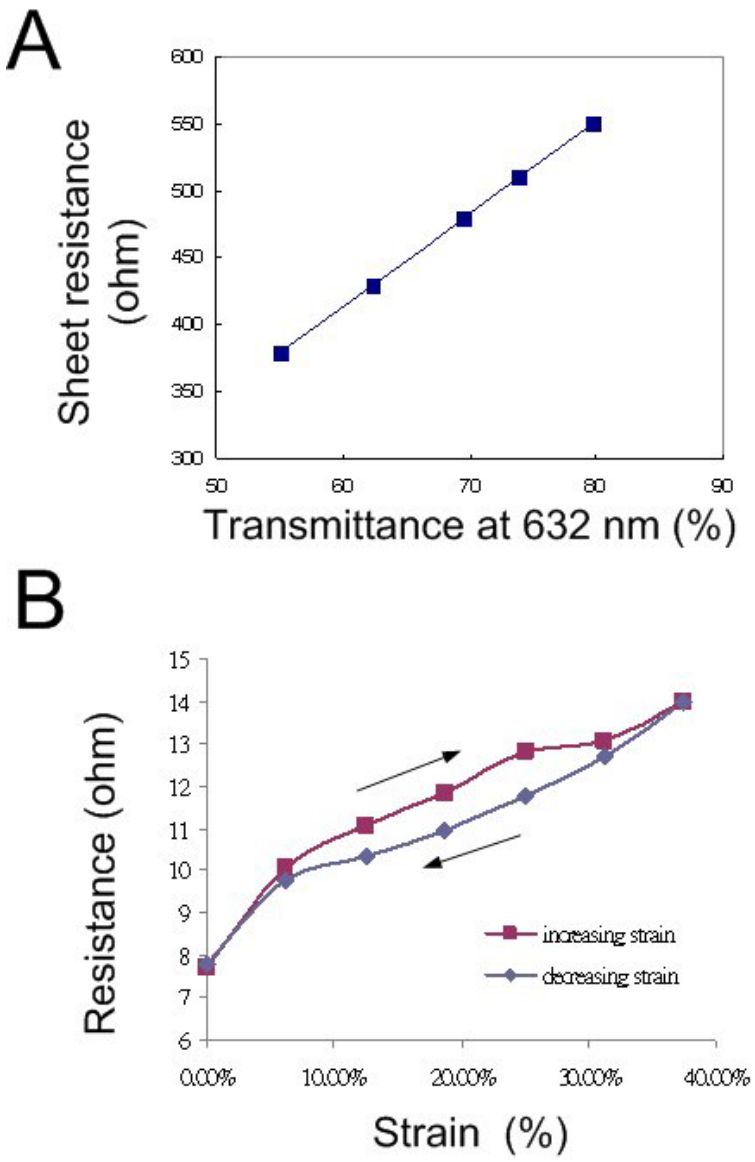

Figure 2- 11 (A) Measured sheet resistance of SWNT embedded PDMS electrodes and its relation with optical transmittance at 632 nm. (B) Resistance vs. percentage of strain on SWNT embedded PDMS. Data show the SWNT embedded PDMS can retain the conductance after releasing the stress.

In a SWNT OET device, all the flow channels (top layer) and the control channels (bottom layer) are 300-μm wide, so the area of the valve was 300 μm × 300 μm and the height of bottom channel was 18 μm. The valve could be pushed down to completely close the bottom flow channel by applying a pressure in the top channel. Figure 2- 12 shows a series of pictures of

valve function. The dye solution was pumped into a SWNT OET device by a constant pressure of 1.5 psi. The white arrows are the flow directions of dye solution. First, a pressure of 25 psi was applied into the top channel in the right-hand side, the PDMS membranes deformed and the dye solution was stopped by the two closed valves. The dye solution moved when the two valves were open and the valve in left-hand side was close. After the dye solution was filled in the entire flow channel, the color change in the valve region indicates the closing of the valves.

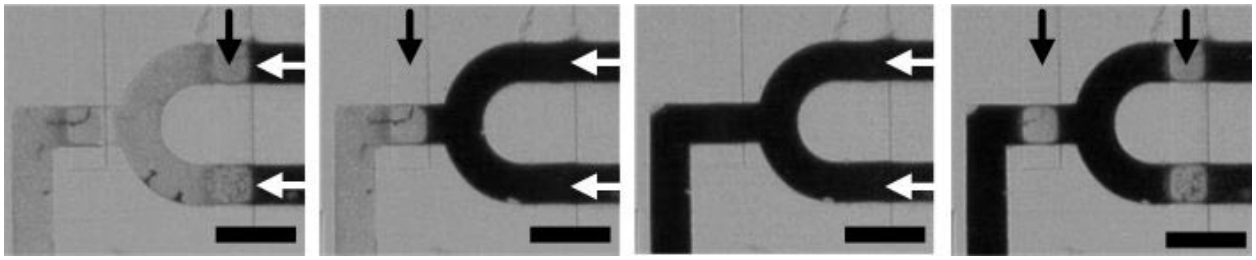

Figure 2- 12 A series of pictures showing the valve function by deforming the SWNT membrane electrode. The white arrows are the flow directions of the dye solution in the flow channels. The black arrows show the pressure sources to deform the membranes. The dye solution can be stopped by pushing down the membrane. The scale bars is 600μm.

To verify the the microfluidic integraed OET platform, we couple a DMD based projector (BenQ, MP730) with an inverted microscope. The projection lenses of the projector are removed and replaced by a 4X objective lens to focus the light to photoconductive surface. 10-μm particles were firstly suspended and flowed into the microchannels in OET using syringe pumps. The microfluidic integrated OET was connected to a sinusoidal ac bias (100 kHz, 10Vpp). In the OET devices, the light illuminated areas on the photoconductive surface correspond to the high electric field regions. Particles experienced negative DEP forces which repel them away from the

light spots. Figure 2- 13(a) and Figure 2- 13(b) are the consecutive images showing a 10-μm particle was transported across a deformable PDMS membrane valve by the projection light.

The performance of OET manipulation using a SWNT embedded PDMS thin film electrode has been compared with a regular ITO electrode. A HeNe laser which was set on an up-right microscope was used as the light source to trigger virtual electrodes. Therefore, the incident laser light is from the bottom side of the photoconductive layers, avoiding the optical transmittance difference between two top electrodes (ITO and SWNT). 10-μm particles were diluted in KCl solution of 0.07mS/cm and injected into a liquid chamber which was formed by an ITO electrode or a SWNT electrode. The tests were under the application of an ac bias with different voltage but in the same liquid chamber and at the same frequency, 100 kHz. Figure 2-13(c) shows the average velocities of 10-μm particles under different voltages. The SWNT electrodes behave like regular ITO electrodes under these operation conditions. The particle transport speed using the SWNT electrode is similar to a regular ITO electrode. We can estimate the DEP forces in both electrodes are almost the same.

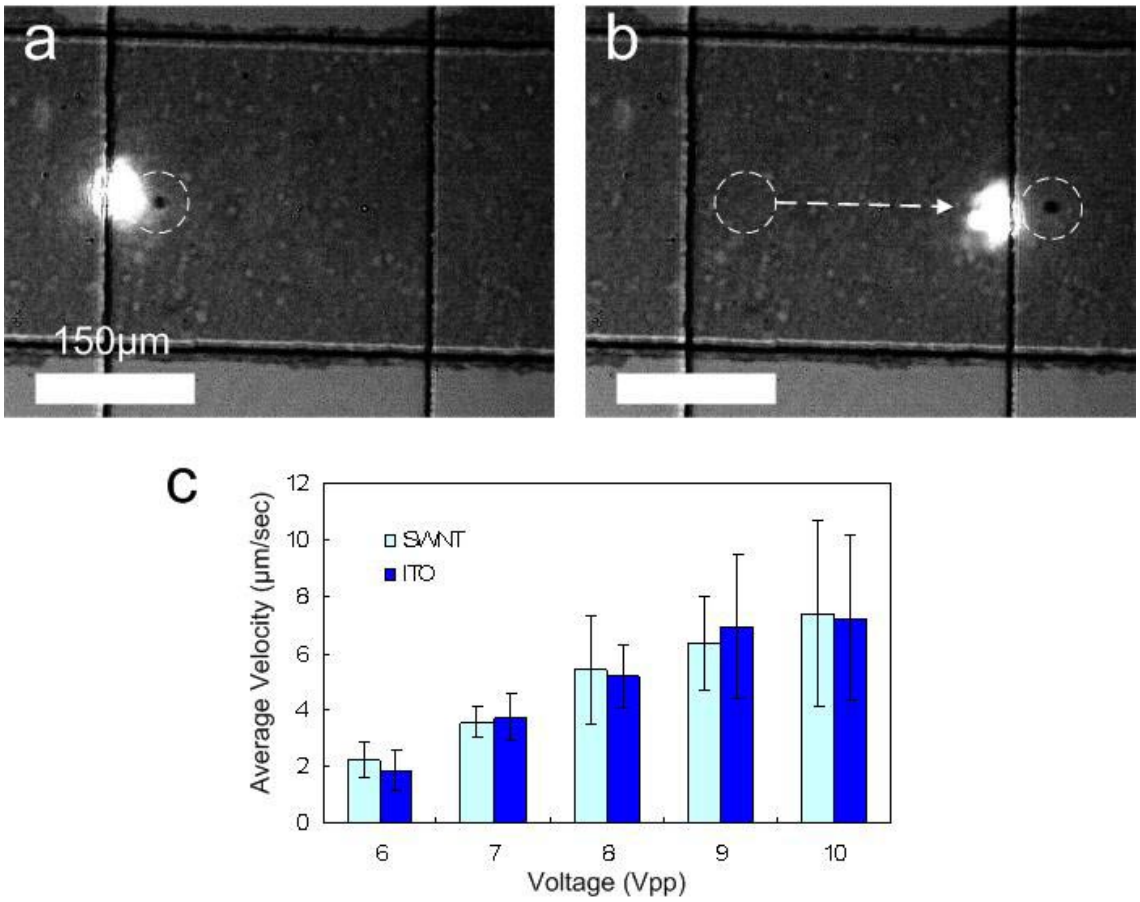

Figure 2- 13 (a)(b) Transport of a 10-μm particle by light across a membrane valve on an OET integrated multilayer PDMS device. The scale bars is 150μm. (c)Comparison of particle moving speed in OET using ITO electrode and SWNT embedded PDMS electrode. The light intensity is 1.5 W/cm^2 and the applied frequency is 100 kHz.

2.4 Conclusion

We have successfully demonstrated OET manipulation of cells and polystyrene beads in PDMS microfluidic devices. To replace the conventional ITO electrodes, two different types of electrodes have been introduced. Au-mesh electrodes are optically transparent, electrically conductive and able to provide covalent bonding to substrate. However, the Au-mesh electrodes

still suffer from the cracking issues. Therefore, a novel method to embed a conductive, transparent and flexible SWNT thin-film electrode into PDMS has been developed. The SWNT electrodes not only simplify the design of the devices but also address the cracking issue of Au-mesh electrodes. OET platforms with SWNT electrodes were made for manipulating micro particles. This successful integration steps up OET platforms to many useful applications. Furthermore, this fabrication method can be integrated with multilayer PDMS technique. The ultimate usefulness of the fabrication of SWNT electrodes can lie not only in OET platform but also in many other microfluidic applications.

Chapter 3 Three-dimensional Microfluidic for OET

3.1 Introduction

The detection of heterogeneity with single-cell resolution is critical in study of stem cell differentiation, gene expression, and origin of disease. Microfluidic devices have been developed as a powerful tool to analyze various intracellular components including DNA, RNA transcript levels, and identification of protein [2]. The capability of handling small reaction volume provides advantages of increasing sensitivity and precision, economical reagents cost, and automation. However, almost of the microfluidic platforms for single-cell analysis require off-chip cell sorting (i.e. FACS), sample preparation, and off-chip cDNA synthesis. The missing of a robust on-chip cell sorting mechanism limits the advanced integration of the off-chip processes with the other steps for single-cell analysis. To address this problem, we develop an optoelectrofluidic platform combining OET and Three-dimensional (3D) multilayer microfluidic structure enabling robust cell and fluid control on one chip. This 3D microfluidic OET is different from the ones we described in Chapter 2. The multilayer microfluidic OET in Chapter 2 is based on monolithic PDMS while 3D microfluidic OET is utilizing 3D fabrication techniques to build unique PDMS thin film spacer between two rigid substrates. The thin film spacer can further be built on conventional OET platforms to create a new microfluidic tool with on-chip optical cell manipulation and fluid control functions. In this chapter, we first do a brief review of 3D multilayer PDMS and the limitations, and then introduce the new method to overcome the limitation to integrate the 3D multilayer PDMS with OET.

Fabrication of via-holes (the vertical channels) on a Polydimethylsiloxane (PDMS) thin membrane is a difficult and attractive issue for researchers who work in multi-layered

microfluidic systems. The 3D microfluidic with via channels mainly started from the efforts put by Prof. Whitesides' research group. A variety of fabrication methods for PDMS through-hole patterning have been reported.

The PDMS membrane-sandwich method and membrane add-on technique were proposed in 2000 [62]. Authors employed two Si masters mold with two-level photolithography to make thin PDMS membranes. After that, the thin PDMS membrane is transferred to another PDMS slab, or another PDMS membrane. Then, one of the masters should be removed. The results showed a successful fabrication of a basket-weave structure. Jeon *et al*. modified the previous method to build a polymeric 3D microfluidic valve and pump made by stacking patterned PDMS layers with microchannels and vias [63]. The previous method was modified by replacing one of the Si master with Teflon sheets. Although only single check valve structure was shown, this work on 3D via layer has demonstrated the concept of 3D microfluidic and a method showing how to fabricate, handle, and bond PDMS membranes. The PDMS membrane was fabricated by curing the uncured PDMS between a clamped Teflon sheet and Si master, and then the membrane was lifted from the Si master using a type. These methods require pressure applied on Teflon and Si master to ensure that the vias were not blocked by PDMS that seeped between the Teflon and the features during curing. The concept to pressurize Teflon stamp to make via is modified to a PDMS stamp by Zhang *et al*. in 2010 [61]. Teflon stamps are replaced with PFOCTS-coated PDMS stamps, which can merge the transfer step and membrane fabrication in one step. 3D PDMS chips by an add-on process were shown by stacking five layers of PDMS membrane. One method similar to membrane-sandwich method was using inhibition process to manufacturing a densely perforated PDMS membrane [64]. This method sandwich a PDMS membrane between a dual-level Si master mold and a treated glass stamp. The stamp glass was

treated by silanized chelating compound aminoethylaminopropyltrimethoxysilane (AEAPS). AEAPS can inhibit the curing of PDMS and prevent the residual membrane issue in the membrane-sandwich method. The fabrication procedure in this chapter is modified by the membrane-sandwich method. One advantage of this method is the easy integration of dual-level SU-8 master mold, which allows rounded channels; another is the stacking of membrane provides an opportunity to bond to two rigid substrates. For the applications, Chiu *et al*. employed this fabrication technique to pattern cell on glass surface [65]. Multiple types of cells can be deposited on the surface (i.e. thirty-six cell types can be patterned on six by six well array). A paper-based microfluidic has been demonstrated by using similar 3D fabrication concepts[66]. Pattern papers which is substituted for PDMS channels and cut double-side tapes which is substituted for via holes were stack layer by layer to form wave structures. Although paper-based device distributes microliter volumes of samples into arrays of detection zones without any external pumps, this unique dipstick-like device is very difficult to integrate with other structures and still left out by the main microfluidic platforms.

The protruding-mold method uses hybrid mold with two photoresists, a short one for channels and a tall one for vias [67]. A PDMS membrane is formed on a mold by spun at high speed. The PDMS membrane is bonded to a thicker PDMS slab while the protruding features (taller photoresist) are not covered by PDMS. Thus, the protruding features result in vias which connect top and bottom channels in different layers. Luo *et al.* modified this method by removing the protruding features after the PDMS membrane being cured [68]. The new method can shorten the interconnection thickness, but manually removing the protruding structures is hardly controlled during the membrane fabrication.

Solid-object printing is one of the methods to build 3D PDMS microfluidic channels [69]. A solid-object printer was used to replace masters for the fabrication of microfluidic devices in PDMS. In spite of the relative low spatial resolution (features size >250 μm), the solid-object printer provides an alternative. This method doesn't need a multiple photolithographic steps and mask alignment for 3D microfluidic structures, especially for tall stuructures (>1mm). For simple and tall 3D channels, solid-object printing is an easy way for fabrication. It only needs two masters and one bonding step for the two halves for a basket weave pattern for crossing, nonintersecting channels. However, this method can't be used to fabricate complex structure which is more than two layers of channels, compared to "membrane sandwich" method. For 3D OET application which needs two rigid glass substrates, the method won't be able to provide the thin film PDMS membranes, complex pneumatic valve structure, and flat surfaces.

Wu *et al.* demonstrated a method for fabricating 3D microfluidic channel systems in PDMS with complex topologies and geometries [70]. The channel geometries are knots, spiral channels, and braided channels, which are fabricated by manually inserting pre-made 2D channel structures into a special master mold with additional photoresist posts on top of the normally used photoresist features. This method is based on pre-made 2D PDMS tubing to form 3D structures rather than stacking via channels or via layers, so complex and smooth 3D channel system can be achieved. It can also offer a potential solution to the interface issues of the PDMS microfulidic platforms. However, the need for manual work to assemble pre-made channels limits the cross sections of the interconnections to be relatively large dimension and the positions of the pre-made channels are not precisely controlled.

Some integration between OET and microfluidic channels have also been reported [25, 26]. Continuous sorting of microbeads was demonstrated by patterning a photoresist on OET chips,

but photoresist cannot provide good sealing to ITO glasses and cannot provide valve functions to control the liquid. On-chip generation and manipulation of water droplets has been demonstrated by using PDMS to form the channel. The PDMS channel was formed by blowing an air jet on the photoresist pattern through a narrow nozzle [71]. The devices show single-layer PDMS integration with conventional OET. The lateral-field optoelectronic tweezers (LOET) has been integrated with electrowetting-on-dielectric (EWOD) [72]. In this system, microbeads were manipulated using OET while droplets were manipulated by EWOD. As a result, conventional OET platforms with two rigid substrates were not really merged with soft lithography, which limits OET from more complex microfluidic functions such as single-cell mRNA analysis or on-chip RT-PCR. In this chapter, we are going to outline a new 3D PDMS fabrication method to facilitate conventional OET with microfluidic channels and switching valves. This membrane method results in the creation of 3D channel structures. Section 3.2 outlines the novel method for making a flat perforated membrane. The method follows the concept of sandwich uncured PDMS between a stamp and a master mold to form membranes and then remove the master molds to transfer the membranes to target substrates. Furthermore, we modify the stamps and master molds to produce flat membranes. The detail will be shown in Section 3.3. The results and discussions are shown in Section 3.4.

3.2 3D microfluidic for OET

The structure of the platform is shown in Figure 3- 1. Two layers of elastomeric structures made by PDMS are sandwiched by two rigid ITO glass substrates. The bottom ITO glass is coated with a photoconductive layer for light-induced DEP forces. 3D microfluidic technique is utilized to fabricate “through patterns” (i.e. channels without top PDMS walls). The through patterns on

perforated membrane are an essential an element facilitating OET function. The through patterns on the two thin PDMS layers are aligned and overlapped, so cells in the channels can be directly exposed to top and bottom electrodes for dynamic DEP manipulation. PDMS pneumatic valves are also formed by the membrane between the control channel and the link channel. When the control channel is pressurized, the membrane will be pushed up and the valve will be closed.

Microfluidic pneumatic valves are implemented by multiple soft lithographies. Each device consists of two layers with elastomeric structures with a bottom control layer and a top flow connection layer.

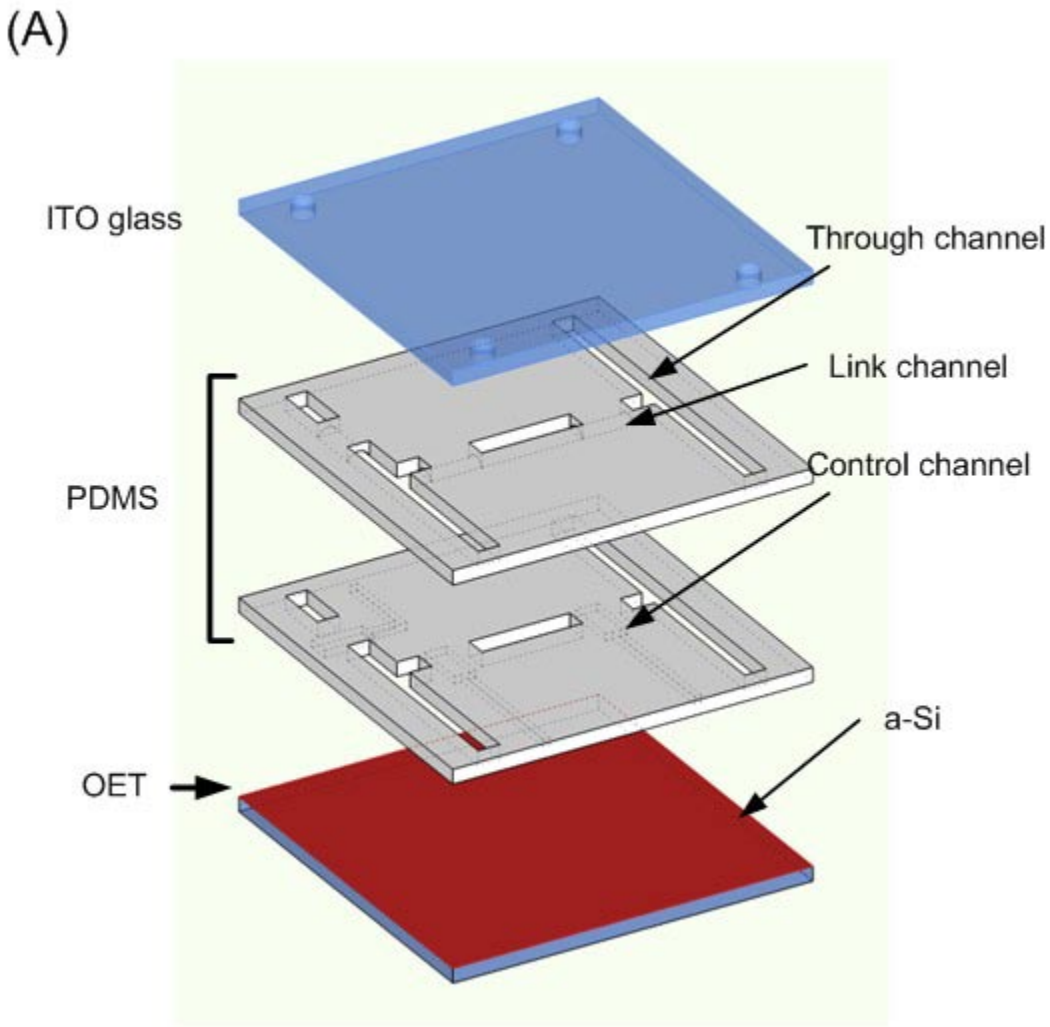

Figure 3- 1 ***Structure of the microfluidic integrated OET platform. Two layers of elastomeric PDMS with through patterns are sandwiched by two ITO electrodes. The bottom ITO is deposited with a photoconductive layer. The membrane between link channel and control channel forms a push-up valve.***

3.3 Fabrication Method

We present an alternative approach for fabricating interconnections. The process is developed in collaboration with my colleague, Mr. Yu-Chun Kung. The approach is based on membrane-sandwich method (mentioned in 3.1). Similar to the membrane-sandwich method, a PDMS membrane is formed between a mold with channel features and a stamp mold. However, the photoresist features master molds are replaced with a PDMS soft mold and the stamp is modified to result in a membrane to eliminate the protruding features along the channels. The fabricated PDMS membrane is easy to be bonded to other PDMS membranes or rigid substrates to form a 3D channel structure. The procedure for producing this 3D channel OET involves making photoresist master mold, casting a PDMS mold, embedding a glass into a PDMS slab, pressing the slab to form PDMS membranes with through-holes patterns, and transferring the membrane to the substateds. The fabrication of such through-holes membranes was different from previous procedures, which is able to overcome the protruding features along the channel structures resulting in impossibility of bonding to flat rigid surfaces or substrates. In this manner, we have fabricated 3D connected channel structures on conventional OET consisting two rigid substrates (i.e. ITO and a-Si on ITO). We believe that this novel technique can realize complex approaches on OET platforms.

The fabrication process starts from photoresist features on two silicon wafers to produce soft lithography molds. One of the molds is for control layer and the other is connection layer

(Figure 3- 2A). There are two levels of pohtoresist on the two molds, high-feature photoresist (SU8 2075) and low-feature photoresist (AZ4620 or SU8 2025). The high-feature photoresist is used to make through-hole channels. The low-feature photoresists are used to form the control valves and the connection channels. The master molds of control layer were fabricated with two lithographic steps: the channels for valves control were defined by a thin layer of SU8 2025 photoresist, and the OET areas were made by high-feature photoresist (Figure 3- 2B). The master molds of connection layer were also fabricated with two lithographic steps. First, the openings for OET operation were made by SU8 2075 to deposit OET functional areas with 60 um height. Second, the flow channel connected two OET functional areas were defined by AZ4620 photoresist. The AZ4620 was rounded to facilitate the valve function (Figure 3- 2B). Because of the thermal properties of AZ4620, a low-feature photoresist can have round cross sections. Such the features are able to produce flow connection channels with round cross sections, which can be closed by valves. PDMS gel was poured onto the two master molds to make two PDMS slabs with the inverted features (Figure 3- 2C). These two PDMS slabs were treated with trichloro(1H, 1H, 2H, 2H-perfluorooctyl)silane (PFOCTC, Sigam-Aldrich, Inc.) (see Figure 3- 2D). PDMS gel at ratio of 1:10 curing agent: base was poured onto glass slides then PDMS slabs were then placed on glass slides with the PFOCTC treated surface facing the master mode (Figure 3- 2E). These two PDMS master molds were spin-coated with Cytop (Asihi Glass, Japan) and baked at 150 °C for 8hrs to make surfaces hydrophobic (Figure 3- 2F).

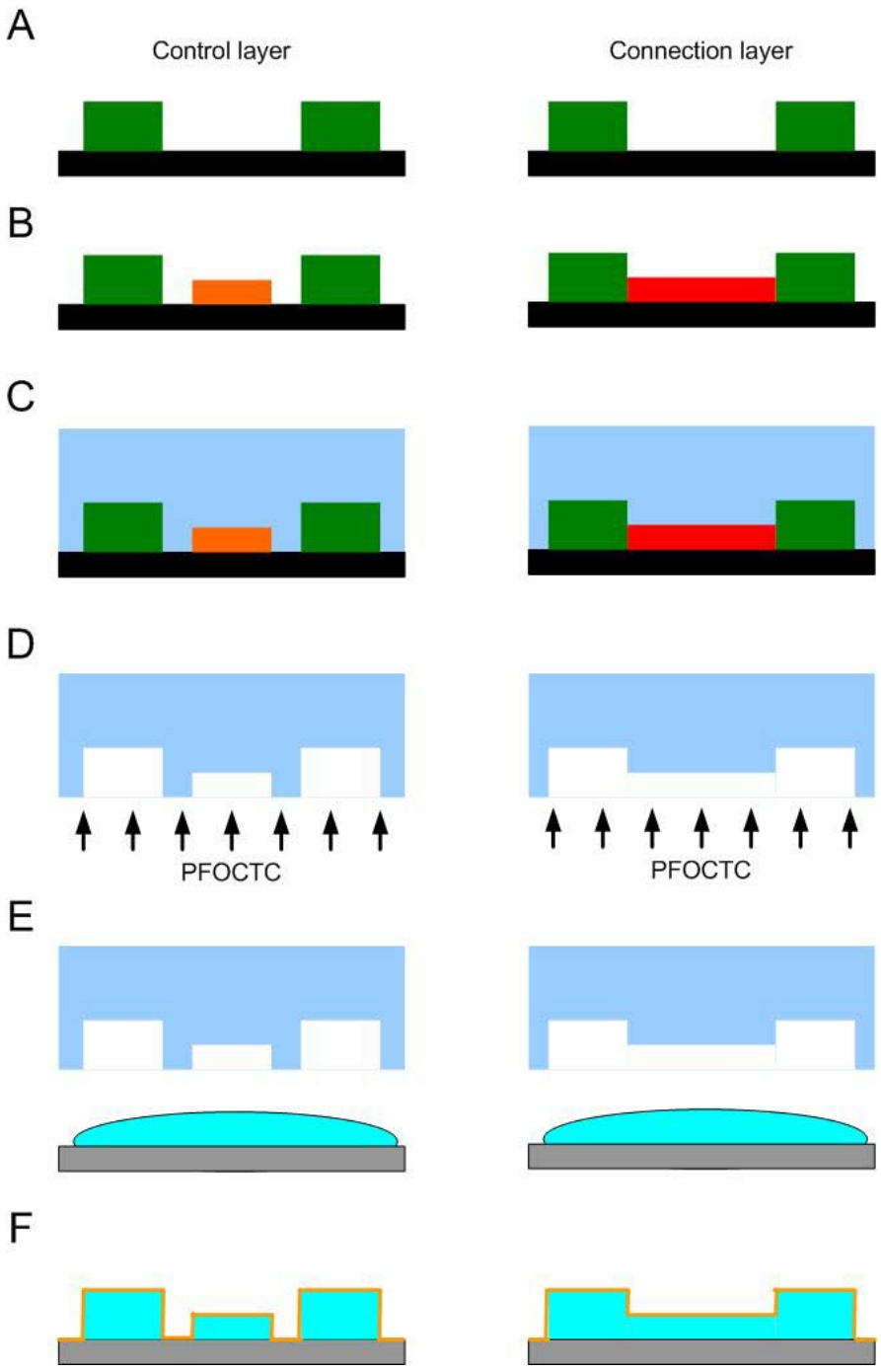

Figure 3- 2 Fabrication process flow of PDMS master molds for 3D PDMS channels. (A) Si wafer with high-feature SU-8. (B) Patterning low-feature SU8 and AZ4620. (C) Pouring uncured PDMS to make the inverted molds. (D) PFOCTC treatment on the inverted PDMS molds. (E) press uncured PDMS to make the final PDMS molds. (F) Final PDMS molds are coated with CYTOP.

To make a perforated membrane by the sandwich method, the PDMS membranes are usually formed by pressing a thick PDMS stamp on the mold. In order to make the membrane flat, a solid surface rather than PDMS slab is needed. Because the surface of PDMS stamps can be deformed when the pressure is applied, the deformation of the stamp means protruding features on the PDMS membranes. Figure 3- 3 shows the method to avoid the protruding features by embedding a glass into a PDMS stamp. PDMS (mixture of Silgard 184 at a ratio of 10 : 1) is cured in an oven at 80 °C for about 2 h to form a PDMS slab (Figure 3- 3A). The slab was treated with oxygen plasma and bonded to a glass slide (Figure 3- 3A). Then the glass surface was covered by thin PDMS surface which will further be treated with PFOCTC (Figure 3- 3B). PDMS gel at ratio of 1:10 (curing agent: base) was poured onto PDMS-glass modes which was made by method described in Figure 3- 2. To make a perforated membrane, the PDMS stamps were then placed on PDMS-glass modes with the PFOCTC treated surface facing the modes (Figure 3- 3C). A weight was loaded on it to apply constant pressure and then the device was baked to solidify the PDMS gel. The through channels can be formed by pressing the stamps toward the PDMS-glass modes. The thickness of the membrane is equal to the height of the high-feature photoresist posts (60 μm). Then the PDMS-glass modes can be directly removed from the membrane due the CYTOP coating (Figure 3- 3D). When detaching the transferring PDMS slab and the PDMS membranes, the detachment between PDMS and PDMS-glass mold can easily be achieved because that the bonding force between FPOTS and PDMS is higher than that between the PDMS and Cytop. The membranes stayed on the PDMS stamps for the next transfer step. The advantage of this method is that the PDMS membrane can be assemble to the substrates layer by layer. No matter how many layer need to be stacked, all the membranes can be fabricated by the method in Figure 3- 3.

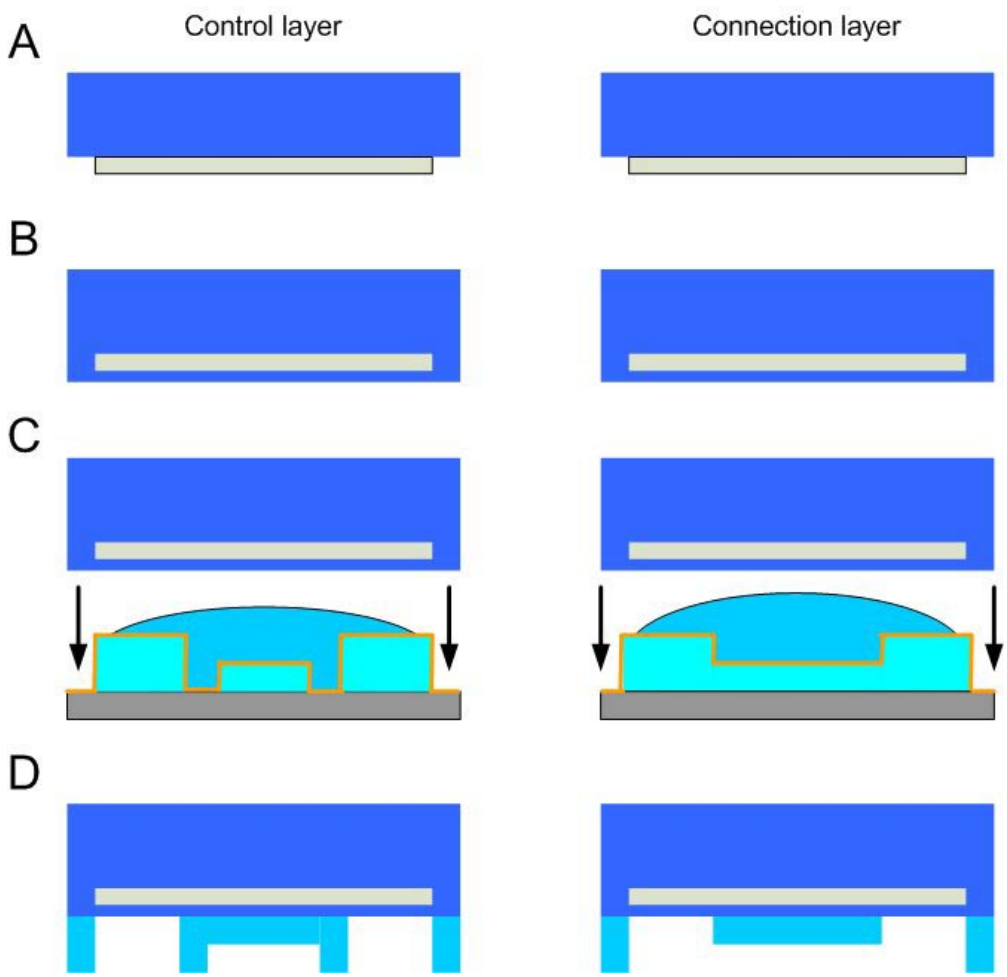

Figure 3- 3 Schematic procedure of making PDMS stamps and PDMS membrane with through-hole channels. (A) Thin glass slides are bonded to PDMS slabs by oxygen plasma treatment. (B) The slabs are covered by thin PDMS polymer and treated with PFOCTC to form the final stamps. (C) The stamps are pressed toward the PDMS-glass mold made by following the procedure described in Figure 3- 2. (D) After peering the PDMS-glass modes, the membrane will stay on the transfer stamps.

The Schematic procedure of making a 3D microfluidic OET device having a multilayer PDMS valves structure is shown in Figure 3- 4. After detaching from the master mold, the membrane with control layer could be transferred to OET surfaces by oxygen plasma treatment (Harrick Plasma cleaner) (Figure 3- 4A). Then, the transferring slab could be taken off, leaving

the patterned thin layer well linked to the OET substrate (Figure 3- 4B). The connection-layer structure could be easily obtained by repeating the same process to stack another thin patterned PDMS membrane on the control layer (Figure 3- 4C). Finally, the top ITO electrode was deposited a SiO_2 layer by PECVD and bonded to the device by oxygen plasma treatment (Figure 3- 4D). A push-up valve (see Figure 2- 1) is formed where the connection channels and control channels cross each others. The difference of height of the high-feature photoresist (SU8 2075) and the low-feature photoresist (SU8 2025) on the control layer mold gives a gap to form the PDMS membrane for a push-up valve. The rounded AZ4620 photoresist on the connection layer mold promises the closure of the push-up valve. The reason we use PDMS-glass molds is to overcome the issue of residual PDMS [73]. The issue happens when the spacer or the high-feature photoresist is rigid and not flat.

Figure 3- 5 shows a picture of a fabricated 3D microfluidic OET device having structures of pneumatic valves. Fabrication of this 3D microfluidic OET device is followed the processes in Figure 3- 2, Figure 3- 3, and Figure 3- 4. Two perforated membranes are sandwiched between two rigid substrates, ITO glass and OET chip. The through channels in the two membranes are aligned and stacked to form the final through channels shown in Figure 3- 5A. The through channels are exposed to top ITO and bottom OET surface, and it allows light-induced DEP works in the through channels (Figure 3- 5C). The push-up valves can be closed by applying pressure to the control channels (Figure 3- 5B and C). By carefully designing the channels layout, both optical manipulation and flow control can both be realized in one chip. Compared to the SWNT electrodes described in Chapter 2, the 3D microfluidic OET has several improvements. First, the properties of top ITO electrodes are better than the SWNT electrodes. The commercial

ITO glasses are more transparent and more conductive than the SWNT electrode. Second, the push-up valve in 3D microfluidic channels can be fully closed due to the rounded profiles [30].

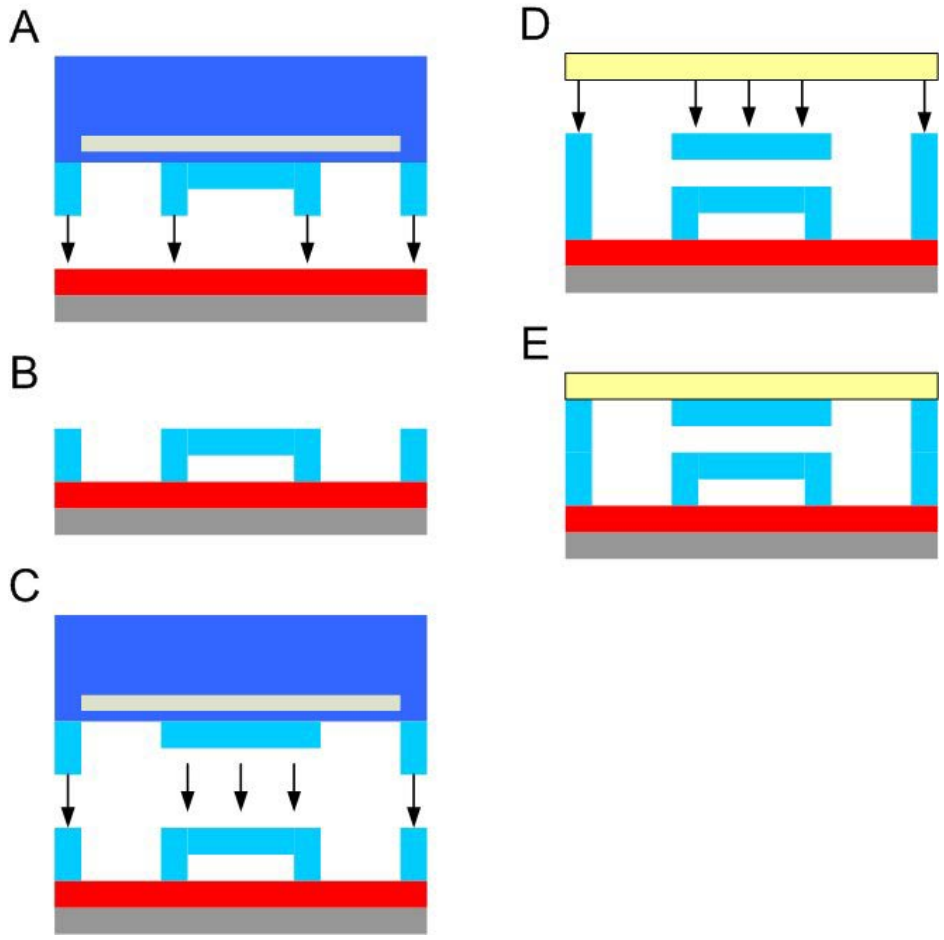

Figure 3- 4 Schematic procedure of making a 3D microfluidic OET device having a multilayer PDMS valves structure. (A) Bonding of control layer to OET chip. (B) Removing the stamp and transferring the membrane to OET chip. (C) Bonding of connection layer to the first layer. (D) Bonding of ITO electrode to the device. (E) The 3D microfluidic OET device.

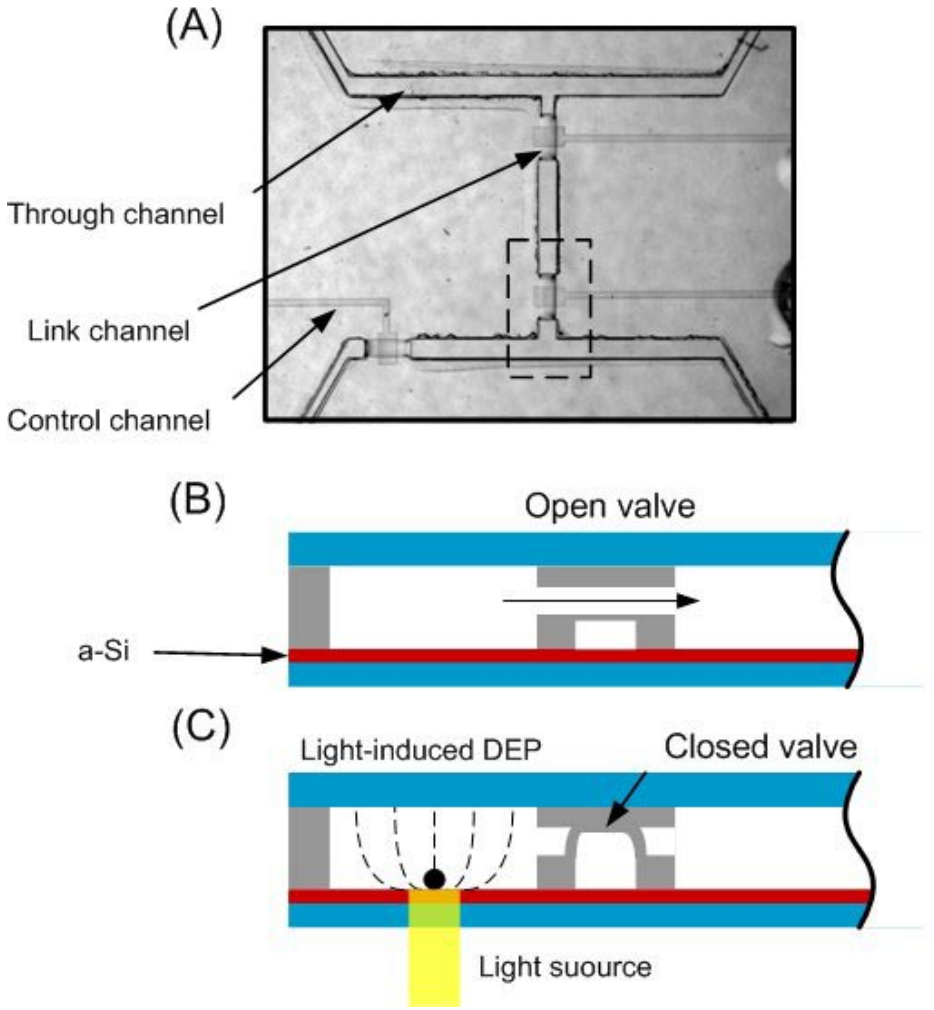

Figure 3- 5 (A) Top view of the device fabricated by stacking the four layers in Figure 3- 1. (B, C) The side views of the circled region in (A). Cell manipulation in OET is achieved by light induced DEP forces on a photoconductive surface. Liquid is not allowed to pass when the membrane is pushed up by pressurizing the control channel.

3.4 Results and Discussions

The pictures of switching valve are shown in Figure 3- 6. It shows that a multilayer valve can be operated between two rigid substrates. Dyed liquid could pass the link channel while the valve was open (Figure 3- 6A). Valve sealing can be inspected by observing the channel edges under

an optical microscope. It appears as a distinct, visible edge. Incomplete sealing as with a rectangular channel appears as a distinct and visible edge in the flow channel, while the complete sealing gives a continuous contact and almost invisible edges. (see Figure 3- 6 and Figure 2- 12). The pneumatic valve in Figure 3- 6 was operated by applying 25-psi pressure into the control channels.

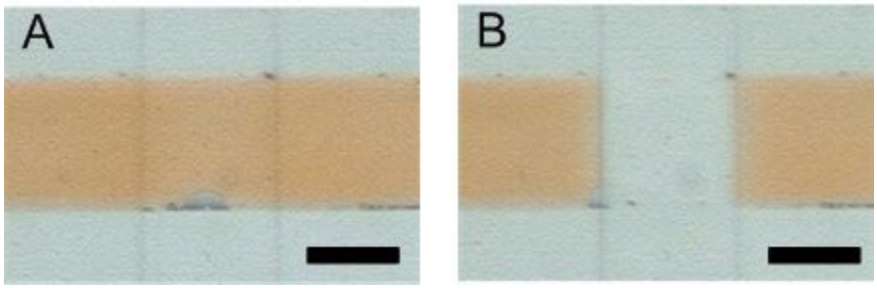

Figure 3- 6 Switching valve in 3D microfluidic device. (A) Dyed water was pumped into the fluid channel when valve is open. (B) The valve is closed by pressurized the control channel. The scale bars are 200 μm.

The OET function was verified by manipulation of HeLa cells. Figure 3- 7A and Figure 3- 7B are the bright-field images showing the transportation of the target cell in the manipulation chamber. In Figure 3- 7, the targeted cell circled by white marks was manipulated by a single light spot (positive DEP). First, the 3D OET has many advantages. The top ITO electrode provides a very clear window for cell observations and high-resolution image-based sorting can be achieved by using 3D OET. PDMS side walls compose the microfluidic channels and valves. The PDMS channels are sealed by oxygen plasma and don't have leaking issue which exists in the case of SU-8 side walls. Third, the ITO electrodes are possible to further be integrated with the large-area detection microscopy (on-chip holographic microscopy) described in the next chapter.

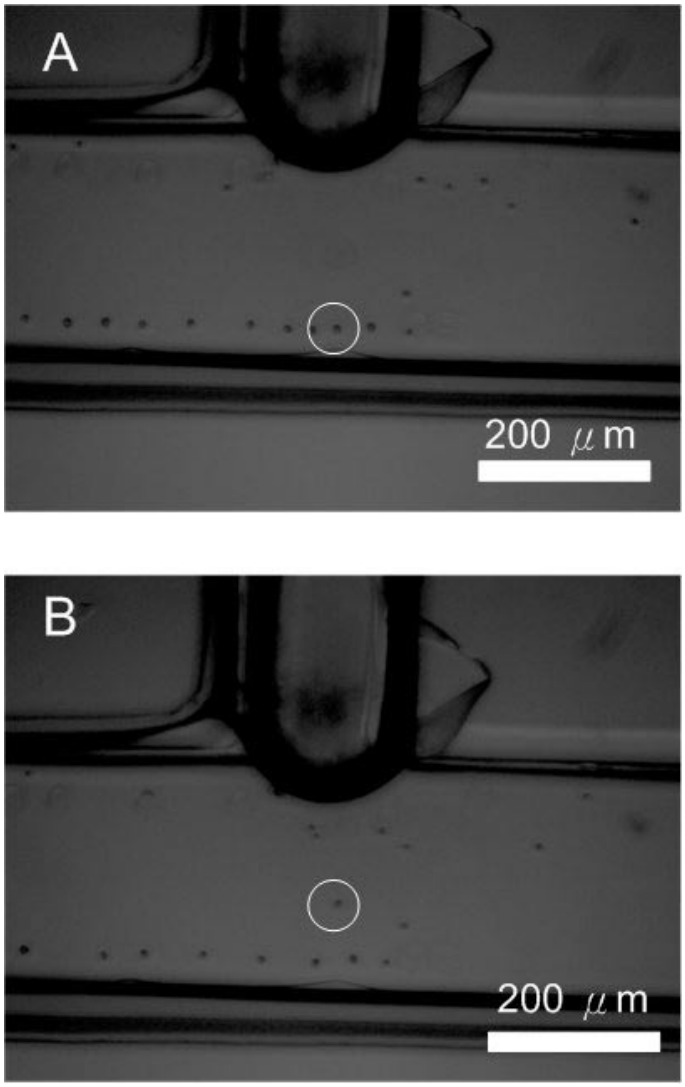

Figure 3- 7 (A)(B) Transport of a HeLa cell by light on an 3D microfluidic OET device.

Chapter 4 Large-area Detection for Optoelectronic Tweezers

4.1 Introduction

Approaches that enable large-area noncontact manipulation and detection of microparticles or cells play important roles in miniaturized systems for chemical and biological analysis [74, 75]. Manipulation mechanisms utilizing optical, electrical, magnetic, and acoustic forces have been demonstrated [76, 77]. Optoelectronic tweezers (OET) is one of such platforms that has been developed to manipulate versatile biological and dielectric objects such as polystyrene beads [1], semiconductor microdisks [78], nanowires [2], DNA molecules [15], proteins [79], sperm cells [80], bacteria and mammalian cells[5, 20, 81]. OET system can easily be extended for large-area manipulation (i.e., > 100 cm^2) because of its simple and pattern-less structure which only incorporates a photoconductive layer on an indium tin oxide (ITO) glass. This pattern-less photoconductive layer serves as virtual electrodes to induce dielectrophoresis (DEP) manipulation when light images are projected on its surface. Massively parallel control of individual objects in a large-area chip can be easily realized by dynamically changing the projected light patterns. Although large-scale individual manipulation has been achieved by using this OET platform, most of the manipulations are passive type, which means the projection light patterns are programmed before knowing where the objects are. To realize active and interactive manipulation of a large array of randomly distributed cells and particles, a real-time, massively parallel particle detection function is required. In conventional OET, particle position feedback function is provided by processing the images recorded through an objective lens, which typically has a field of view (FOV) of for example ~ 1-2 mm^2 and significantly smaller than the workable area of OET platform. Therefore, the number of objects that can be

simultaneously monitored and inactively manipulated by conventional OET systems is severely compromised.

To overcome the issue of small detection area in conventional OET, here we demonstrate a unique platform which integrates OET with lensfree holographic on-chip microscopy, an emerging technique that removes the need for conventional objective lenses and uses digital computation to achieve microscopic imaging over a large FOV [82]. This lensfree holographic microscopy technique provides a FOV that is e.g., more than two orders of magnitude larger than conventional lens-based microscopy schemes and has been demonstrated with various biological applications including blood analysis [83], waterborne parasite screening [84], and male fertility testing [85]. Recently, deep-sub-micron resolution and >18 cm^2 FOV [86, 87], were also demonstrated for this technique with an extendibility into three-dimensional imaging [88-90]. This lensfree on-chip microscopy technique furnishes OET with a complementary detection and imaging function to enable large-area, programmable, parallel light-induced DEP manipulation of microscopic particles or cells with real-time position feedback.

4.2 On-Chip Lensfree Holographic Microscopy

The lensfree on-chip imaging approach presented in this section is described in Figure 4-1 . In this technique, which is based on digital in-line holography [91]. The liquid containing sample of interest is placed directly on a CCD or CMOS sensor. The distance between the objects and the sensor is typically 0.5–5 mm. The illumination source can be a simple light emitting-diode (LED) coupled with a pinhole or an optical fiber which is placed at a distance of 4–10 cm from the sample. When the LED light propagates over a few centimeter distance, the spatial coherence increases. When the partially coherent light hit the objects, the scattered light

and the unperturbed light are propagating to the sensor plan. The two waves interfere with each other and form a interference pattern on the plane. The recorded interference pattern can be described as

$$I(x,y) = \left|R(x,y,z_0) + s(x,y,z_0)\right|^2$$

$$= \left|R(x,y,z_0)\right|^2 + \left|s(x,y,z_0)\right|^2 + R(x,y,z_0)s^*(x,y,z_0) + R^*(x,y,z_0)s(x,y,z_0) \quad \textbf{Eq. 4- 1}$$

where R(x,y,z) is the reference wave and s(x,y,z) is the object wave. There are four terms in Eq. 4- 1. The first one is the intensity of the background wave, the second is the intensity of the object scattering light, the third and the fourth are the interference of the background and the objects. Because the distance between the objects and sensors are close, the field of view of this microscopy can be as large as the sensor sizes. Furthermore, the numerical reconstruction of the holographic image can provide microscope-like images. The reconstruction algorithm is propagating the hologram in the sensor plane back to the object plane, which is applied by multiplying a Fourier transform of the hologram by a transfer function of the free space, then followed by an inverse Fourier transformation. Twin image issue exists when reconstruction is done only by intensity. The lost of the phase information gives the twin image problem. This can be fixed by recovering the phase information. The pixel size of the image sensor is a critical factor affecting the image resolution or the information from holograms. Therefore, the resolution is restricted by the pixel size. The limitation can be mitigated by using pixel super-resolution technique [86]. The basic idea of super pixel-resolution is synthesizing one high-resolution image from several low-resolution images which is recorded by shifting the illumination light source slightly. The pixel super-resolution technique can provide resolution down to < 1μm. [92]

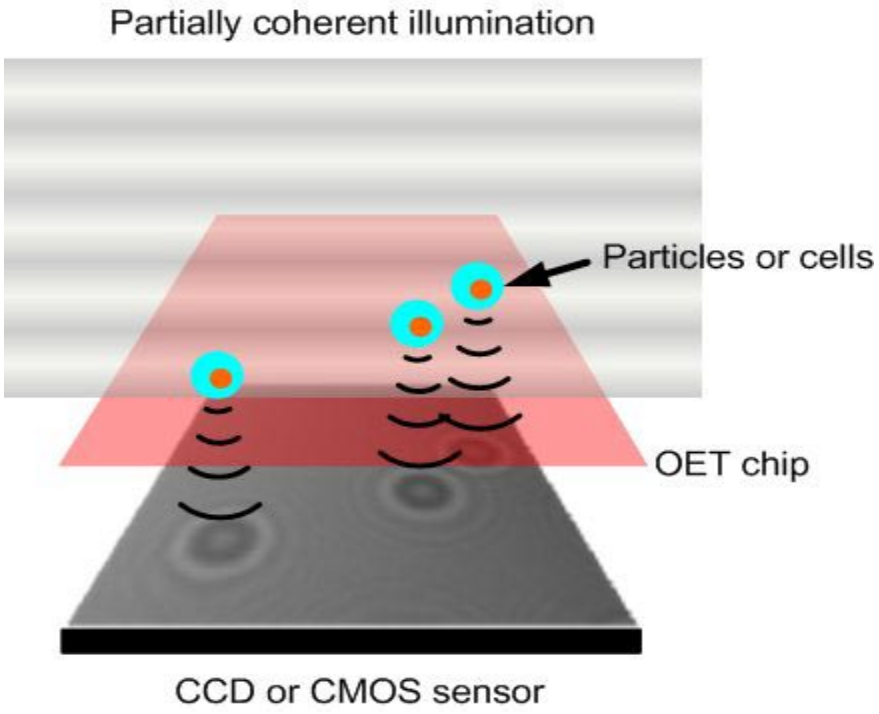

Figure 4- 1 the schematic diagram of lensfree on-chip microscopy. In this imaging scheme, inline holograms of samples are recorded using partially coherent illumination. The large field-of-view (FOV) is equal to the dimension of the CCD.

Usually, the on-chip holographic microscopy is built with two glasses sandwiching the sample solutions. In order to verify the on-chip holographic microscope which consists of OET chip, we sandwiched the particles with an OET and an ITO glass. Figure 4- 2 and Figure 4- 3 are the images showing the particles on top of an OET chip. Because of absorption spectrum of the a-Si layer on OET chip, infrared LED light source was used as the reference background light source (wavelength = 840). In the Figure 4- 2 and Figure 4- 3, raw holographic images are compared with the microscopic images to prove the concept. Figure 4- 2A shows a large-area image of high-concentration particles. The Figure 4- 2B-E are the zoom-in image of the Figure 4- 2A, which demonstrates the detail of the comparison. The empty areas where no particles

located in the holographic image are verified by microscopic image. It proves the on-chip holographic microscope can be built with an OET device.

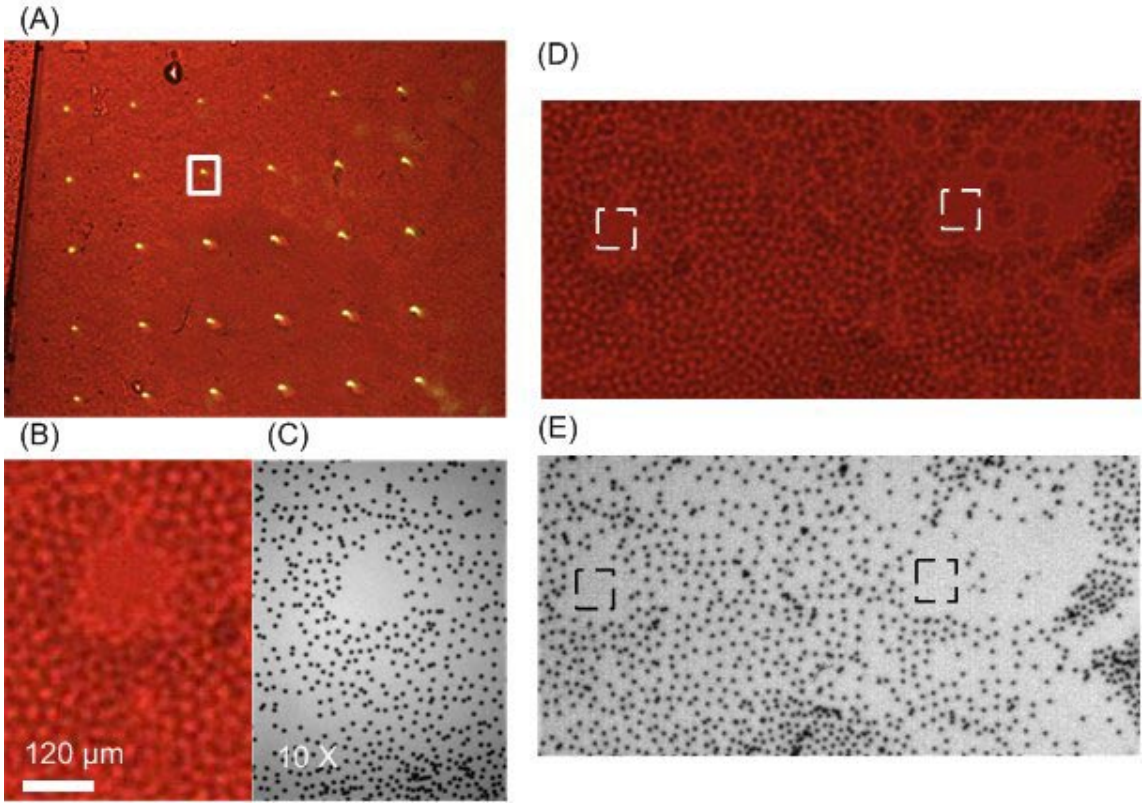

Figure 4- 2 (A) A lens-free image obtained by a partially coherent holographic on-chip imaging platform with a FOV of ~32 cm^2 (*6.55mm* × *4.92mm*). (B) The selected area of interest (corresponding to the rectangular in (A)) **shown at higher magnification. (C) The 10X image of the same area of interest in (B). (D)(E) Comparison images of the area of interest under 10X objective lens and on-chip lensfree holographic microscope.**

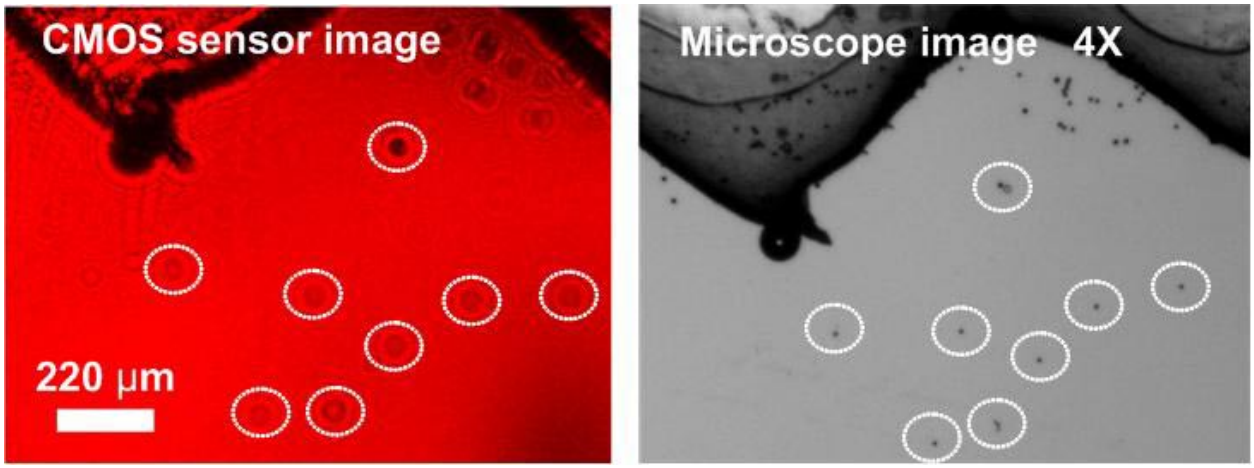

Figure 4- 3 The diffraction image of 10-µm beads can be verified by microscope image of the same region.

The Figure 4- 4 shows the typical holographic images of HeLa cells and 25 µm particles. The holograms can be used to build the image libraries for pattern-matching method (see next section). The method to build the library is to average intensity of 20 sample images in the same imaging condition.

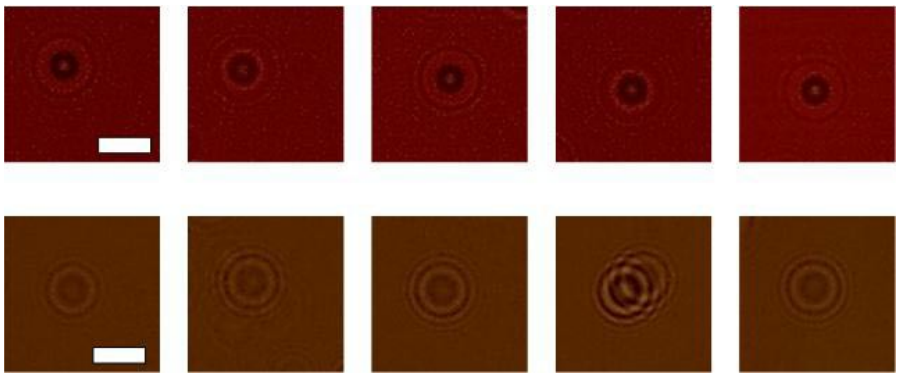

Figure 4- 4 Sample images of polystyrene particle and Hela cells. Top row: 25µm beads. Bottom row: Hela cells. Building image libraries by averaging sample images can be used to recognize unknown by patterning matching method. (see 4.4) Scale bars are 107 µm.

4.3 OET Integrated with On-Chip Lensfree Holographic Microscopy

We report an OET platform that is integrated with a lens-free holographic microscope for real-time on-chip detection and optical manipulation over a large field-of-view. Micro-objects are trapped, moved or patterned by light-induced DEP forces with the assistance of a lens-free holographic microscope. All the detection and manipulation steps are supervised by a computer with a custom-designed LabView program to form a feedback loop, which enables the lens-free-microscope-integrated OET system to keep track of individual objects and to manipulate them interactively in parallel.

Figure 4- 5 shows the schematic configuration of the OET system that is integrated with an on-chip holographic microscope. At the core of the system, the OET device is directly placed on top of an image sensor array. The OET device is composed of two rigid indium tin oxide (ITO) plate electrodes, where the bottom ITO is deposited a layer of heavily doped a-Si: H and a layer of 1-μm intrinsic a-Si:H. The liquid containing particles is sandwiched between the two flat electrodes. Since the a-Si layer allows infrared light to penetrate, an 850-nm LED coupled with a fiber-optic cable forms a partial coherent light source for the holographic imaging. The light source illuminates on the OET chip from 10 cm above. The senor array used in the chapter is a charge-couple device (CCD) image sensor (KAF-8300, Kodak) with a pixel size of 5.4 μm and an active area of 17.96 mm × 13.52 mm or a CMOS sensor (Logitech). When the scattered wave from objects interferes with the unperturbed wave from the LED light source on the surface of the image sensor, the holograms of objects are recorded by the CCD pixels. As a result of this, the manipulation chamber can be monitored by the on-chip holographic microscope without the use of any lenses. It removes the limitation of small FOV of conventional objective-based

microscopes and increases the detection area, matching it to the active area of the CCD or CMOS sensor array.

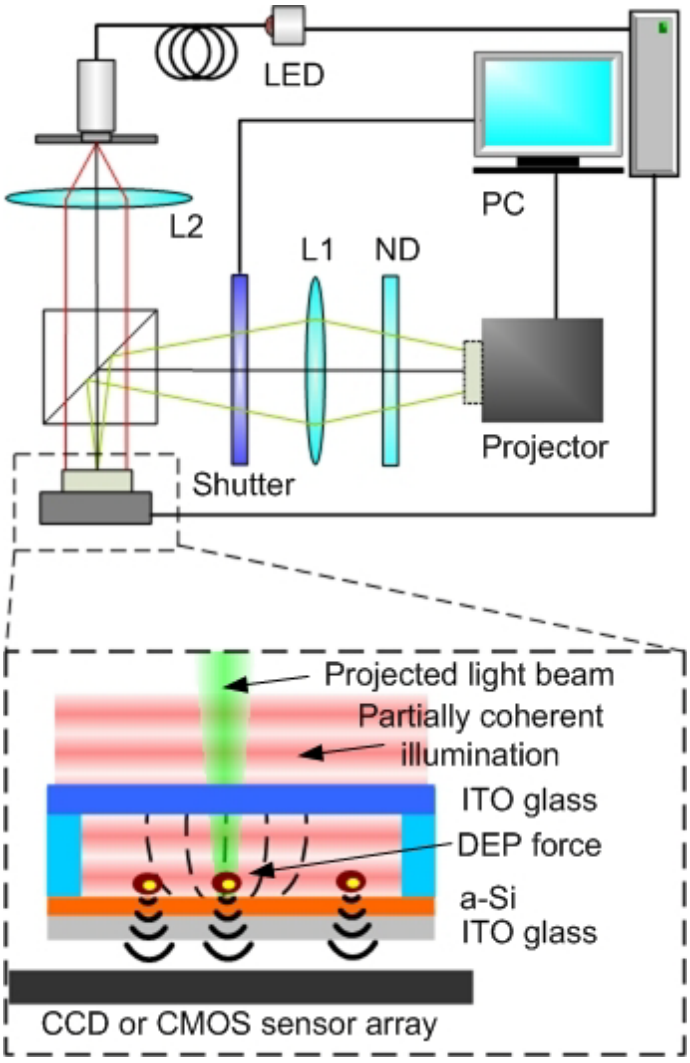

Figure 4- 5 Schematic diagram of the experimental setup and the device. The OET chip is placed on the top of an image sensor array.

For DEP manipulation, a commercial DMD-based projector is set to provide the light patterns to trigger light-induced DEP. The projection lens and color filter of the projector are removed and replaced by a lens with 15 mm focal length. The projection light beam is aligned with CCD for automated control. The top and bottom ITO glass substrates are supplied with an

alternating-current (AC) bias. Before the projection light illuminates the a-Si layer, the impedance of the a-Si is high, and therefore no DEP forces are produced. After a light beam hits the a-Si, the conductivity of the photoconductive layer decreases, which shifts the bias to the liquid layer. It induces a non-uniform electric-field near the projection light spots. In this study, polystyrene particles experience negative DEP forces, while HeLa cells experience positive DEP forces. Figure 4- 6 demonstrates an example of large scale, realtime interactive optical manipulation on a LUCAS integrated OET platform. A group of 5 closely positioned 10-μm polystyrene beads are separated into two groups by manually control the projected optical patterns using a mouse on a computer.

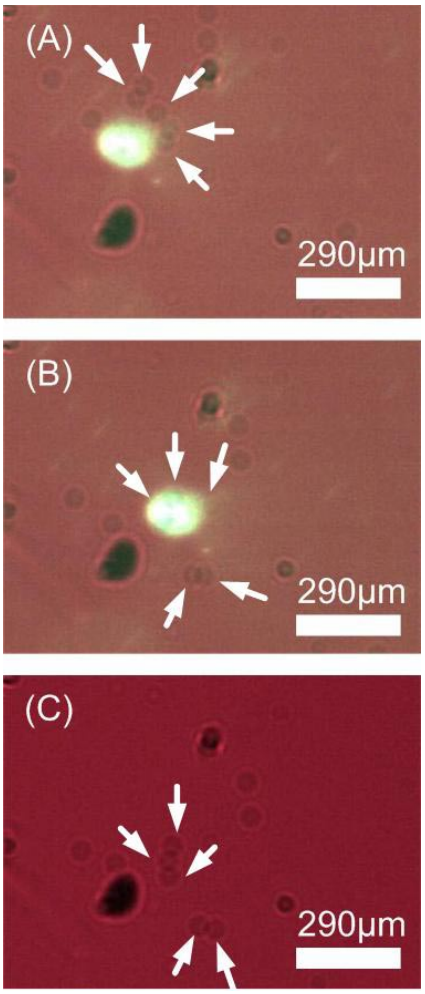

Figure 4- 6 The consecutive images showing a light spot controlled by projector to separate a group of five micro beads into two and three small groups.

4.4 Particle Recognition and Tracing Function

Large-area parallel manipulation requires continuous monitoring of every moving object in the FOV, tracing its location, and dynamically adjusting the projection light spots in real time. To accomplish the automated real-time feedback control, the monitoring and manipulation of objects are realized with a lensfree on-chip microscope and a digital projector, which are connected and synchronized via a computer. LabView (National Instrument, USA) is used to develop the automated process for real-time monitoring and manipulation (Figure 4- 7).

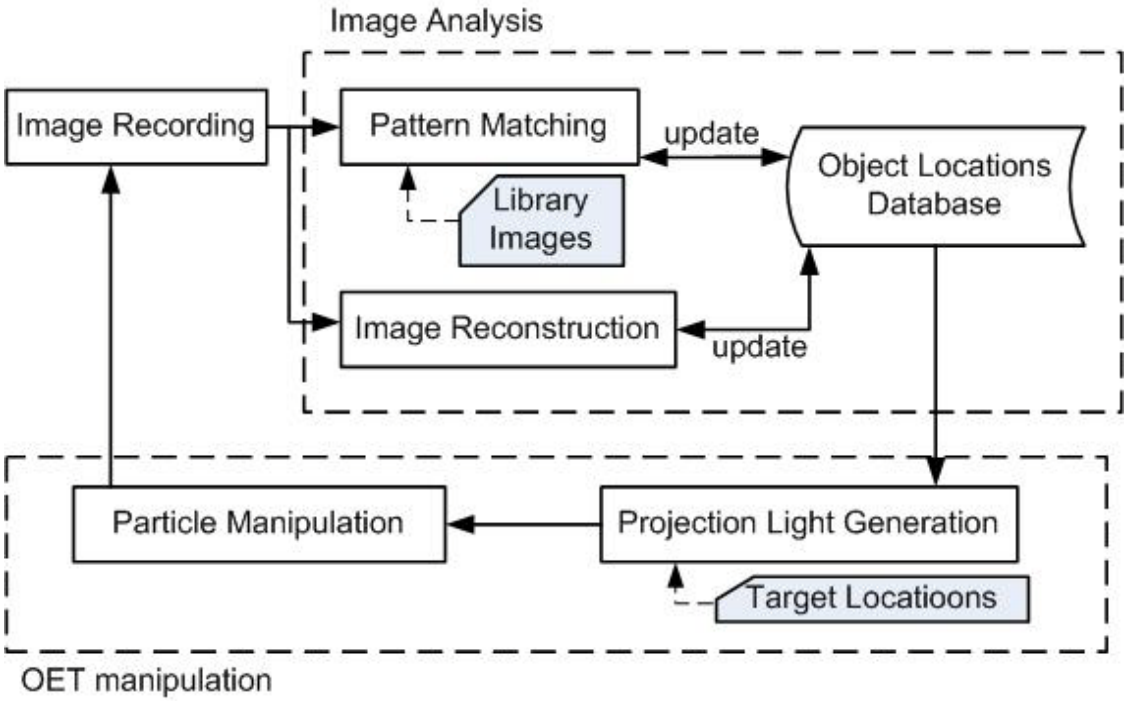

Figure 4- 7 Automated process chart of the system. The object locations database provides the information for (1) tracing the objects and (2) generating the manipulation beams. The database can be updated through two image analysis methods: pattern matching and holographic reconstruction.

For monitoring the micro-objects inside the manipulation chamber, the automated process inside the LabView program begins by capturing a holographic image from the CCD image sensor. Not to disturb the recording of holograms, a mechanical shutter is activated during the image acquisition period of the image sensor to block out the light from projector (Fig. 1). The automated process can then use two different methods to determine the positions of the micro-objects for each holographic frames: (1) A pattern-matching algorithm which compares the recorded holograms to a prepared texture library [93]; or (2) a holographic reconstruction process that generates microscopic images and reports the centroids of the detected objects [94].

Method (1) is based on the concept of correlation index which simply evaluates the similarity of a recorded hologram to a mean library image of a given object type. To build the library image for each object type, a suspension of particles (i.e. 10, 20 or 30 μm micro-particles) is injected into the OET chip and then the images of 20 arbitrarily chosen particles (recorded with the same wavelength and depth position) are averaged to generate the mean library image. With the defined object library image *L(x',y')*, a 2D deviation map (*Dev(x,y)*) can be calculated for the recorded image *f(x,y)* by:

$$Dev(x,y) = \sum_{(x',y') \in D_L} \left| \qquad \right| \qquad \textbf{Eq. 4- 2}$$

where D_L represents the domain of the library image. After this step, the 2D deviation map is converted into a 2D correlation map for each object type by using:

$$Corr(x,y) = 1 - \frac{Dev(x,y) - Dev_{MIN}}{Dev_{MAX} - Dev_{MIN}} \qquad \textbf{Eq. 4- 3}$$

where Dev_{MAX} and Dev_{MIN} refer to the maximum and minimum of the deviation values for $f(x,y)$. After the creation of this 2D correlation map, potential candidates with large correlation peak

values can be distinguished by setting a certain threshold value. The coordinates of the correlation peaks are used as the positions of the detected objects and the type of each object can be identified by finding the maximum correlation when matching with various library images. Further discussion on this detection and tracking related technique can be found in [93].

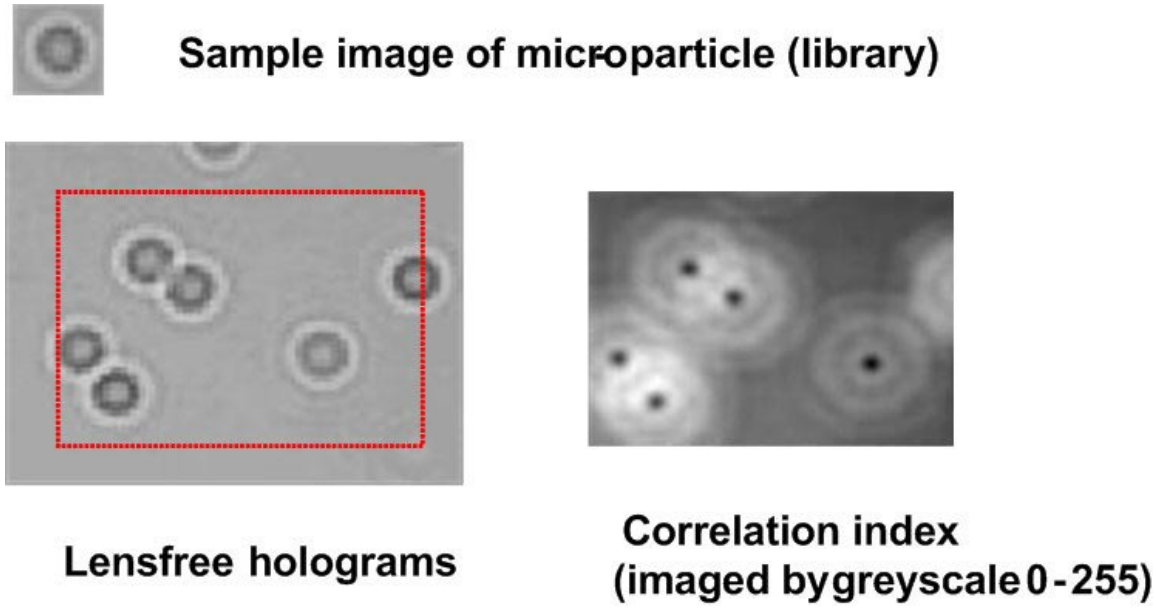

Figure 4- 8 Pattern-metching method of lensfree holographic microscope. Left: the raw image from the CMOS sensor. Right: the visualized 2D correlation map of the left image. The correlation index is from 0-255 and visualized. The black areas are the areas that the samples image can be matched in the raw image.

Different from the method discussed above, method (2) is based on in-line holography and uses a digital algorithm to convert the lensfree holograms back to the microscope-like images of micro-objects. This low-resolution reconstruction or conversion is done by propagating the recorded hologram intensity back to the plane of objects [94]. For this end, first, the complex field is decomposed by fast Fourier transform (FFT) into components with various spatial

frequencies. Then each component is multiplied with its corresponding transfer function component to simulate the effect of wave propagating in a uniform medium. Lastly, the modified frequency components are merged back into a complex field in real space through an inverse-FFT operation. Out of this low resolution reconstruction process (which still contains the twin-image artifact), method (2) provides microscope-like images of the objects (see for example Insert 2 in Figure 4- 9), whose coordinates are determined by calculating their centroids after thresholding the intensity profile of the reconstructed images. The type of detected objects can be identified by analyzing the morphological properties of their reconstructed images (e.g., size, intensity, and eccentricity). Since the images reconstructed by this method do not overlap as much as the holograms do, this approach is especially suitable for analyzing samples containing higher density of micro-objects. Further details of this holographic imaging technique can be found in [94].

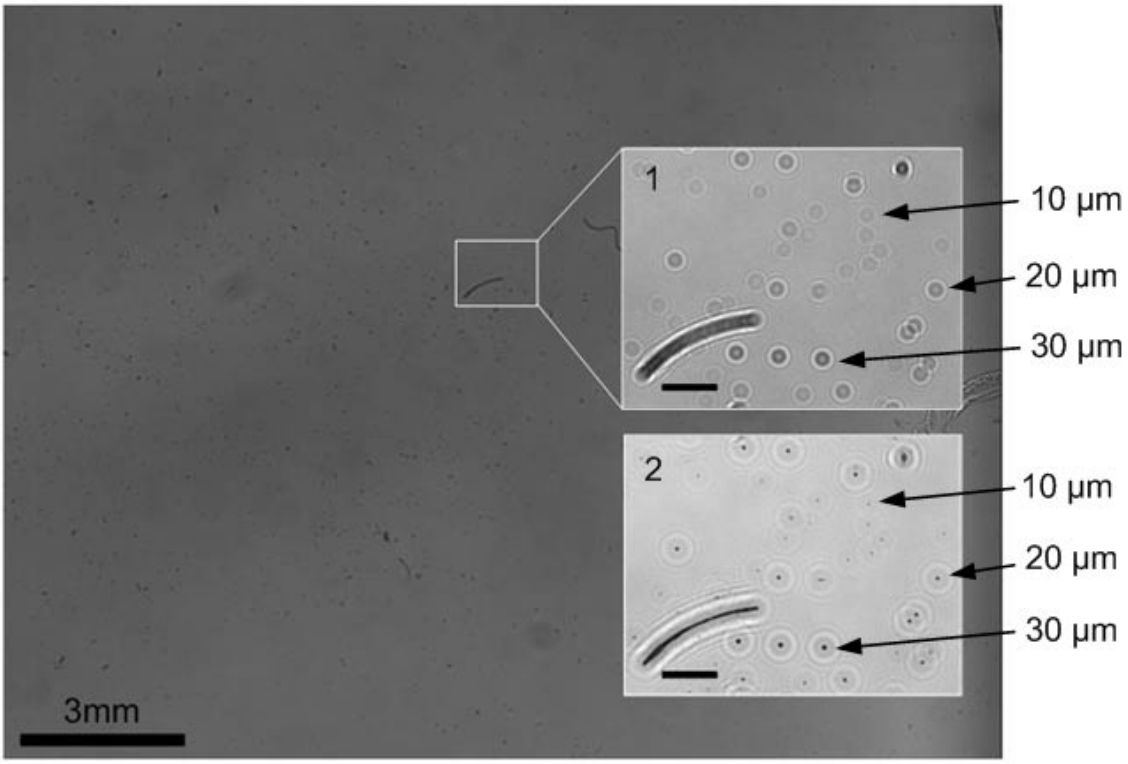

Figure 4- 9 A full field-of-view holographic image for a mixture of 10, 20, and 30 µm polystyrene beads. The insets show two different methods used to determine the locations of objects. Inset 1 (top) is the holographic image of the circled area, where holographic textures are used to identify particle types. Inset 2 (bottom) is the reconstructed microscopic image of Inset 1. The particle types are distinguished by their sizes in the reconstructed image. The scale bars in the insets are 300 µm.

To test the performance of our experimental set-up, polystyrene particles with diameters of 10, 20, and 30 µm were mixed and suspended in KCl solution. The mixture was introduced onto the platform. An example holographic image of the particle mixture with the FOV of 17.96 mm × 13.52 mm is showed in Figure 4- 9. Inset 1 in Figure 4- 9 shows a raw hologram that is cropped from the full FOV, while Inset 2 shows the intensity of its lower resolution reconstructed image. The dynamic locations and the type of the particles can be determined by our custom-designed LabView program using the holographic reconstruction process. Inset 2

shows that the 10, 20, and 30 μm particles can be clearly recognized by their sizes in the reconstructed images. This inset also demonstrates that our holographic detection process can successfully separate nearby particles even when their hologram textures are spatially overlapping with each other.

According to the object coordinates determined by either of the two methods discussed above, our custom-designed LabView program can compare the new object coordinates with the previous ones to update the object location database. With the location database, the LabView program can speed up the detection process by keeping the information. Thus, the program only searches over the whole FOV for potential candidates in the first frame. Starting from the second frame, searching is limited to the neighborhoods of the objects that are detected in the previous frame. Based on the location database and the preset final locations of the objects, the program creates a projection light pattern to induce DEP forces on target micro-objects (e.g., particles or cells) over a period of time. Target micro-objects will be moved toward the preset locations during the time when projection light illuminates. The same procedures repeat themselves after the acquisition of each holographic frame. The cycle time of the whole loop can be minimized by carefully overlapping the period for DEP manipulation and the period for image analysis.

Figure 4- 10A shows that 901 target particles are concurrently and individually detected and moved within the field of view. By using reconfigurable virtual electrodes on the a-Si layer in OET, the developed LabView program can dynamically adjust the projection light pattern based on the real-time detection results generated by the on-chip holographic imaging technique. Figure 4- 10B shows that the LabView program can follow the pre-defined manipulation strategy to create light spots tracing multiple target particles in parallel. The preset manipulation scenario in Fig. 4 was to move the recognized particles toward the direction pointed by white arrows, so

the light spots were projected at the opposite side allowing negative DEP forces to push the particles away from the light spots at which the electric field maxima were. the square light spots were shown for visual purpose. For image analysis, the projection light should not be recorded.

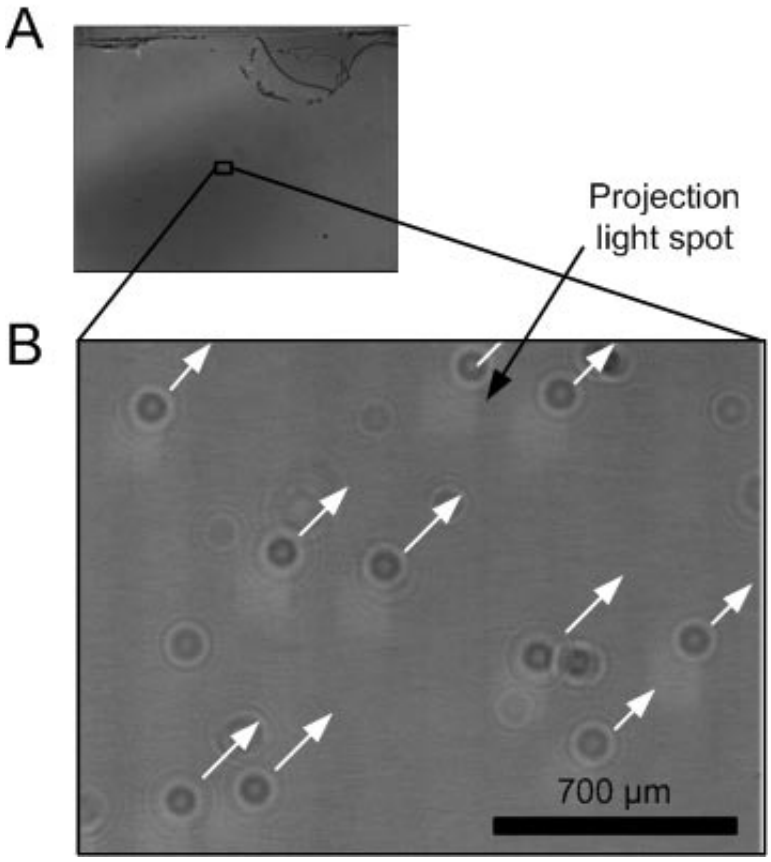

Figure 4- 10 (A) A full field-of-view image showing the parallel manipulation of 901 target particles. (B) The zoom-in image of (A). The target particles experienced negative DEP force and were repelled by the projected light spots. To speed up the detection process and minimize the cycle time of the whole system, the LabView program only searches over the whole FOV for potential candidates in the first frame. Starting from the second frame, searching is limited to the neighborhoods of the objects that are detected in the previous frame. All the detection and manipulation steps are synchronize by a custom-designed LabView program to form a feedback loop, which enables the lensfree-microscope-integrated OET system to keep track of individual objects over a large FOV and to manipulate them interactively in parallel.

4.5 Cell Manipuation and Particle Sorting

Human ovarian cancer cells (HeLa cells) were also used in this study to verify the platform's ability to manipulate live biological cells. HeLa cells was cultured in Dulbecco's modified Eagle's medium (DMEM), supplemented with 10% fetal bovine serum (Hyclone), 50 mg/ml penicillin/streptomycin, and 50 mg/ml L-Glutamine. For all of experiments, the cells were first washed with phosphate buffered saline (PBS, pH7.4) and then were dissociated using 1X trypsin. After washed and neutralized with PBS, cells were re-suspended into isotonic buffer (8.5% sucrose [wt/vol], 0.3% dextrose [wt/vol]). The conductivity of the cell suspension was adjusted to 100 - 200 μS cm^{-1} by this isotonic buffer. The cell suspension was injected into the OET chip and placed on the system for characterization. For determining the locations of HeLa cells and distinguishing them from other micro-objects in the chamber, the holographic textures of potential candidates were matched to a mean library cell image (Method (1) – see the Methods section), which was composed of microscope-verified cell holograms.

Figure 4- 11 shows the sequential holographic images of a single HeLa cell which was being dragged toward a desired location during real-time feedback manipulation. Unlike polystyrene beads used for initial testing, the HeLa cells experienced positive DEP force, so the cell hologram followed the projection light spot. The LabView program kept on updating the location of the cell to determine the position of the new projection spot. Therefore, the cell closely followed the designed path (defined by the light spot) toward the target destination.

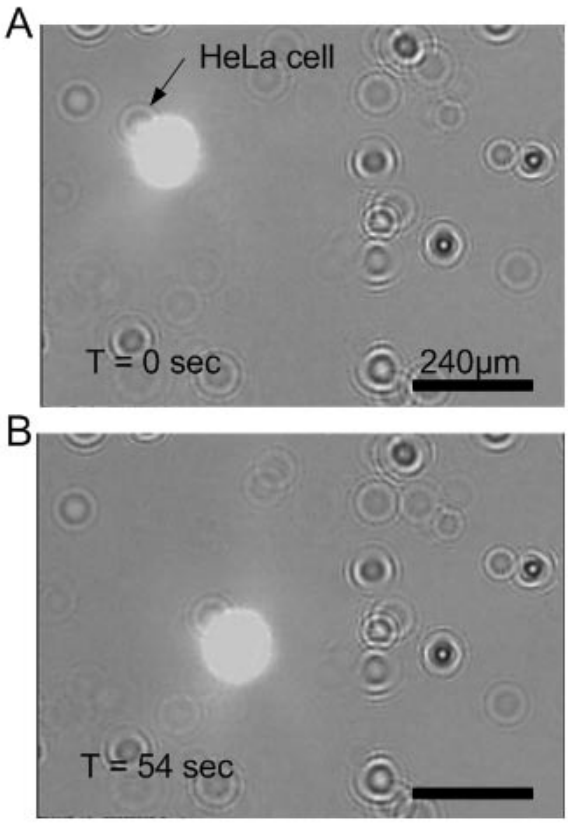

Figure 4- 11 Sequential holographic images of a single HeLa cell attracted by a projected light spot and dragged toward the desired location.

When the preset manipulation scenario is more complicated, the developed program can dynamically adjust the projection light pattern based on the real-time detection results to reconfigure virtual electrodes on the a-Si layer. Figure 4- 12 is the sequential holographic images showing selected particles were arranged to form an elliptical pattern. The preset final locations were along the ellipse in Figure 4- 12 and the particles selected by pattern-matching method were first distributed in the FOV. After 122 sec, most of the selected particles were moved to its final position with an average moving speed of ~25 um/sec, which demonstrates that the particles can be traced dynamically and in parallel by the system. In this platform, the average moving speed of a certain particle can be affected by the intensity of projection lights, the period

of projection in each cycle, the setting distance between projection light spot and the centroid of holograms, etc. Longer moving distance in each monitoring cycle increases the risk of losing the information about particles. The lost of information results in the failure of tracing function. However, the system can be optimized by adjusting the parameters.

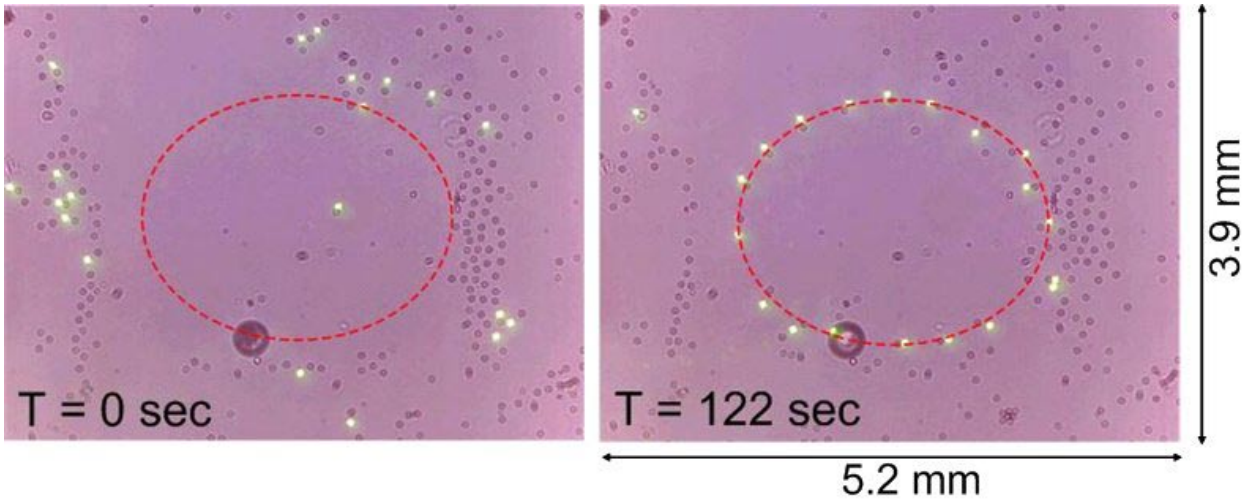

Figure 4- 12 The feedback-control function allows LUCAS OET to select particles and manipulates them to the target locations automatically. The top figure shows the system picked up the particles after pattern matching recognition. The bottom figure shows after 122sec the selected particles were arranged to an elliptical pattern. The average moving speed is about 25 um/sec.

Manipulation with the advice of reconstructed images is shown in Figure 4- 13. Different particles (10 and 30 μm) were mixed in KCl solution and injected into the device. The manipulation scenario was to pick up the minor type of particle and move them away from the majority. In the experiment, the method 2 was employed to recognize different particles. The 30-μm particles were indentified form the others in the reconstructed images, marked with red cycles by the LabView program, and moved to the target locations which are marked by “x” (see Figure 4- 13). The system was built with the ability to reconstruct every holographic image

during the manipulation as well as the first frame. Therefore, the recorded images in Figure 4- 13 were reconstructed ones instead of the raw holographic images. Considering the computation power of the computer, low-resolution reconstruction with twin-image artefact was used to balance the period of time for real-time manipulation and real-time detection in the full FOV of 17.96 mm × 13.52 mm. This experiment demonstrates the capability of the lens-free-microscope-integrated OET to trace objects with real-time reconstructed images and also to separate minor objects from the mixture.

4.6 Conclusions

A wide-field optoelectronic tweezer (OET) platform that is integrated with a lensfree holographic microscope is reported. The holographic on-chip microscope furnishes OET with a complementary detection function to enable large-area, programmable, parallel light-induced DEP manipulation of microscopic particles or cells with real-time position feedback. The manipulation area (i.e., the FOV) has been increased to 240 mm^2, more than 2 orders of magnitude larger than conventional microscope based OET platforms. Methods of automated pattern matching and image reconstruction have been demonstrated for monitoring thousands of objects inside the FOV. Real-time closed-loop manipulation of polystyrene particles and human ovarian cells has been achieved with this holographic on-chip microscope-furnished OET system.

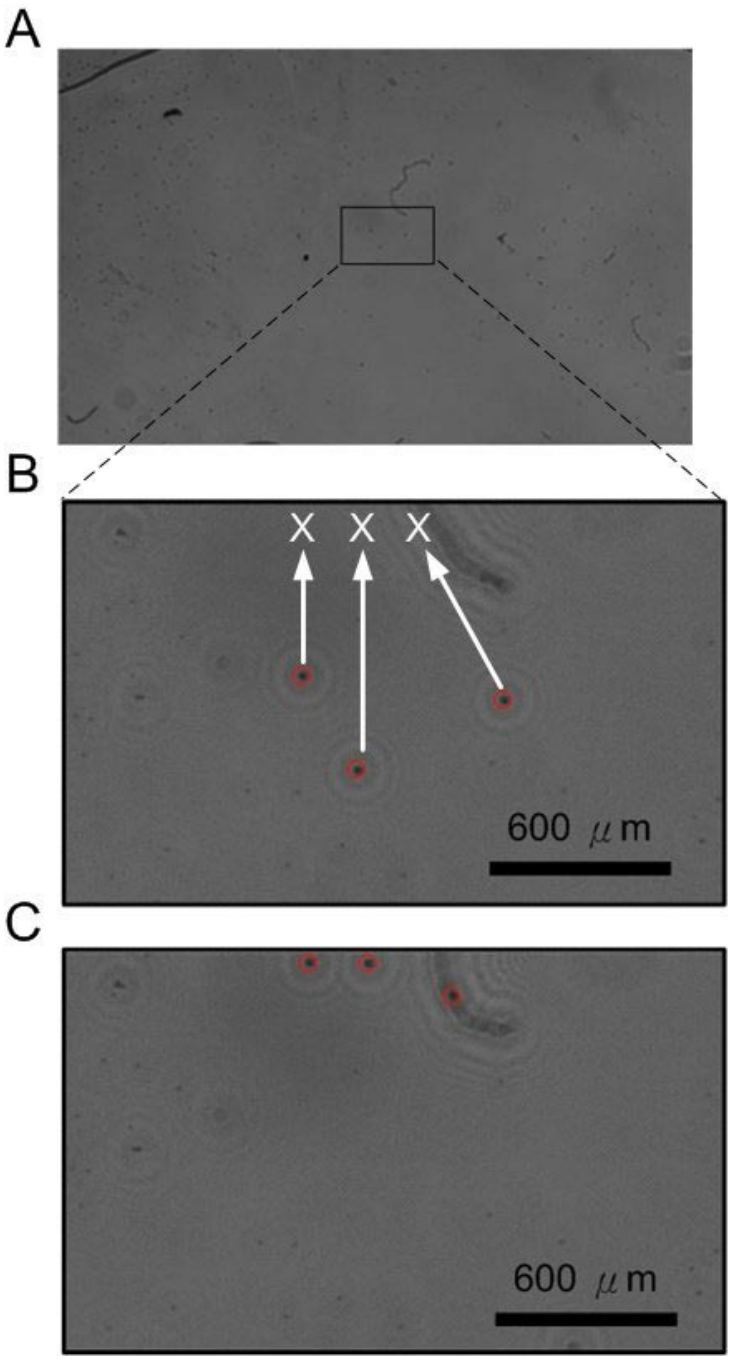

Figure 4- 13 Sorting of particles. (A) A full field-of-view reconstruction image for a mixture of 10 and 30 μm polystyrene beads. (B) and (C) are sequential reconstruction images of the area of interest shown in (A). Three 30-μm particles are recognized and circled by the LabView program in (B). The three particles are moved to the target locations which have been set.

Chapter 5 Single-cell Applications

5.1 Introduction

Single-cell analysis is an important trend in future biomedical diagnostics, cloning, and cell biology research. The understanding of the heterogeneity at cell level has become an approach to study complex phenomena such as cancer, development, microbial ecology, and noise in biological systems[95-99]. Technologies such as polymerase chain reaction (PCR), microarrays or sequencing have successfully been applied to samples containing many thousands of cells. Collecting useful information about the underlying biochemistry of specific cells usually requires isolating small number of cells from background population or mixture. The capability of sorting and isolating single cells is critical for those analyses. It is not only a way to collect useful information about the underlying biochemistry of specific cells from background population but also a start of a desired population. Many techniques exist to sort cells from a population. The most widely used and well-established method refers to fluorescence-activated cell sorters (FACS). Conventional FACS based on collecting fluorescence from makers provides a high-speed viable cell sorting tool. Most FACS encapsulating and sorting cells in drops labeled with electric charges still suffer from sorting rare cells from samples with small volumes or a small population. Laser capture microdissection (LCM) [100, 101] offers a precise system for picking up cells from fixed tissues and transferred to specific films , but usually applied to fixed cells. The development of microfluidic, lab-on-a-chip (LOC) technologies for single-cell sorting respond to the demand on complementary methodologies [102]. Microfluidic or Lab-on-a-chip devices have enabled the ability to analyze the heterogeneity with single-cell resolution. Microfluidic devices handling liquid volume as small as nantoliter level has emerged as a

promising tool for processing single-cell analysis [103-108]. The cell-based microfluidic chips become increasingly implemented mainly because of PDMS, which is easily fabricated by soft lithography and relatively cheaper than Si-based or glass-based devices. Utilizing deformable mechanical micro-valves and pumps made by PDMS, microfluidic devices enable minimization of sample consumption to perform more sensitive and efficient biochemical reactions as well as isolation of single cells from small volume of biological specimens [105, 109]. This can minimize the errors occurring during the sample dilution or operations, reduce the material loss, and increase the accuracy. Even though microfluidic devices are effective in controlling the delivery of fluid, the inefficiency to manipulate particles or cells carried by the fluid is still the barrier for many applications. It is difficult for PDMS microfluidic chips to do some special application, such as electrical forces for microscale cell manipulation [109]. There are still some methods to handle, place, or transport cells in PDMS microfluidic chips. In valve-based devices, manipulating single cells by controlling fluid requires complicated networks of fluidic control valves, which means a complex chip design. The difficulty in designing and operating such complex devices has discouraged many biologists and clinicians from using microfluidic devices. For handling cells, the ideal method should have the properties of parallel formats, have high throughput capability, and limit dilution. Many techniques exist to physically manipulate cells in microsystems, including electrical[24], magnetic, acoustic[76], optical forces[110, 111], hydrodynamic flow and focusing , the use of on-chip valves to direct cell transport, and the use of pressure and geometrical trapping of cells [30].

In contrast, optoelectronic tweezers (OET), mainly relying on light-induced DEP forces, is a useful and user-friendly platform to directly manipulate cells, instead of the fluid, in a non-contact method [1, 112, 113]. Compared to other manipulation methods such as electrical [114],

magnetic [115], optical [110] , or acoustic forces [116], OET has the flexibility and dynamic control of optical trapping to individually address single cells from one location to another with precision. Low light intensity prevents OET from damaging cells, and massively parallel manipulation of specific object such as semiconductor microdisks, nanowires, DNA molecules, and mammalian cells [2, 11, 15, 78, 80, 81] has also been reported. Moreover, the potential of OET for integration with PDMS channels has been demonstrated by using embedded single-wall carbon nanotubes (SWNT) electrodes [117]. The properties combining optical manipulation and electrical forces make OET a strong complement to microfluidic devices. Optical forces such as optical tweezers or optical tweezers arrays allow directly forces via laser light beams to manipulate single or multiple cells to target locations. Without any additional electrodes, objects can be trapped by focused laser lights and be moved to desired locations. Optical tweezers provide a tool to dynamic control objects but high numerical aperture and high optical intensity requirement lead to small imaging field and potential damages. Electrical forces mainly relying on dielectrophoresis (DEP) are increasingly common method for microfluidic platform because DEP utilizes the intrinsic electric polarizability of cells, easy fabrication of electrodes on Silicon or glass substrate and easy electric control. However, most of the devices with electrical manipulation need fixed metal electrodes, which makes them difficult to individually manipulate single cells and isolate target cells from a population. Hybrid integrated circuit (IC) devices have been shown to individually control cells by two-dimensional array of electrodes [118], but these high-cost chips do not suit the integration with deposable microfluidics (i.e., PDMS) for biological applications.

OET allows for reconfigurable virtual electrodes to dynamically grab single or multiple objects to certain locations with low light intensity (~1w cm^{-1}). Compared to traditional DEP

forces created by fixed metal electrodes, OET retains the flexibility and dynamic control of optical trapping. This property makes OET a powerful and easily-used tool to trap, concentrate, separate, and pattern specific objects of interest. Although it is very attractive that conventional OET allows individual particle manipulation, conventional OET which is comprised by two rigid electrodes (a photosensitive electrode and a transparent indium tin oxide electrode) to sandwich liquid containing the particles has been limited to the specific single-cell applications and assessments [11, 81]. Single-cell applications of OET technologies have been shown recently. For example, parallel single-cell electroporation has been performed on OET platform [81]. Most of the single-cell studies need not only individual cell control but also isolating them into discrete environments for performing complex protocols. Recently, modified OET platforms have been developed to control cells in droplet microfluidics [72, 119]. The droplets are good reaction surroundings for cell application, but the OET platforms for cutting droplets are not accurate. Discreting the liquid is still very challenging for standard OET due to the insufficient fluid control of traditional OET. By using the SWNT electrodes in PDMS-based microfluidic channels or the 3D-PDMS fabrication technique, this problem of integration with other components such as fluidic channels has been addressed. how to incorporate OET into microfluidic devices for single-cell analysis still remains unanswered.

This chapter describes the microfluidic integrated OET that enables optical cell control in PDMS-based channels to accomplish multi-steps from on-chip cell selection, cell isolation, liquid plug formation, liquid plug transportation, and extraction for external single cell analysis. This chapter will provide the real benefits and practical applications of OET platforms. Therefore, OET provides not only individual cell control but also isolating them into discrete environments for performing complex protocols.

5.2 OET with SWNT Electrodes for Off-chip Single-cell Analysis

This section presents the first microfluidic integrated OET that utilizes SWNT embedded PDMS thin film as the electrode and multilayer PDMS channels to provide the valve functions for fluid control. OET and microfluidic integration structures promise a powerful platform in both fluid and cell control. The microfluidic integrated OET platform is capable of accomplishing multistep from on-chip cell selection, cell isolation, liquid plug formation, liquid plug transportation, and extraction for external single cell analysis such as single cell mRNA analysis.

The schematics of an OET integrated microfluidic platform and the procedure of preparing single cell samples are shown in Figure 5- 1A. The platform consists of an OET surface and multilayer PDMS channels. The multilayer PDMS have two layers of channels. The bottom fluidic layer includes a main channel and several branch channels with SWNT top electrodes. The main channel is used to introduce aqueous solutions with biological cells into the device. Several branch lines go from the main channel and are all connected to its own outlet. Above the fluidic layer, a control layer is used to control the membrane valve formed at the region where the top and bottom channel intersect. Figure 5- 1B and Figure 5- 1C show cross-sectional schematics of a branch channels (the A-A' line in Figure 5- 1A). If a pneumatic pressure is applied in the top channels, the elastic PDMS membrane will deform as a mechanical valve to close the bottom channel and stop the fluid flow (Figure 5- 1B). When the pneumatic pressure is released, the mechanical valve is open and the liquid passes (Figure 5- 1C). In the bottom channels, OET functions in the region where SWNT thin film is embedded into the top surface. The SWNT networks form the uniform transparent conductive electrodes on the top channel wall while an ITO glass substrate with a photoconductive layer forms the bottom channel wall. After the top SWNT and bottom ITO glasses are supplied with an alternating-current (AC) voltage, the

impedance of the bottom photoconductive layer can be decreased by illuminating light. These lower impedance regions created by light illumination works as virtual electrodes on the bottom of the fluidic channels. Hence, the applied voltage will drop across the liquid layer and induce a non-uniform electric field distribution between the top SWNT electrode and bottom OET substrates. The cells are then experienced with a DEP force and can be manipulated by changing the optical image (Figure 5- 1B).

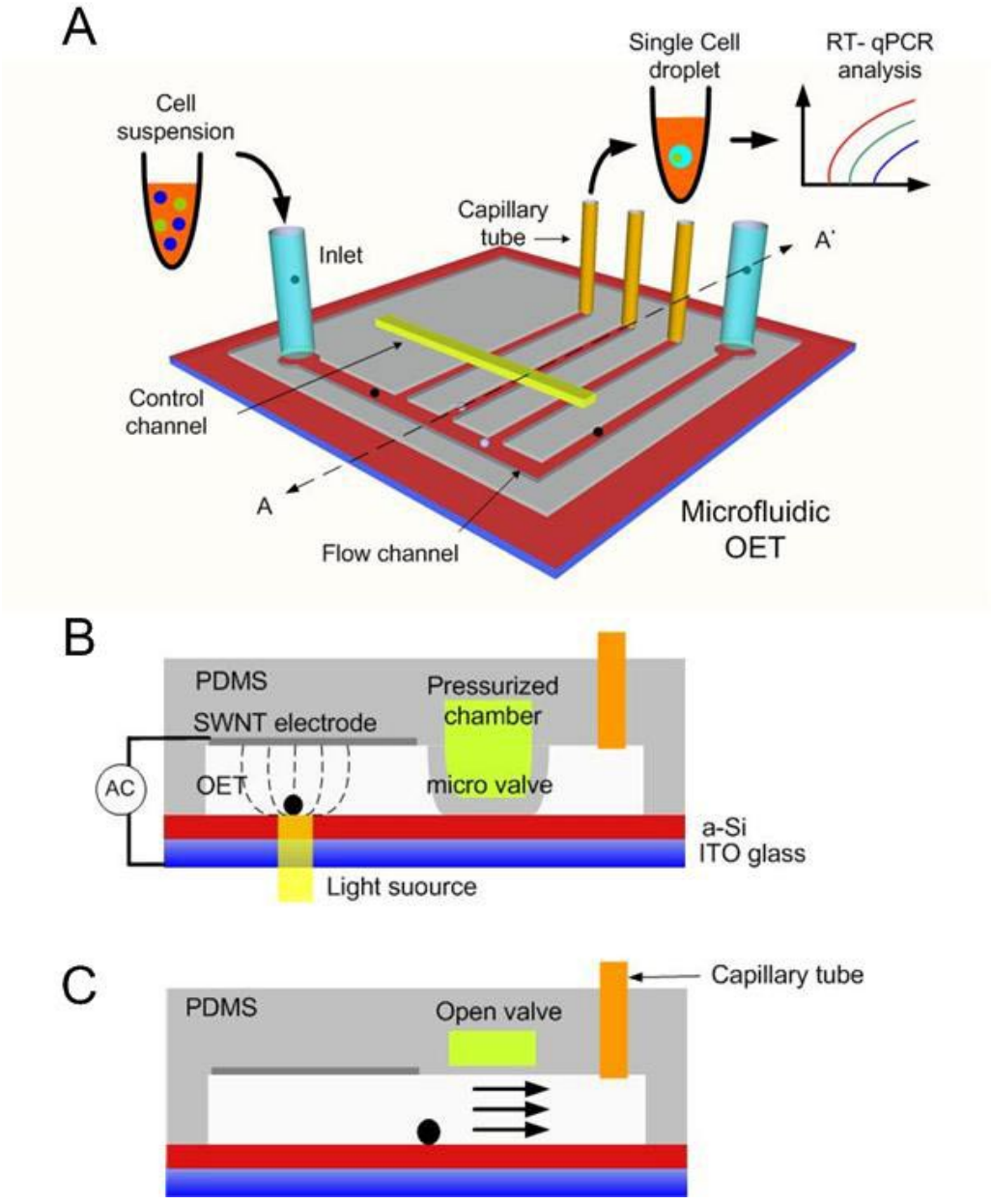

Figure 5- 1. (A) Schematic of the microfluidic integrated OET platform and the procedure of preparing single cell samples for analysis by this platform. (B, C) The side view of the A-A' cross section. The SWNT electrode enables OET integration with multilayer PDMS based microfluididics. Cell manipulation in OET is achieved by light induced DEP forces on a photoconductive surface. The elastomeric PDMS membrane valve controls fluid flows on the chip.

Figure 5- 2 shows the operation processes of preparing single-cell sample. First, cell mixture is injected into the main channel. The valves are closed to keep cells from the branch channels. Cell mixture in the OET manipulation region are selected under a microscope based on their optical signatures. Target cells then transported by light beams into neighboring perpendicular channels that are temporarily blocked by pneumatic valves that are all controlled by a single pressure source (Figure 5- 2B). After all single or targeted number of cells are transported (Figure 5- 2C), the main channel is pressurized by airflow to remove the fluid in the main channel and leave an array of isolated nanoliter liquid plugs with cells. The pneumatic valves are then opened to allow the airflow further pushing these liquid plugs across the valves to the outlets (Figure 5- 2C, D). These liquid plugs are then extracted out from the chip by capillary fused-silica tubing (1570, Upchurch Scientific). The nano-liter droplets with target cells were transferred into a standard PCR tube containing mineral oil (Sigma-Aldrich) to perform quanitive reverse transcription polymerase chain reaction (RT-qPCR) for single and multiple cells mRNA analysis.

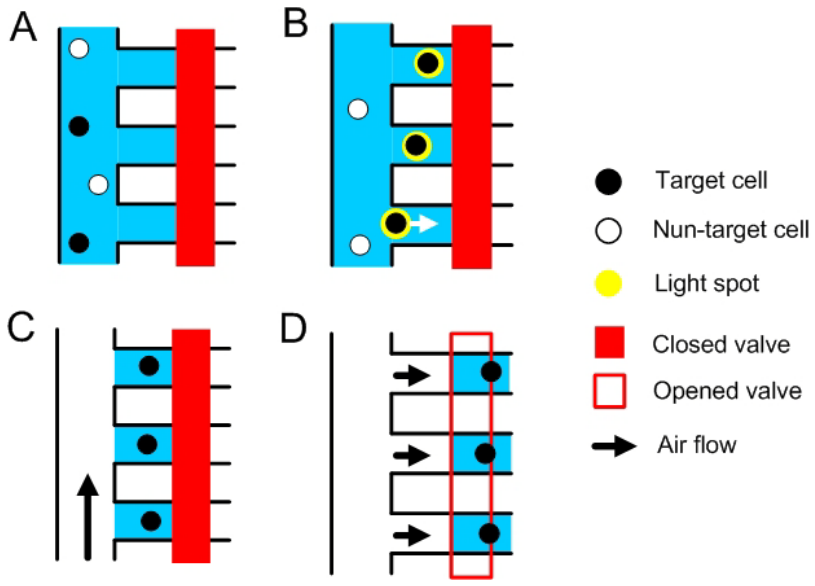

Figure 5- 2. Operation procedure of the platform (A) Cell mixture is injected into the main channel. The valves are closed to keep cells from the adjacent channels. (B) Target cell stained with fluorescent dyes are identified and selectively transported into adjacent channels by light beams. (C) The main channel is flushed by airflow to form liquid plugs in the adjacent channels. (D) The pneumatic valve is then open for pushing liquid plugs to outlets for extraction.

Device Fabrication and Preparation

To realize such integration, there are several requirements for the top electrode in PDMS channels [117]. First, the electrode needs to be optically transparent to allow optical imaging and diagnostics, since the amorphous silicon used in OET strongly absorb visible lights. Fluorescence excitation and observation has to come from the transparent electrode side. Second, the electrode needs to be electrically conductive after deposited on the elastic PDMS surface. Third, the PDMS device needs to provide an interface after electrode coating that can form strong bonding with the OET surface to provide good sealing and prevent liquid leakage during manipulation. In order to satisfy the above requirements, standard multilayer soft lithography

techniques were modified to embed SWNT thin film on PDMS microfluidic channels to form the transparent and conductive electrodes.

The fabrication process is briefly described in Figure 5- 3. Two SU-8 plymer structure were fabricated on silicon wafer and used as the master molds to cast PDMS transfer molds and top control channels. The transfer mold was made by PDMS (Sylgard 184, Dow Corning) with a ratio of 10 base: 1 curing agent. This PDMS transfer mold with channel patterns was used as a stamp to transfer the SWNT thin film from the filtration membrane to the top surface of channels. After the transfer mold was treated by trichloro(1H, 1H, 2H, 2H-perfluorooctyl)silane (Sigam-Aldrich, Inc.), it was then pressed in contact with the SWNT network on the AAO filter paper (Anodisc 47, Whatman Inc.). The high purity SWNT network on the AAO filter paper was formed by being suspended in sodium dodecyl sulfate (SDS), ultrasonically agitated, and filtered through a porous anodic aluminum oxide (AAO) filter. Uncured PDMS precursor at a ratio of 20 base: 1 curing agent was spin-coated on the transfer mold to form the layer for fluidic channels. The top control layer made with the ratio of 5 base: 1 curing agent is aligned onto the thin fluidic layer. Both layers were left at oven for curing bonding. The cured PDMS with a top control channel and bottom flow channel was peeled off from the transfer mold.

To fabricate OET substrates, a 50-nm n+ hydrogenated amorphous silicon (a-Si:H), a 1-μm undoped a-Si:H, and a 10-nm silicon dioxide are deposited on an ITO glass using a plasma-enhanced chemical vapor deposition (PECVD) process. The undoped a-Si:H serves as the photoconductive layer while the n+ undoped a-Si:H is used to reduce contact resistance. The silicon dioxide provides the permanent bonding with multilayer PDMS channels. Finally, the multilayer PDMS channels with an embedded SWNT thin film electrode on the top surface of bottom channels was then bonded with an OET device through oxygen plasma treatment. Prior

to all experiments, the channel wall was treated by flowing 1% CYTOP (Asahi Glass Co., Ltd.) followed by an air drying. Right before each experiment, a solution of 0.1% BSA was flowed for 1hour followed by a DEP isotonic buffer wash in order to prevent cell adhesion to the device walls.

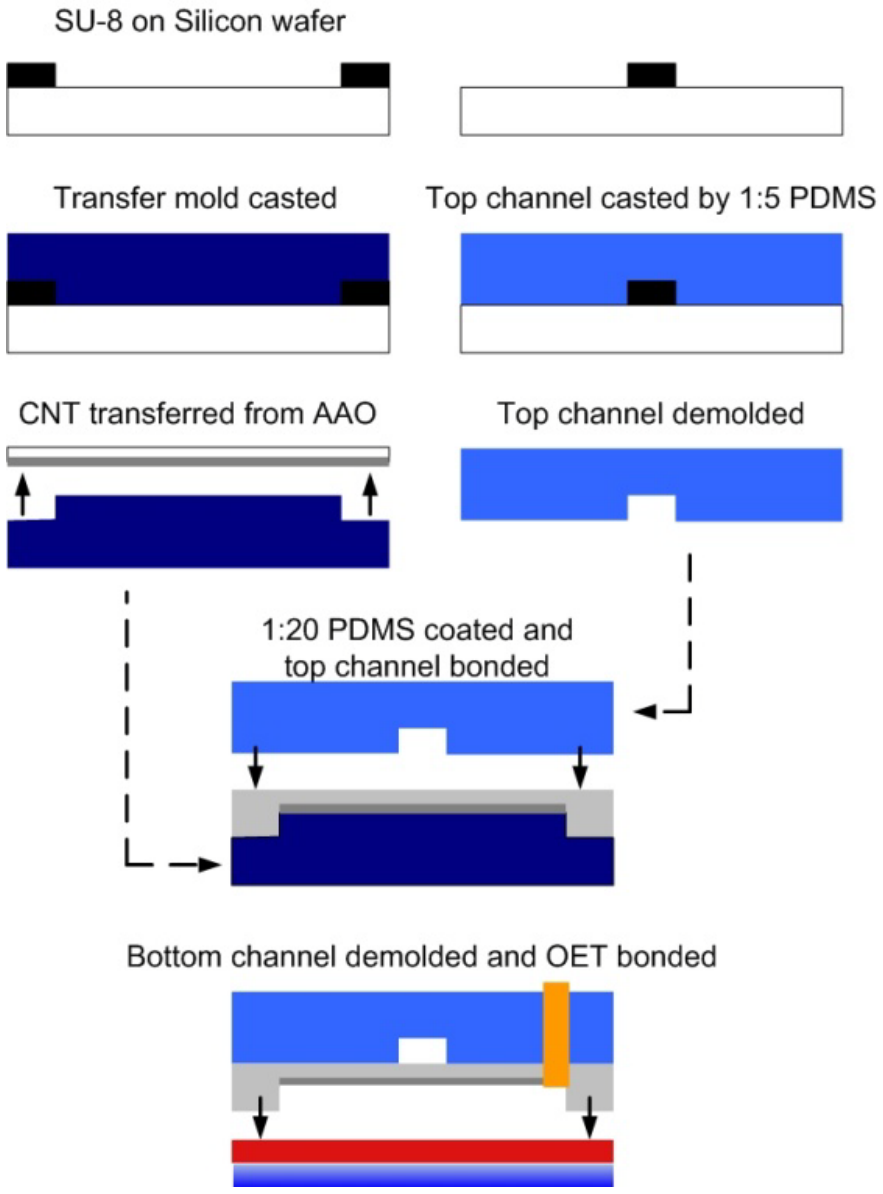

Figure 5- 3 Key processing steps for fabricating Microfluidic OET platform.

Experimental setup

In the experimental setup, the microfluidic integrated OET device was positioned on an upright microscope (Zeiss, Axioskop 2FS) equipped with a CCD camera for observation and image recording. The microscope is used to observe cells via SWNT electrodes. A mercury lamp and a filter set are also equipped for fluorescent images. In order to manipulate cells, a 633-nm HeNe laser (Thorlabs) coupled with polarizer to attenuate the intensity or a commercial DMD projector (MP730, Benq) is placed under the microscope and focused onto the photoconductive layer through an objective lens. An ac bias is applied to the SWNT electrode and the ITO electrode on the OET device with a function generator (33220A, Agilent Technologies). The pneumatic valves were connected to an external pressure source of 35 psi. The cell suspensions were also injected with a constant pressure source of 1 psi and could be switched by an external valve (V-101D, Upchurch Scientific).

Cell preparation

To verify the microfluidic OET, human ovarian cancer cells (HeLa cells) were used in this study. HeLA cells was cultured in Dulbecco's modified Eagle's medium (DMEM), supplemented with 10% fetal bovine serum (Thermo Scientific), 50 mg/ml penicllin/streptomycin (Mediatech, Inc.), and 50 mg/ml L-Glutamine (Thermo Scientific). For fluorescence sorting experiments, we stained a small population of HeLa cell with Calcein AM (Life Technologies). For experiments, we mixed this stained population with an unstained population. All of the cells were first washed with phosphate buffered saline (PBS, pH7.4, Mediatech Inc.) and then were dissociated using 1X trypsin (Thermo Scientific). After washed and neutralized with PBS, cells were resuspended into isotonic solution (8.5% sucrose [wt/vol], 0.3% dextrose [wt/vol]). The conductivity of the cell suspension was adjusted to 100 - 200 μS cm−1 by adding the isotonic buffer. Ramos cells were

cultured in RPMI 1640 medium (Mediatech, Inc.), supplemented with 10% fetal bovine serum, 50 mg/ml penicllin/streptomycin, and 50 mg/ml L-Glutamine. Before experiments, Ramos cells were washed with PBS and resuspended into isotonic solution

PCR reagents and protocol

All qPCR was performed with a commercial machine (Lightcycler 480, Roche Applied Science) and PCR kit (RNA Master Hydrolysis Probes, Roche Applied Science). Taqman primers and probe for beta-actin were designed and synthesized by Roche Applied Science (Realtime ready catalog assay ID 104288). The oligonucleotides sequences were ACCCAGCACAATGAAGATCA (forward) and ATCTGCTGGAAGGTGGACAG (reverse). For micro-liter reactions, 1-uL single-cell droplets were directly merged with 9-μL reagents mixture and then subjected to RT-qPCR. For nano-liter reactions, 30-nL cell droplets were merged with 500nL reagents by centrifugation for RT reactions. Upon completion of the RT reaction, 9.5μL PCR reagents mixture was added for qPCR. The thermal cycling protocol was as follows: 180 sec reverse transcription at 63°C, 30 sec pre-denaturaion at 95°C, following by 45 cycles of denaturaion at 95°C (15 sec), annealing 60°C (45sec) and elongation at 72°C (1sec). The standard curve was generated with known amount of human reference cDNA (Clontech) for the detection of the amount of the target cDNA.

Results and Discussions

Figure 5- 4A shows a fabricated microfluidic integrated OET device. The fluid channels are marked out with write lines while the control channel is in the dashed line. The embedded SWNT electrodes provide a conductive and transparent layer in the PDMS channels. It can be

observed that the SWNT electrode exists on the top surface of the fluid channels and the covalent bonding between the PDMS structure and the silicon dioxide surface of OET device is promised. To verify the performance of OET manipulation using SWNT electrodes, cells were first suspended in an isotonic solution, and then flowed into the microchannels. Figure 5- 4B and Figure 5- 4C demonstrate the bright field images of a cell underneath an SWNT electrode. The cell was trapped and the transported by light-induced pDEP. The optical transparency and electrical conductivity of SWNT electrodes are highly dependent on the thickness of carbon nanotube film. The electrodes with sheet resistance from 350 to 550 ohm/square have from 55 to 80% optical transparency at 632 nm. The performance of microfluidic OET device was further characterized by using Ramos cells. The manipulation speeds of Ramos cells are shown in Figure 5- 4D. The speed measurement was taken by installing a motorized XY stage (Märzhäuser Wetzlar GmbH & Co. KG) with the controller (Zeiss SMC 2009) under the microscope. In these experiments, moving speeds of the XY stage was programmed and controlled by a computer. The optical intensity and the applied frequency were fixed (300 kHz), while the applied voltages were varied from 6 to 10 V. The average speed of Ramos cells at $10V_{pp}$ is >10μm/sec and the standard variation is ~1μm/sec.

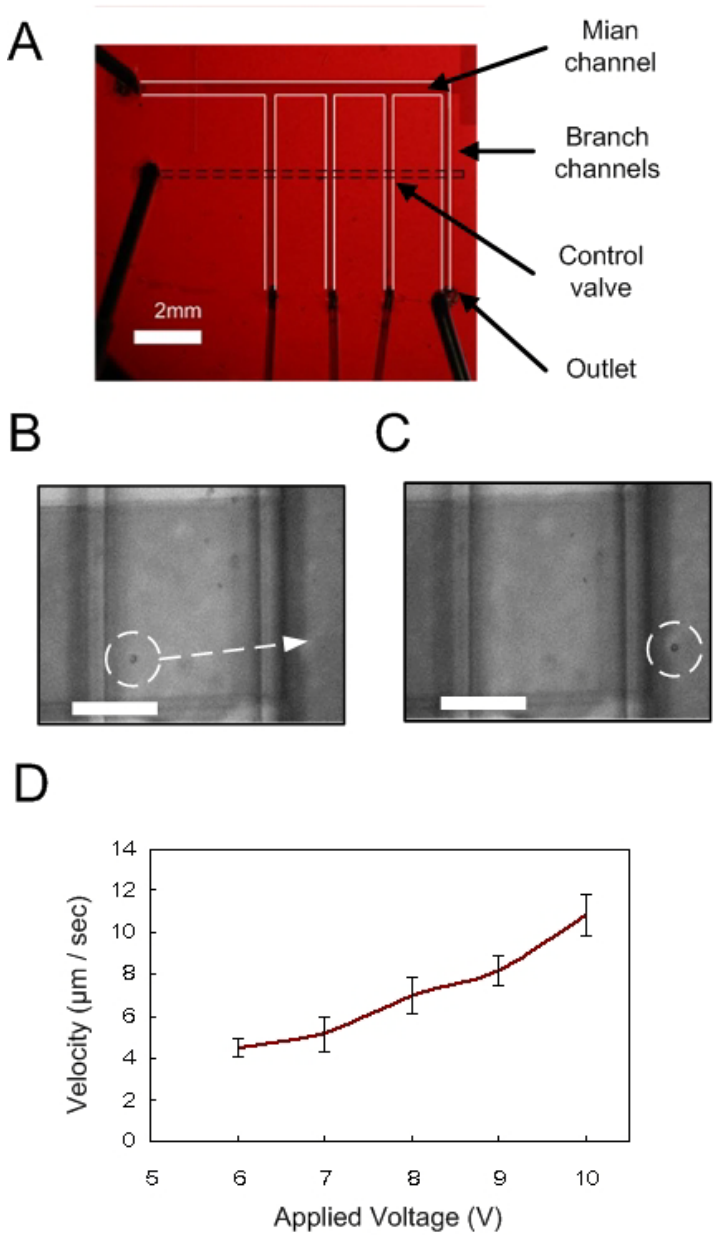

Figure 5- 4 (A) A microfluidic integrated OET. (B) Cell manipulation in the channel covered by SWNT electrode.scale bar =150μm. (C) Cell manipulation speed in microfluidic OET platform.

The microfluidic OET allows fluorescence-based cell sorting and manipulation. To exam the cell identification and cell separation, HeLa cells stained with Calcain AM were mixed with unstained cells. Before laoding the cells into the device, the pneumatic valve was closed and isotonic buffer was flushing into the channels. Because the isotonic buffer occupied the branch

channels, no cells flow into the channels during the loading. After the mixed cell suspension was introduced into the microfluidic OET, we inspect the cells in the main channel under bright-field (Figure 5- 5A) and fluorescence illumination (Figure 5- 5B).

The target stained HeLa cell was recognized from the population. When the light spot was projected, the target cell (circled by dotted line in Figure 5- 5) experienced a positive DEP force and moved toward the potential well. The target cell was pulled out from the population by changing the light spot location (Figure 5- 5C and Figure 5- 5D) and then moved into an adjacent channel (Figure 5- 5E and Figure 5- 5F). Once the target cells were moved into the adjacent channels, air flow was then induced to clean the main channel and remove the nun target cells. Figure 5- 5H shows the target cell stay at the same location in the adjacent channel after liquid plugs form, which demonstrates an 8.3-nL single-cell droplet.

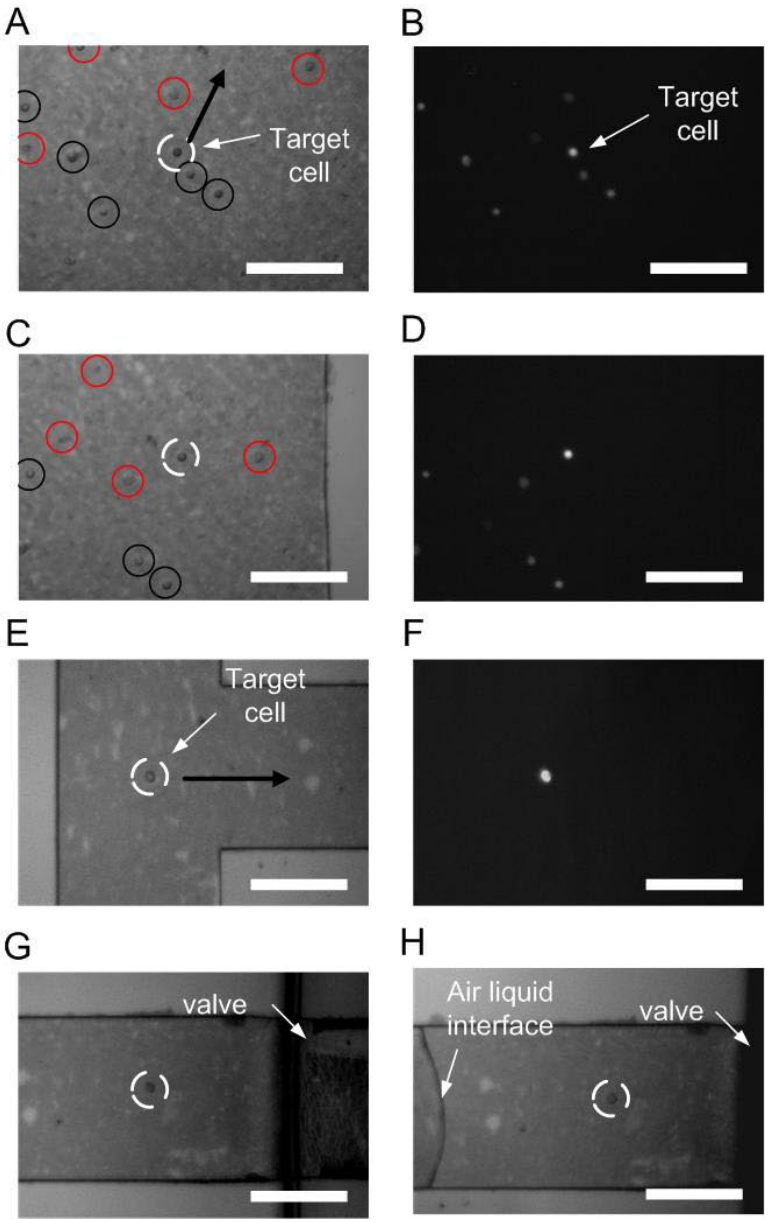

Figure 5- 5. The sequential images where cells are identified by fluorescent, manipulated by a light beam and the single-cell droplet formation. (A) The initial position of a target Hela cell is circled with write lines. (B) The fluorescent image of (A). (C)(D) The target cell is selected and moved away from other cells. (E)(F) The target cell is moved to the entrance of a perpendicular channel. (G) The target cell is inside the adjacent channel. (H) A liquid plug is formed in front of the valve after airflow in the main channel. Scale bars are 200μm.

In order to close the valve, the height of the fluid channels is usually 25- 30 μm, and the distance between top and bottom electrodes in this microfluidic OET platform is shorter than the conventional OET. When the size of the particle is similar to the distance over which the external E-field varies, a more precise approach to calculate DEP force is to use Maxwell stress tensor (MST) formulation, which is integrating the stress tensor T over the surface of the particle:

$$\vec{F}_{DEP}(t) = \oint (T \cdot \vec{n}) dA \qquad \textbf{Eq. 5- 1}$$

where $\vec{n}$ is the unit normal to A and t is time. This is the most general approach to the force [12]. For an applied electric field with a frequency less than 100 MHz, the expression for the time-average DEP force for spherical cells immersed in a medium with complex permittivity ε_s^* and subjected to electric field can be described as follows:

$$\langle F(DEP) \rangle = \frac{1}{4} \mathrm{Re}(\varepsilon_s^*) \oint_A \left[(EE^* + E^* E) - |E|^2 \right] \cdot \vec{n} dA \qquad \textbf{Eq. 5- 2}$$

where E is the electric field distributed on surface A enclosing the cell, and E* is the complex conjugate of E. To evaluate the DEP force in the platform, Comsol Multiphysics (Comsol, Inc. USA) was used for modeling. The Cosmol model was verified by simulating a case reported in literature [120] and comparing the results. Figure 5- 6 shows the setting dimensions and parameters for the simulations of SWNT OET. The diameter of HeLa cell was set to be 15μm while the distance between the center of the light spot and center of the cell is 15 μm. The cell was simulated by single shell model. The parameters for single shell model are the permittivity and conductivity of the cell's cytoplasm and membrane. The value of these parameters are from the literature [121]. The value of the permittivity and conductivity of the cell's cytoplasm are ε_r = 50 and σ = 0.53 Sm^{-1}. The value of the permittivity and conductivity of the cell's membrane are ε_r = 7 σ = 0.87 μSm^{-1}. The thickness of cell membrane is set to be 5 nm.

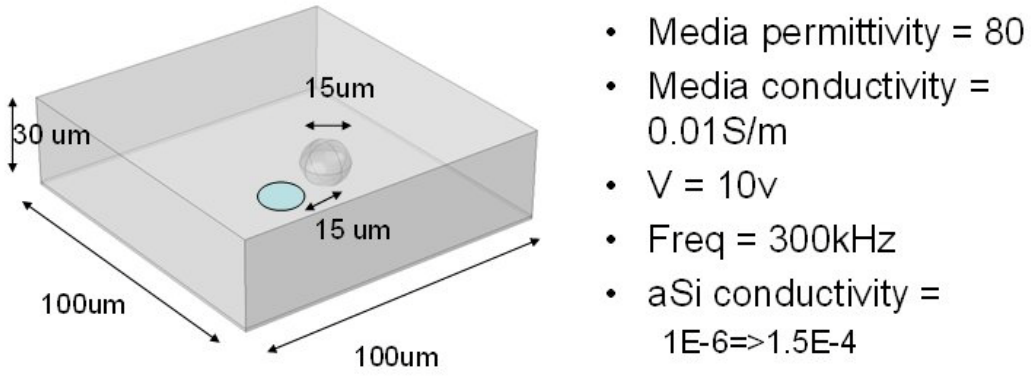

Figure 5- 6 The dimensions and the parameters for the simulations.

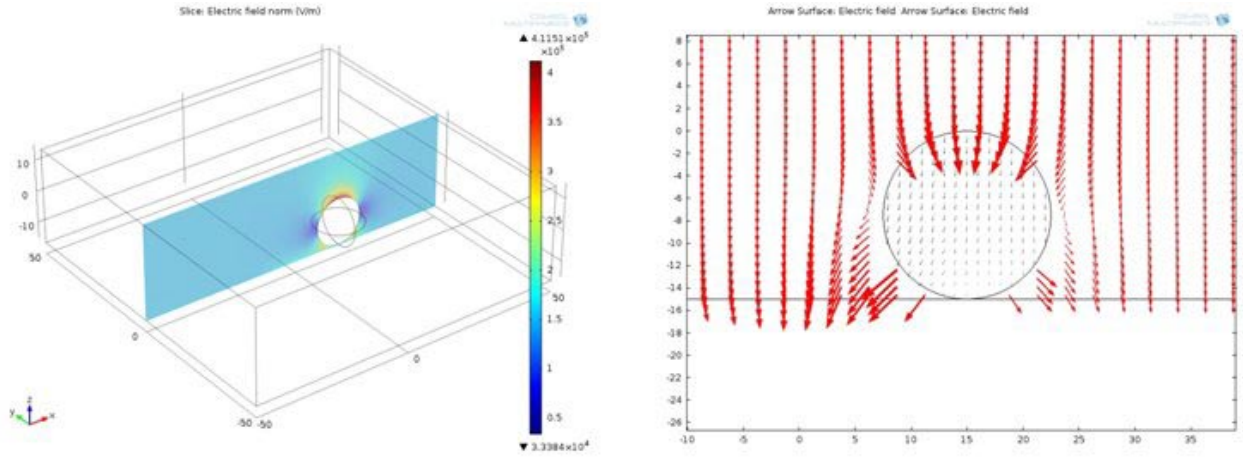

$$\langle F_{dep}(x,y,z)\rangle = (-28.8,\ 0.014,\ 207)\text{pN}$$

Figure 5- 7 The results of the simulation in the case of Figure5-6.

The result is shown in Figure 5- 7. If the cell is located on the photoconductive surface, the cell can experience a force toward the light spot. However, the simulation shows the cell can also experience a force toward the top channel. This force might be balanced when cell does not

directly contact the bottom surface. The force in x direction might decrease when the cell doesn't contact the bottom surface.

RT-qPCR

To demonstrate the downstream single or multiple cell analysis, we have measured the level of beta-actin mRNA of the cell samples prepared by microfluidic OET by RT-qPCR. As mentioned previously, two different procedures mentioned in previous were applied to the samples after transferring the single-cell droplets to the PCR tube. Figure 5- 8A shows the amplification curves of single or multiple cell samples in microliter reactions. The inset shows the standard curves which generated with known amounts of reference cDNA. The curves cover from 0.5 to 50000 pg of the standard samples. The threshold cycle (Ct) value of the curves were analyzed by the 2nd derivative maximum method for comparison of the level of the cell samples. The Ct value of single-cell samples prepared by our platform is 34.20. One of the advantages of microfluidic OET platform is sorting multiple cells in one droplet. To demonstrate this, five HeLa cells were randomly picked by the platform and the Ct value of five-cell sample is 30.61. The results of nanoliter RT reaction are shown in Figure 5- 8B. The curves obtained by diluting HeLa cell in isotonic solution are plotted for comparison of cell sample prepared by microfluidic OET platform. The Ct value of 25 cells and 1000 cells are 27.35 and 22.25 respectively. The measured Ct value of single-cell sample is 30.35, which is approximately 3-order lower than the sample with 1000 cells. It has been reported that the nanolitre scale reaction may increase the mRNA-to-cDNA processing efficiency [34, 122]. A shift of Ct value which may be due to the nanolitre scale reaction was observed. The phenomenon of rise of mRNA-to-cDNA efficiency is similar to the previous reports from other microfluidic devices.

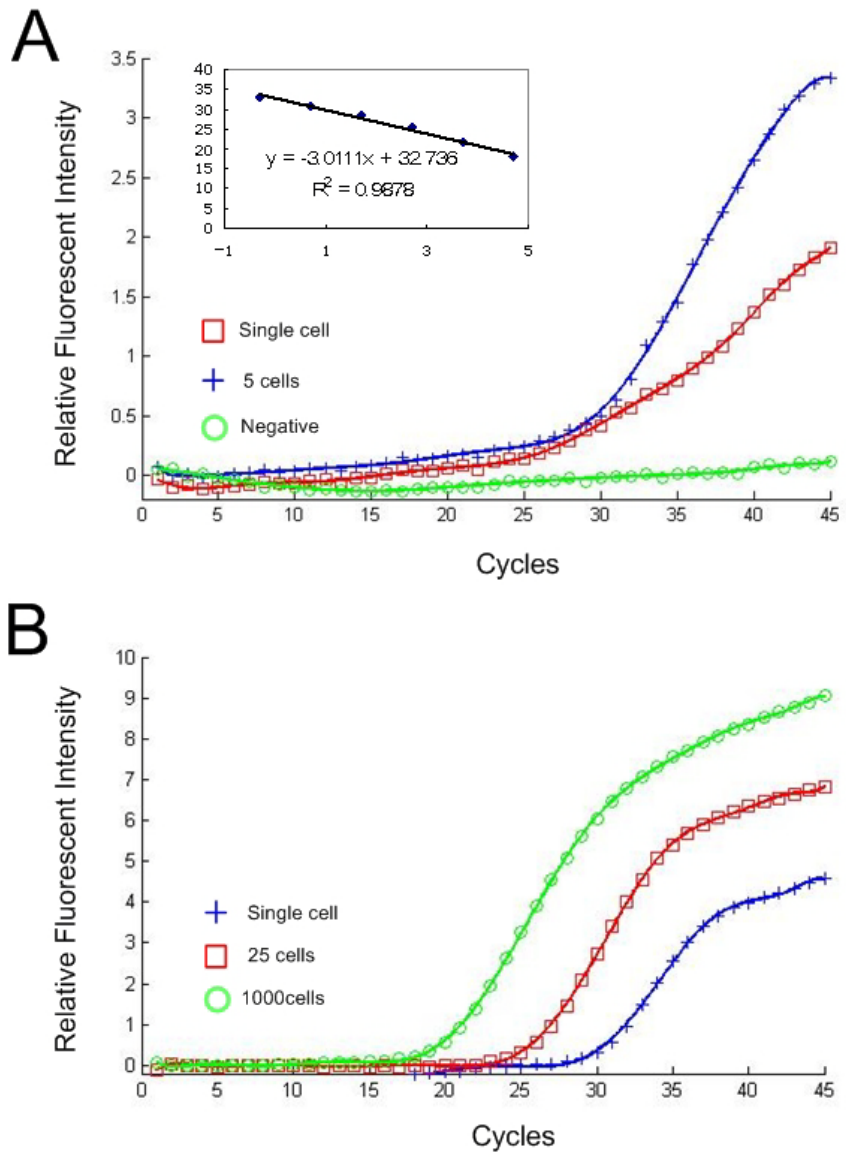

Figure 5- 8. qPCR of cDNA converted from Beta actin mRNA extracted from single and 5 HeLa cells. Data is compared with curves showing amplification of reference human cDNA as control.

5.3 3D Microfluidic OET for On-chip Single-cell Analysis

The schematic of the 3D microfluidic OET is shown in Figure 3- 1. The fabrication process is described in Chapter 3. The structure includes two layers of elastomeric structures made by PDMS and two

rigid ITO glass substrates. The bottom ITO glass is coated with a photoconductive layer for light-induced DEP forces. 3D microfluidic technique is utilized to fabricate “through patterns” (i.e. channels without top PDMS walls). The through patterns on the two thin PDMS membranes are overlapped to form OET manipulation regions. Cells in the regions can be directly exposed to top and bottom electrodes for dynamic DEP manipulation. Microfluidic pneumatic valves are implemented by multiple soft lithographies. Each device consists of two layers with elastomeric structures with a bottom control layer and a top flow connection layer. PDMS pneumatic valves are also formed by the membrane between the control channel and the link channel. When the control channel is pressurized, the membrane will be pushed up and the valve will be closed. A fabricated device is shown in Figure 3- 5A. The operation procedure is shown in Figure 5- 9. The layout of the channel is in “H” shape which consisted of three parts, two side channels and one middle channel. The two side channels are symmetrically connected to the middle channels. Four inlets/outlets are located at the ends of the two side channels and can be used for injection of cell suspension, buffers, or reagent mix, etc. In Figure 5- 9, the RT-qPCR master mix was prepared following the recipe in Section 5.2. The master mix was loaded into the middle channels from either one of the side channel (Figure 5- 9A). After loading the reagent mix, the two pneumatic valves were closed to prevent the lost of the master mix and to keep cells from entering the middle channels. The advantage of this design is that the pneumatic valves are push-up valves which provide good sealing to the reagents. Cell suspension was then introduced into one of the side channels. Cells in the OET manipulation region are selected under a microscope based on their optical signatures. Target cells then transported by light beams into neighboring chamber that are temporarily blocked by pneumatic valves that are all controlled by a single pressure source (Figure 5- 9B). A nanoliter liquid plug was formed by pressurizing airflow and then

mineral oil to remove the fluid in the main channel (Figure 5- 9B). At the same time, the other side channel was also flashed with oil. The oil prevents evaporation of reagent mix during the PCR thermal cycles. The pneumatic valves are then open to allow the target cell mix with the reagent mix. The mixing of cell and reagents is based on diffusion. The entire device was then moved to PCR thermal cycler for RT-qPCR.

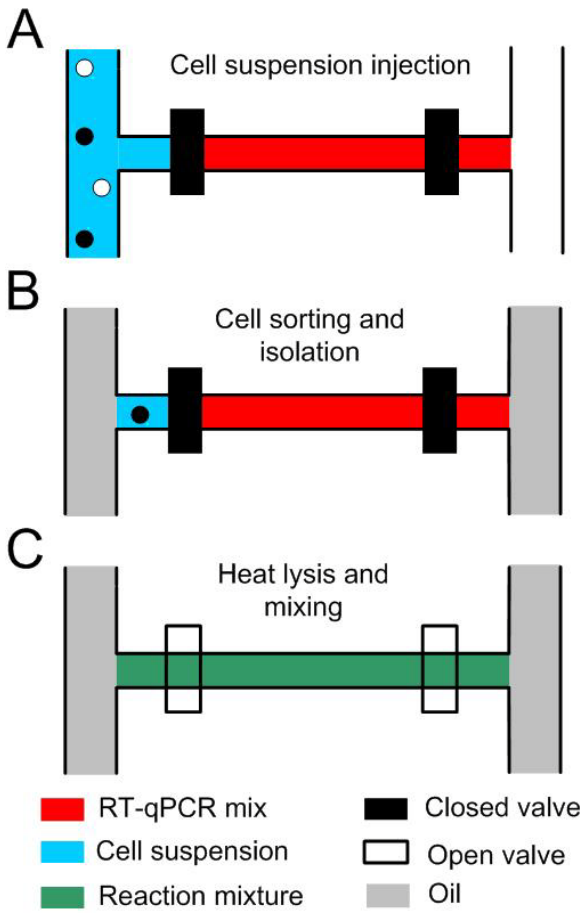

Figure 5- 9 The operation procedure of single-cell analysis on 3D microfluidic OET. (A) Cell suspension and RT-qPCR reagent mix are first separated by a pneumatic valve. (B) After cell mixture is investigated under a microscope based on their optical signatures, target cell is transported by light beams into neighboring chamber and isolated by injecting mineral oil. (C) Actuation of the valve results in mixing of the cell and the reagents. The chip will be placed on a thermoelectric cooler (TEC) for heat lysis and RT-PCR thermal cycles.

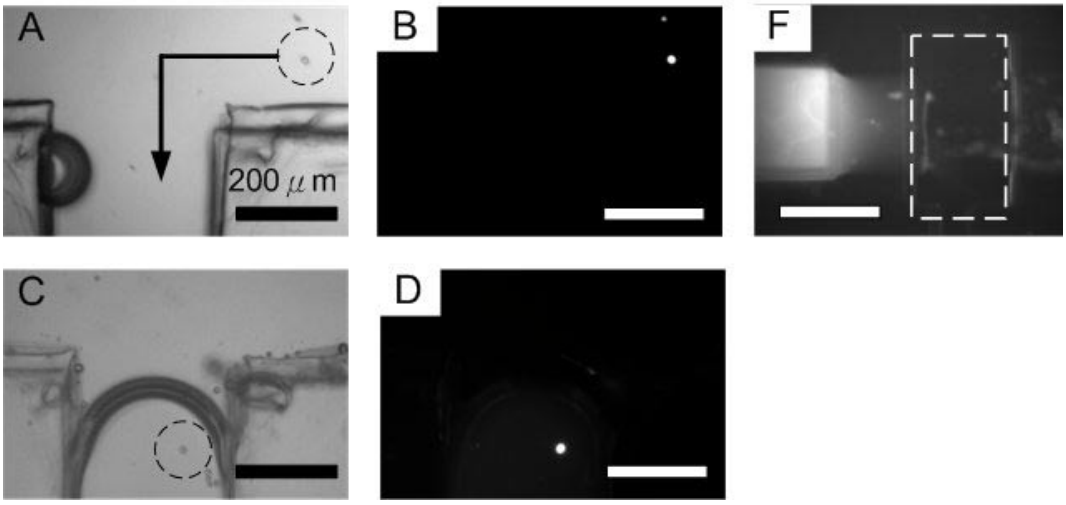

Figure 5- 10 (A) Target cell identified by fluorescent image was transported to the chamber by OET. (B) Fluorescent image of (A). (C)Target cell in the camber was isolated by oil. (D) Fluorescent image of (C). (F) scale bar =300μm.

Results and Discussions

To verify the procedure in Figure 5- 9, Ramos cells were prepared by the recipe mentioned in the previous section and introduced into a 3D microfluidic OET. Figure 5- 10F shows a fluorescent image near one of the pneumatic valve after loading the reagent mix. The valve which is marked by a dotted square was closed. The reagent mix showing fluorescence was stored in the left chamber. 3D microfluidic OET takes few advantages over the SWNT electrodes. The biggest advantage is the micro-valve type. The advantage is fully demonstrated in Figure 5- 10F. Figure 5- 10A to Figure 5- 10D show the snapshots of step B in the Figure 5- 9. A ramos cell was identified under a microscope with bright-filed (Figure 5- 10A) and fluorescent-mold (Figure 5- 10B). The target stained ramos cell was projected a light spot by a laser, the target cell (circled by dotted line in Figure 5- 10A) experienced a positive DEP force and moved toward the potential well. The target cell was pulled out from the population by changing the light spot

location (Figure 5- 10A and Figure 5- 10C) and then moved into the near chamber. Once the target cells were moved into the chamber, air flow was then induced to clean the main channel and remove the rest cells. Figure 5- 10B shows the target cell stay in the chamber after mineral oil injection. The water plug is surrounded by oil. On this platform, OET and PDMS microfluidic devices provide complementary functions. OET is a powerful tool enabling individual cell control in micro-channels but not effective in manipulating fluid. PDMS microfluidic device is effective in controlling the delivery of fluid but ineffective in manipulating particles or cells carried by the fluid. Integration of OET with 3D PDMS membranes promises a platform for sorting individual cells, for isolating them into discrete environments, and for on-chip cell treatment. Here, on-chip RT-PCR was used to demonstrate. The setup for RT-PCR is shown in Figure 5- 11. A Canon 5D Mark II digital single lens reflex (dSLR) camera was used to capture images. A Macro Lens (Canon Inc., USA) was connected to the dSLR and mounted to an optical table. Thermocycling setup was built by using a 39.7 mm × 39.7 mm thermoelectric cooler (TEC) and a FTC-100 controller (Ferrotec Inc., USA). A customized aluminium block with fins was connected to the TEC device with a layer of silver thermal compound. The temperature control was used the manufacturer software. Temperature feedback control was accomplished by adjusting parameters of PID control. A TR-1(2245) thermistor (Ferrotec Inc., USA) was placed on the TEC to monitor the temperature. The customized LabView program was developed to synchronize the thermal cycles and the image recording. A mercury lamp coupled with an optical fiber is illuminated on the device. In order to minimize the illumination time, a mechanical shutter is set. A commercial filter set with FAM excitation and emission wavelengths are placed on front of the devices and macro lens. The PCR thermocycling was followed the recipe in the previous section.

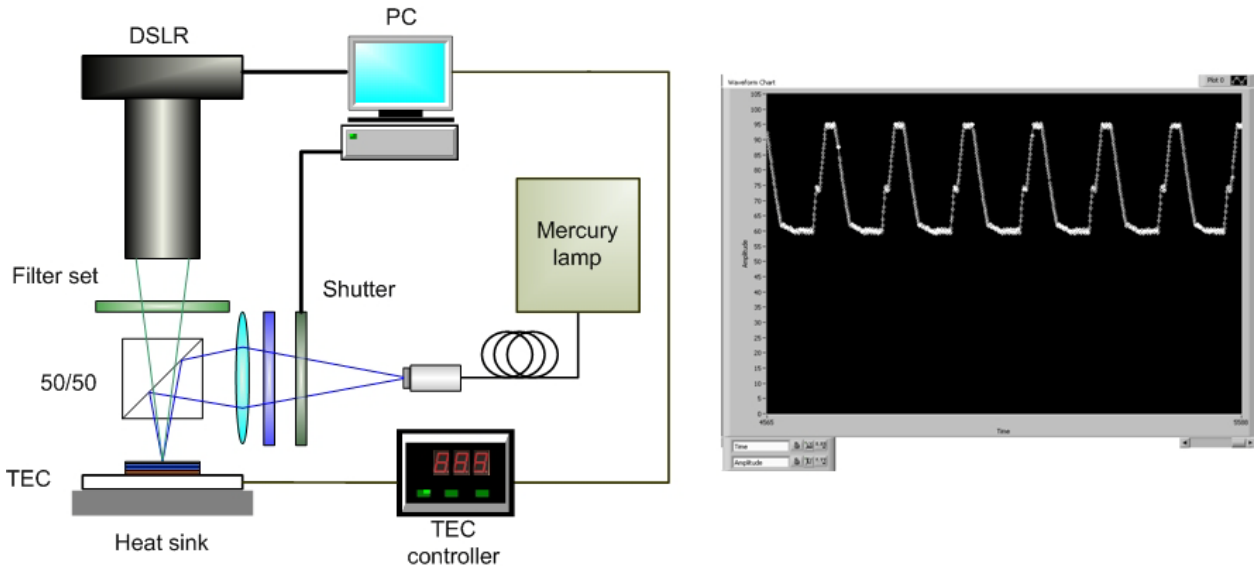

Figure 5- 11 The setup for fluorescent imaging and temperature control. 3D microfluidic OET is placed on a TEC controlled by a controller. A dSLR camera is used to record the fluorescent image of the device in every temperature cycles. The synchronization is achieved by a customized LabView program. The picture in the right shows an example of the LabView program monitoring the temperature on TEC.

The results of the RT-PCR were shown in Figure 5- 12. The fluorescent intensity of the middle PCR channel were recorded and analyzed by software (Image J). The average fluorescent intensities of the middle channel are plotted in the Figure. Three different lines present positive control, negative control and single-cell sample. The positive curve was generated by pumping PCR mixture with known amounts of reference cDNA (5000ng/μL) in the middle channel. The negative curve is obtained by mixing PCR reagents with DI water. Single-cell sample was prepared with the recipe in the previous section 5.2. The operation procedure is shown in Figure 5- 9. The recorded curves shown in Figure 5- 12 are not good enough for qPCR analysis. The variation of the fluorescent intensity makes the measurement of Ct value difficult. The reasons of the variation might come from the setup for fluorescent imaging. However, on-chip PCR has

been achieved and reported by literatures [123-129]. In the future, modifying the setup to achieve accurate measurement of Ct is practical. The amplification curves still show the difference between the negative and the single-cell sample. The trend of single-cell sample is similar to the positive control.

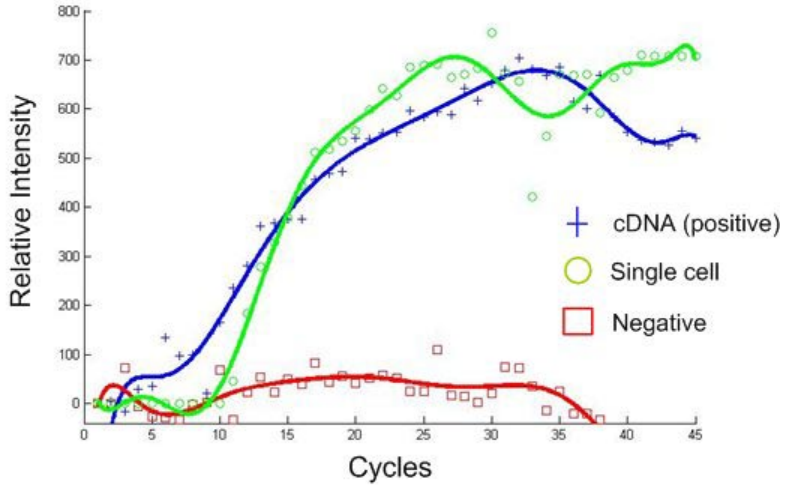

Figure 5- 12 Amplification curves of PCR performed on 3D microfluidic OET platform.

5.4 Conclusions

In conclusion, we have demonstrated a microfluidic integrated OET platform for single-cell or multi-cell sample preparation. The platform employs light-induced DEP and PDMS microfluidic channels to sort target cells based on their optical signatures into isolated droplets for downstream analysis. The optical cell manipulation function simplifies the design of microfluidic device for single cell analysis. The down-stream analysis can be performed in either off-chip or on-chip way. Off-chip methods utilize high sensitive commercial product for single or multiple cell analysis or even other types of analysis. In general, the on-chip analysis is not limited to RT-qPCR. It could be applied to the buffer or reagents mixing. In summary, this chapter presents

two different OETs which are integrated with SWNT electrode or 3D microfluidic membrane for off-chip or on-chip single-cell applications. Single-cell/multi-cell samples have been successfully prepared for analyzing the level of beta-actin mRNA by real-time RT-PCR. The simplicity of use solves the complexity of operating conventional microfluidic devices but still provides a rapid sorting and isolation tool for cell samples with small volume. In addition, the simplicity of the device design has the potential to be integrated with automated processing to perform high throughput.

Chapter 6 Summary

To be a powerful tool of cell manipulation, OET has many advantages and also face some challenges. The two main challenges of conventional OET are the integration of microfluidic channels, valve, pumps etc. and the lack of simultaneous large-area detection function. The first challenge, the integration of PDMS-based microfluidic components, restrains OET from complex processes such as injection or collection of samples, change of buffer media, or cell lyses.

To address this limitation of integration of PDMS microfluidic components, two techniques are purposed in this research. First, the integration by SWNT-embedded electrodes is discussed in Chapter 2. The second method, 3D PDMS membrane, is described in Chapter 3. Both techniques can solve the issue of the integration. The fabrication of SWNT electrode is developed for transparent and conductive layer in PDMS channels. The development is based on the concept of multilayer soft lithography. Therefore, the fabrication process fits for standard multilayer soft lithography and Chapter 2 shows the results of particles manipulation in PDMS channels by OET. The SWNT electrodes simplify the design of the devices. This successful integration steps up OET platforms to many useful applications. Furthermore, the ultimate usefulness of the fabrication of SWNT electrodes can lie not only in OET platform but also in many other microfluidic applications. In the other hand, the technique described in Chapter 3 trims the 3D PDMS membrane for OET integration. It keeps the original configuration of OET (tow ITO electrodes) and adds microfluidic components on OET. The improvements of 3D PDMS technique are increasing the “via patterns” from holes to channels and the flatness of the PDMA membranes. These two major improvements make it possible that the PDMS membrane

can be sandwiched in two rigid substrates and the OET function can be realized in those via channels. Several points can be compared between these two techniques. (1) Both methods make pressurized flow, pressurized valves, and OET manipulation impossible. (2) OET with SWNT-embedded electrodes uses push-down valves while 3D microfluidic OET uses push-up valves. (3) Commercial ITO electrodes on 3D microfluidic OET platform are more conductive and transparent than the state-of-art SWNT electrodes. (4) Particles or cells can be manipulated across the micro-valve under SWNT electrodes but they cannot be moved across the valve in 3D microfluidic structures.

For single-cell applications, two new platforms incorporating OET into PDMS-based microfluidic channels enabling single or multiple cell control to accomplish multi-steps tasks were demonstrated in Chapter 5. On these two platforms, techniques described in Chapter 2 and Chapter 3 are used to build the devices. OET and PDMS microfluidic components provide complementary functions. OET provides spatial trapping and sorting cells of interest. PMDS microfluidic components are effective in controlling fluid. Both integrated platforms allow users to selectively retrieve individual cells from a population based on their optical signatures such as size, shape, and fluorescence colors. The comb-shaped design of SWNT OET can further isolate the cells into discrete droplets and then put the droplets out for external single-cell analysis. Therefore, OET with SWNT-embedded electrodes is designed for off-chip analysis. In 3D microfluidic OET platform, the H-shaped channel can be used for on-chip analysis such as single-cell RT-qPCR. However, the 3D microfluidic OET platform is not limited to on-chip applications. It can be used for off-chip too.

Chapter 4 discusses arming OET with large-area detection. It has been demonstrated that the optical detection and manipulation area of OET can be extended to 17.96 mm × 13.52 mm

using lensfree on-chip holographic microscope and OET. The system enable large-area, programmable, parallel light-induced DEP manipulation of microscopic particles or cells with real-time position feedback. Methods of automated pattern matching and image reconstruction have been demonstrated for monitoring thousands of objects inside the FOV. Real-time closed-loop manipulation of polystyrene particles and cells has been achieved with this holographic on-chip microscope-furnished OET system.

The potential of further integration of 3D microfluidic OET platform and lensfree on-chip holographic microscope is enormous. Large-area parellel cell manipulation and high-throughput cell sorting can be realized by combining the above two techniques.

Chapter 7 References

REFERENCES

[1] P. Y. Chiou, *et al.*, "Massively parallel manipulation of single cells and microparticles using optical images," *Nature*, vol. 436, pp. 370-372, 2005.

[2] A. Jamshidi, *et al.*, "Dynamic manipulation and separation of individual semiconducting and metallic nanowires," *Nat Photon*, vol. 2, pp. 86-89, 2008.

[3] M. W. Lee, *et al.*, "Manipulation and patterning of carbon nanotubes utilizing optically induced dielectrophoretic forces," *Microfluidics and Nanofluidics*, vol. 8, pp. 609-617, 2010.

[4] P. J. Pauzauskie, *et al.*, "Parallel trapping of multiwalled carbon nanotubes with optoelectronic tweezers," *Applied Physics Letters*, vol. 95, pp. 113104-113104-3, 2009.

[5] A. T. Ohta, *et al.*, "Dynamic cell and microparticle control via optoelectronic tweezers," *Microelectromechanical Systems, Journal of*, vol. 16, pp. 491-499, 2007.

[6] C. ILIESCU, *et al.*, "3D Dielectrophoretic Chips: Trapping and Separation of Cell Populations," *SCIENCE AND TECHNOLOGY*, vol. 13, pp. 49-64, 2010.

[7] H. Hwang, *et al.*, "Enhanced discrimination of normal oocytes using optically induced pulling-up dielectrophoretic force," *Biomicrofluidics*, vol. 3, 2009.

[8] W. Choi, *et al.*, "Programmable manipulation of motile cells in optoelectronic tweezers using a grayscale image," *Applied Physics Letters*, vol. 93, p. 143901, 2008.

[9] M. Hoeb, *et al.*, "Light-induced dielectrophoretic manipulation of DNA," *Biophysical journal*, vol. 93, pp. 1032-1038, 2007.

[10] Y. H. Lin, *et al.*, "Manipulation of single DNA molecules by using optically projected images," *Optics Express*, vol. 17, pp. 15318-15329, 2009.

[11] J. K. Valley, *et al.*, "Preimplantation mouse embryo selection guided by light-induced dielectrophoresis," *PloS one*, vol. 5, p. e10160, 2010.

[12] X. Wang, *et al.*, "General expressions for dielectrophoretic force and electrorotational torque derived using the Maxwell stress tensor method," *Journal of electrostatics*, vol. 39, pp. 277-295, 1997.

[13] B. Çetin and D. Li, "Dielectrophoresis in microfluidics technology," *Electrophoresis*, vol. 32, pp. 2410-2427, 2011.

[14] J. K. Valley, *et al.*, "Operational regimes and physics present in optoelectronic tweezers," *Microelectromechanical Systems, Journal of*, vol. 17, pp. 342-350, 2008.

[15] P. Y. Chiou, *et al.*, "Light-actuated ac electroosmosis for nanoparticle manipulation," *Microelectromechanical Systems, Journal of*, vol. 17, pp. 525-531, 2008.

[16] A. Jamshidi, *et al.*, "NanoPen: dynamic, low-power, and light-actuated patterning of nanoparticles," *Nano Letters*, vol. 9, p. 2921, 2009.

[17] H. Hwang and J. K. Park, "Rapid and selective concentration of microparticles in an optoelectrofluidic platform," *Lab Chip*, vol. 9, pp. 199-206, 2008.

[18] S.-Y. Park, *et al.*, "A light-induced dielectrophoretic droplet manipulation platform," *Lab on a Chip*, vol. 9, pp. 3228-3235, 2009.
[19] S. Park, *et al.*, "Floating electrode optoelectronic tweezers: Light-driven dielectrophoretic droplet manipulation in electrically insulating oil medium," *Applied physics letters*, vol. 92, p. 151101, 2008.
[20] A. Ohta, *et al.*, "Optically controlled cell discrimination and trapping using optoelectronic tweezers," *Selected Topics in Quantum Electronics, IEEE Journal of*, vol. 13, pp. 235-243, 2007.
[21] S. M. Yang, *et al.*, "Dynamic manipulation and patterning of microparticles and cells by using TiOPc-based optoelectronic dielectrophoresis," *Optics Letters*, vol. 35, pp. 1959-1961, Jun.
[22] W. Choi, *et al.*, "Lab-on-a-display: a new microparticle manipulation platform using a liquid crystal display (LCD)," *Microfluidics and Nanofluidics*, vol. 3, pp. 217-225, 2007.
[23] H. Hwang, *et al.*, "Interactive manipulation of blood cells using a lens integrated liquid crystal display based optoelectronic tweezers system," *Electrophoresis*, vol. 29, pp. 1203-1212, 2008.
[24] H.-y. Hsu, *et al.*, "Phototransistor-based optoelectronic tweezers for dynamic cell manipulation in cell culture media," *Lab on a Chip*, vol. 10, pp. 165-172, 2010.
[25] Y. Lin and G. Lee, "Optically induced flow cytometry for continuous microparticle counting and sorting," *Biosensors and Bioelectronics*, vol. 24, pp. 572-578, 2008.
[26] D. Lee, *et al.*, "Generation and manipulation of droplets in an optoelectrofluidic device integrated with microfluidic channels," *Applied Physics Letters*, vol. 95, p. 164102, 2009.
[27] J. W. Hong and S. R. Quake, "Integrated nanoliter systems," *Nature biotechnology*, vol. 21, pp. 1179-1183, 2003.
[28] G. Whitesides, "The origins and the future of microfluidics," *Nature*, vol. 442, pp. 368-373, 2006.
[29] J. C. McDonald, *et al.*, "Fabrication of microfluidic systems in poly (dimethylsiloxane)," *Electrophoresis*, vol. 21, pp. 27-40, 2000.
[30] M. A. Unger, *et al.*, "Monolithic microfabricated valves and pumps by multilayer soft lithography," *Science*, vol. 288, p. 113, 2000.
[31] D. Laser and J. Santiago, "A review of micropumps," *Journal of Micromechanics and Microengineering*, vol. 14, p. R35, 2004.
[32] N. T. Nguyen and Z. Wu, "Micromixers—a review," *Journal of Micromechanics and Microengineering*, vol. 15, p. R1, 2005.
[33] E. A. Mansur, *et al.*, "A state-of-the-art review of mixing in microfluidic mixers," *Chinese Journal of Chemical Engineering*, vol. 16, pp. 503-516, 2008.
[34] J. F. Zhong, *et al.*, "A microfluidic processor for gene expression profiling of single human embryonic stem cells," *Lab Chip*, vol. 8, pp. 68-74, 2007.
[35] S. Guo, *et al.*, "An integrated microfluidic culture device for quantitative analysis of human embryonic stem cells," *Lab on a Chip*, vol. 9, pp. 555-563, 2009.
[36] H. Chen, *et al.*, "Electromechanical Properties of Pressure-Actuated Poly (dimethylsiloxane) Microfluidic Push-Down Valves," *Analytical chemistry*, vol. 80, pp. 6110-6113, 2008.
[37] S. T. Yung Joon Jung Swastik Kar, Caterina Soldano, Gunaranjan Viswanathan, Xuesong Li, Zhaoling Yao, Fung Suong Ou, Aditya Avadhanula, Robert Vajtai,Seamus Curran,# Omkaram Nalamasu, and Pulickel M. Ajayan, "MULTI-LAYER EMBEDMENT OF

CONDUCTIVE AND NON-CONDUCTIVE PDMS FOR ALL-ELASTOMER MEMS," *Nano Lett.,* vol. 6, p. 6, February 1 2006.
[38] X. Gong and W. Wen, "Polydimethylsiloxane-based conducting composites and their applications in microfluidic chip fabrication," *Biomicrofluidics,* vol. 3, p. 012007, 2009.
[39] L. Chao-Xuan and C. Jin-Woo, "Patterning conductive PDMS nanocomposite in an elastomer using microcontact printing," *Journal of Micromechanics and Microengineering,* vol. 19, pp. 085019 (7 pp.)-085019 (7 pp.), August 2009.
[40] S. Rosset, *et al.*, "Mechanical properties of electroactive polymer microactuators with ion-implanted electrodes," vol. 6524, ed, 2007, pp. 652410-1.
[41] S. Rosset, *et al.*, "Mechanical characterization of a dielectric elastomer microactuator with ion-implanted electrodes," *Sensors and Actuators A: Physical,* vol. 144, pp. 185-193, 2008.
[42] P. Dubois, *et al.*, "Voltage control of the resonance frequency of dielectric electroactive polymer (DEAP) membranes," vol. 17, ed: IEEE, 2008, pp. 1072-1081.
[43] M. Niklaus, *et al.*, "Microstructure of 5keV gold-implanted polydimethylsiloxane," *Scripta Materialia,* vol. 59, pp. 893-896, 2008.
[44] J. Y. Baek, *et al.*, "Stable deposition and patterning of metal layers on the PDMS substrate and characterization for the development of the flexible and implantable micro electrode," *Solid State Phenomena,* vol. 124, pp. 165-168, 2007.
[45] Y. L. Loo, *et al.*, "Soft, conformable electrical contacts for organic semiconductors: High-resolution plastic circuits by lamination," *Proceedings of the National Academy of Sciences,* vol. 99, p. 10252, 2002.
[46] J. Y. Baek, *et al.*, "Flexible polymeric dry electrodes for the long-term monitoring of ECG," *Sensors and Actuators A: Physical,* vol. 143, pp. 423-429, 2008.
[47] S. P. Lacour, *et al.*, "Stretchable gold conductors on elastomeric substrates," *Applied Physics Letters,* vol. 82, pp. 2404-2406, 2003.
[48] J. A. Rogers, *et al.*, "Materials and Mechanics for Stretchable Electronics," *Science,* vol. 327, p. 1603, 2010.
[49] L. B. Hu, *et al.*, "Carbon Nanotube Thin Films: Fabrication, Properties, and Applications," *Chemical Reviews,* p. 18, 2010.
[50] Q. Cao and J. A. Rogers, "Ultrathin Films of Single Walled Carbon Nanotubes for Electronics and Sensors: A Review of Fundamental and Applied Aspects," *Advanced Materials,* vol. 21, pp. 29-53, 2009.
[51] M. W. Rowell, *et al.*, "Organic solar cells with carbon nanotube network electrodes," *Applied Physics Letters,* vol. 88, p. 233506, 2009.
[52] Q. Cao, *et al.*, "Highly Bendable, Transparent Thin Film Transistors That Use Carbon Nanotube Based Conductors and Semiconductors with Elastomeric Dielectrics," *Advanced Materials,* vol. 18, pp. 304-309, 2006.
[53] D. Zhang, *et al.*, "Transparent, conductive, and flexible carbon nanotube films and their application in organic light-emitting diodes," *Nano Lett,* vol. 6, pp. 1880-1886, 2006.
[54] L. Hu, *et al.*, "Electrowetting devices with transparent single-walled carbon nanotube electrodes," *Applied Physics Letters,* vol. 90, p. 093124, 2007.
[55] L. B. Hu, *et al.*, "A method of fabricating highly transparent and conductive interpenetrated carbon nanotube-parylene networks," *Nanotechnology,* vol. 20, p. 5, Nov 2009.

[56] E. Lahiff, *et al.*, "Selective positioning and density control of nanotubes within a polymer thin film," *Nano Letters*, vol. 3, pp. 1333-1337, 2003.
[57] K. Lee, *et al.*, "Carbon nanotube film piezoresistors embedded in polymer membranes," *Applied Physics Letters*, vol. 96, p. 013511, 2010.
[58] H. Cao, *et al.*, "Single-walled carbon nanotube network/poly composite thin film for flow sensor," *Microsystem Technologies-Micro-and Nanosystems-Information Storage and Processing Systems*, vol. 16, pp. 955-959, Jun 2010.
[59] Z. Wu, *et al.*, "Transparent, conductive carbon nanotube films," *Science*, vol. 305, p. 1273, 2004.
[60] Y. X. Zhou, *et al.*, "A method of printing carbon nanotube thin films," *Applied Physics Letters*, vol. 88, p. 3, Mar 2006.
[61] M. Y. Zhang, *et al.*, "A simple method for fabricating multi-layer PDMS structures for 3D microfluidic chips," *Lab on a Chip*, vol. 10, pp. 1199-1203, 2010.
[62] J. R. Anderson, *et al.*, "Fabrication of topologically complex three-dimensional microfluidic systems in PDMS by rapid prototyping," *Analytical chemistry*, vol. 72, pp. 3158-3164, 2000.
[63] N. L. Jeon, *et al.*, "Microfluidics section: design and fabrication of integrated passive valves and pumps for flexible polymer 3-dimensional microfluidic systems," *Biomedical Microdevices*, vol. 4, pp. 117-121, 2002.
[64] C. F. Carlborg, *et al.*, "A high-yield process for 3-d large-scale integrated microfluidic networks in PDMS," *Microelectromechanical Systems, Journal of*, vol. 19, pp. 1050-1057, 2010.
[65] D. T. Chiu, *et al.*, "Patterned deposition of cells and proteins onto surfaces by using three-dimensional microfluidic systems," *Proceedings of the National Academy of Sciences*, vol. 97, pp. 2408-2413, 2000.
[66] A. W. Martinez, *et al.*, "Three-dimensional microfluidic devices fabricated in layered paper and tape," *Proceedings of the National Academy of Sciences*, vol. 105, pp. 19606-19611, 2008.
[67] E. P. Kartalov, *et al.*, "Microfluidic vias enable nested bioarrays and autoregulatory devices in Newtonian fluids," *Proceedings of the National Academy of Sciences*, vol. 103, pp. 12280-12284, 2006.
[68] Y. Luo and R. N. Zare, "Perforated membrane method for fabricating three-dimensional polydimethylsiloxane microfluidic devices," *Lab Chip*, vol. 8, pp. 1688-1694, 2008.
[69] J. C. McDonald, *et al.*, "Prototyping of microfluidic devices in poly (dimethylsiloxane) using solid-object printing," *Analytical chemistry*, vol. 74, pp. 1537-1545, 2002.
[70] H. Wu, *et al.*, "Fabrication of complex three-dimensional microchannel systems in PDMS," *Burns*, vol. 190, p. 197, 2003.
[71] J. H. Kang, *et al.*, "Fabrication of a poly (dimethylsiloxane) membrane with well-defined through-holes for three-dimensional microfluidic networks," *Journal of Micromechanics and Microengineering*, vol. 19, p. 045027, 2009.
[72] G. Shah, *et al.*, "EWOD-driven droplet microfluidic device integrated with optoelectronic tweezers as an automated platform for cellular isolation and analysis," *Lab on a Chip*, vol. 9, pp. 1732-1739, 2009.
[73] A. Plecis and Y. Chen, "Fabrication of microfluidic devices based on glass-PDMS-glass technology," *Microelectronic engineering*, vol. 84, pp. 1265-1269, 2007.

[74] D. R. Albrecht, *et al.*, "Probing the role of multicellular organization in three-dimensional microenvironments," *Nature methods*, vol. 3, pp. 369-375, 2006.
[75] J. El-Ali, *et al.*, "Cells on chips," *Nature*, vol. 442, pp. 403-411, 2006.
[76] X. Ding, *et al.*, "On-chip manipulation of single microparticles, cells, and organisms using surface acoustic waves," *Proceedings of the National Academy of Sciences*, 2012.
[77] M. Tanase, *et al.*, "Assembly of multicellular constructs and microarrays of cells using magnetic nanowires," *Lab Chip*, vol. 5, pp. 598-605, 2005.
[78] M. Tien, *et al.*, "Heterogeneous integration of InGaAsP microdisk laser on a silicon platform using optofluidic assembly," *Applied Physics A: Materials Science & Processing*, vol. 95, pp. 967-972, 2009.
[79] H. Hwang and J. K. Park, "Measurement of molecular diffusion based on optoelectrofluidic fluorescence microscopy," *Analytical chemistry*, vol. 81, pp. 9163-9167, 2009.
[80] A. T. Ohta, *et al.*, "Motile and non-motile sperm diagnostic manipulation using optoelectronic tweezers," *Lab on a Chip*, vol. 10, pp. 3213-3217, 2010.
[81] J. Valley, *et al.*, "Parallel single-cell light-induced electroporation and dielectrophoretic manipulation," *Lab on a Chip*, vol. 9, p. 1714, 2009.
[82] S. O. Isikman, *et al.*, "Lensfree computational microscopy tools for cell and tissue imaging at the point-of-care and in low-resource settings," *Analytical Cellular Pathology*, vol. 35, pp. 229-247, 2012.
[83] S. Seo, *et al.*, "High-throughput lens-free blood analysis on a chip," *Analytical chemistry*, vol. 82, pp. 4621-4627, 2010.
[84] O. Mudanyali, *et al.*, "Detection of waterborne parasites using field-portable and cost-effective lensfree microscopy," *Lab Chip*, vol. 10, pp. 2419-2423, 2010.
[85] T. W. Su, *et al.*, "Compact and light-weight automated semen analysis platform using lensfree on-chip microscopy," *Analytical chemistry*, 2010.
[86] W. Bishara, *et al.*, "Lensfree on-chip microscopy over a wide field-of-view using pixel super-resolution," *Optics Express*, vol. 18, pp. 11181-11191, 2010.
[87] A. Greenbaum, *et al.*, "Imaging without lenses: achievements and remaining challenges of wide-field on-chip microscopy," *Nature Methods*, vol. 9, 2012.
[88] T. W. Su, *et al.*, "Multi-angle lensless digital holography for depth resolved imaging on a chip," *Optics Express*, vol. 18, pp. 9690-9711, 2010.
[89] S. O. Isikman, *et al.*, "Optofluidic Tomography on a chip," *Applied Physics Letters*, vol. 98, p. 161109, 2011.
[90] S. O. Isikman, *et al.*, "Lens-free optical tomographic microscope with a large imaging volume on a chip," *Proceedings of the National Academy of Sciences*, vol. 108, p. 7296, 2011.
[91] W. Xu, *et al.*, "Digital in-line holography for biological applications," *Proceedings of the National Academy of Sciences*, vol. 98, pp. 11301-11305, 2001.
[92] W. Bishara, *et al.*, "Holographic pixel super-resolution in portable lensless on-chip microscopy using a fiber-optic array," *Lab on a Chip*, vol. 11, pp. 1276-1279, 2011.
[93] S. Seo, *et al.*, "Lensfree holographic imaging for on-chip cytometry and diagnostics," *Lab Chip*, vol. 9, pp. 777-787, 2009.
[94] O. Mudanyali, *et al.*, "Compact, light-weight and cost-effective microscope based on lensless incoherent holography for telemedicine applications," *Lab Chip*, vol. 10, pp. 1417-1428, 2010.

[95] M. Diehn, *et al.*, "Association of reactive oxygen species levels and radioresistance in cancer stem cells," *Nature*, vol. 458, pp. 780-783, 2009.
[96] T. Kalisky, *et al.*, "Genomic analysis at the single-cell level," *Annual review of genetics*, vol. 45, pp. 431-445, 2011.
[97] A. Ståhlberg, *et al.*, "Defining cell populations with single-cell gene expression profiling: correlations and identification of astrocyte subpopulations," *Nucleic acids research*, vol. 39, pp. e24-e24, 2011.
[98] M. Bengtsson, *et al.*, "Gene expression profiling in single cells from the pancreatic islets of Langerhans reveals lognormal distribution of mRNA levels," *Genome research*, vol. 15, pp. 1388-1392, 2005.
[99] M. E. Lidstrom and M. C. Konopka, "The role of physiological heterogeneity in microbial population behavior," *Nature chemical biology*, vol. 6, pp. 705-712, 2010.
[100] M. R. Emmert-Buck, *et al.*, "Laser capture microdissection," *Science*, vol. 274, pp. 998-1001, 1996.
[101] R. F. Bonner, *et al.*, "Laser capture microdissection: molecular analysis of tissue," *Science (New York, NY)*, vol. 278, pp. 1481, 1483, 1997.
[102] M. Eisenstein, "Cell sorting: divide and conquer," *Nature*, vol. 441, pp. 1179-1185, 2006.
[103] R. N. Zare and S. Kim, "Microfluidic Platforms for Single-Cell Analysis," *Annual review of biomedical engineering*, vol. 12, pp. 187-201, 2010.
[104] H. Yin and D. Marshall, "Microfluidics for single cell analysis," *Current Opinion in Biotechnology*, vol. 23, pp. 110-119, 2012.
[105] J. S. Marcus, *et al.*, "Microfluidic single-cell mRNA isolation and analysis," *Analytical chemistry*, vol. 78, pp. 3084-3089, 2006.
[106] Y. Marcy, *et al.*, "Dissecting biological "dark matter" with single-cell genetic analysis of rare and uncultivated TM7 microbes from the human mouth," *Proceedings of the National Academy of Sciences*, vol. 104, pp. 11889-11894, 2007.
[107] B. Huang, *et al.*, "Counting low-copy number proteins in a single cell," *Science Signalling*, vol. 315, p. 81, 2007.
[108] H. C. Fan, *et al.*, "Whole-genome molecular haplotyping of single cells," *Nature biotechnology*, vol. 29, pp. 51-57, 2010.
[109] J. F. Zhong, *et al.*, "Microfluidic devices for investigating stem cell gene regulation via single-cell analysis," *Current medicinal chemistry*, vol. 15, pp. 2897-2900, 2008.
[110] J. Kovac and J. Voldman, "Intuitive, image-based cell sorting using optofluidic cell sorting," *Analytical chemistry*, vol. 79, pp. 9321-9330, 2007.
[111] P. C. Blainey, *et al.*, "Genome of a low-salinity ammonia-oxidizing archaeon determined by single-cell and metagenomic analysis," *PloS one*, vol. 6, p. e16626, 2011.
[112] M. C. Wu, "Optoelectronic tweezers," *Nature Photonics*, vol. 5, pp. 322-324, 2011.
[113] H. Hwang and J. K. Park, "Optoelectrofluidic platforms for chemistry and biology," *Lab Chip*, vol. 11, pp. 33-47, 2010.
[114] X. Hu, *et al.*, "Marker-specific sorting of rare cells using dielectrophoresis," *Proceedings of the National Academy of Sciences of the United States of America*, vol. 102, p. 15757, 2005.
[115] J. D. Adams, *et al.*, "Multitarget magnetic activated cell sorter," *Proceedings of the National Academy of Sciences*, vol. 105, pp. 18165-18170, 2008.
[116] J. Shi, *et al.*, "Continuous particle separation in a microfluidic channel via standing surface acoustic waves (SSAW)," *Lab Chip*, vol. 9, pp. 3354-3359, 2009.

[117] K.-W. Huang, *et al.*, "Electrodes for Microfluidic Integrated Optoelectronic Tweezers," *Advances in OptoElectronics*, vol. 2011, 2011.
[118] D. Issadore, *et al.*, "A microfluidic microprocessor: controlling biomimetic containers and cells using hybrid integrated circuit/microfluidic chips," *Lab Chip*, vol. 10, pp. 2937-2943, 2010.
[119] J. K. Valley, *et al.*, "A unified platform for optoelectrowetting and optoelectronic tweezers," *Lab Chip*, vol. 11, 2011.
[120] C. Rosales and K. M. Lim, "Numerical comparison between Maxwell stress method and equivalent multipole approach for calculation of the dielectrophoretic force in single-cell traps," *Electrophoresis*, vol. 26, pp. 2057-2065, 2005.
[121] S. L. Neale, *et al.*, "Trap profiles of projector based optoelectronic tweezers (OET) with HeLa cells," *Optics Express*, vol. 17, p. 5232, 2009.
[122] N. Bontoux, *et al.*, "Integrating whole transcriptome assays on a lab-on-a-chip for single cell gene profiling," *Lab Chip*, vol. 8, pp. 443-450, 2008.
[123] A. C. Hatch, *et al.*, "1-Million droplet array with wide-field fluorescence imaging for digital PCR," *Lab on a Chip*, vol. 11, pp. 3838-3845, 2011.
[124] S. L. Spurgeon, *et al.*, "High throughput gene expression measurement with real time PCR in a microfluidic dynamic array," *PloS one*, vol. 3, p. e1662, 2008.
[125] A. K. White, *et al.*, "High-throughput microfluidic single-cell RT-qPCR," *Proceedings of the National Academy of Sciences*, vol. 108, pp. 13999-14004, 2011.
[126] L. Warren, *et al.*, "Transcription factor profiling in individual hematopoietic progenitors by digital RT-PCR," *Proceedings of the National Academy of Sciences*, vol. 103, pp. 17807-17812, 2006.
[127] L. A. Warren, *et al.*, "Transcriptional instability is not a universal attribute of aging," *Aging cell*, vol. 6, pp. 775-782, 2007.
[128] N. R. Beer, *et al.*, "On-chip single-copy real-time reverse-transcription PCR in isolated picoliter droplets," *Analytical chemistry*, vol. 80, pp. 1854-1858, 2008.
[129] N. R. Beer, *et al.*, "On-chip, real-time, single-copy polymerase chain reaction in picoliter droplets," *Analytical chemistry*, vol. 79, pp. 8471-8475, 2007.